UNIVERSITY OF
LINCOLN

SCHOOL OF MATHEMATICS
AND PHYSICS

Optical and Morphological Properties of Copper Indium Disulphide Quantum Dots

Robert Sharp

SHA13487651

MSc by Research in Nanomaterials Science

School of Mathematics and Physics

University of Lincoln

2019

CONTENTS

Abbreviations

BE – Band-edge

CB – Conduction band

CdTe – Cadmium telluride

CIS – Copper indium disulphide

CM – Carrier multiplication

$CuInS_2$ – Copper indium disulphide

DSSC – Dye sensitised solar cell

DDT – Dodecanethiol

DLS – Dynamic light scattering

EDT – Ethandithiol

EDX – Energy dispersive x-ray spectroscopy

E_F – Fermi Level

E_g – Energy band-gap

FRET – Förster/Fluorescent resonance energy transfer

FWHM – Full width at half maxima

k_B – Boltzmann constant

MEG – Multiple exciton generation

MPA – Mercaptopropionic acid

NC - Nanocrystal

NMR – Nuclear mangetic resonance

PL – Photoluminescence

PLQY – Photoluminescence quantum yield

PV – Photovoltaic

QCE – Quantum confinement effect

QD – Quantum dot

QDSSC – Quantum dot sensitised solar cell

QY – Quantum yield

SEM – Scanning electron microscopy

VB – Valence band

XRD – X-ray diffraction

ZnS – Zinc sulphide

Acknowledgements

This project has been exciting, challenging and thoroughly rewarding and I am proud of the work that has been produced. As such, I would like to take this opportunity to share my gratitude with a number of people. First of all, thank you to my two supervisors, Dr Matthew Booth and Dr Lyudmila Turyanska, for your support and guidance over the past year. My friends, whose frequent distractions made University one of the best experiences of my life. And finally, my family. You've supported me through thick and thin and I would not have been able to accomplish anything had it not been for you.

ABSTRACT

Quantum dots have emerged as highly promising candidates as the next generation of photovoltaic material due to their tuneable optical properties, carrier-multiplication effects and long exciton recombination times. Recently, they have also exhibited their commercial viability as they can be fabricated using cheap and non-toxic precursors with facile and scalable production methods. One material that has displayed these features but yet to be fully understood is $CuInS_2$.

For QD materials including $CuInS_2$, the surface chemistry plays an integral role in the properties of the quantum dots. Particularly, the presence of surface defects (or trap states) can result in non-radiative emission. Colloidal QDs were synthesised with a surrounding layer of organic molecules, which partially passivate surface defects and solubilise nanocrystals (NCs) in a solvent. A widely used approach for further passivation of the surface states is to surround the NC with an inorganic shell. The material used for passivation could have a wider band gap and comparable lattice constant. The inorganic shell also provides protection from photodegradation. Therefore, this work involves synthesising colloidal $CuInS_2$ QDs using a solvothermal method and investigating the effect of the inorganic shell and organic ligands on their properties.

In this work, optical and morphological properties of $CuInS_2$ quantum dots were explored. Measurements of the PL (peak position, intensity and FWHM) and absorption were performed to investigate the effect of QD morphology and compare their properties. Surface passivation with ZnS resulted in a blue-shift of PL emission, possibly indicating the presence of the inorganic shell lead to an increase in the strength of carrier confinement, which is consistent with the alignment of their band structure. Conversely, the ligand replacement with shorter carbon-chain molecules lead to red-shift of the PL emission, indicating weaker confinement. Time-resolved PL measurements were also conducted which indicated the photostability of the quantum dots under ultraviolet light; photodegradation under the solar spectrum would prohibit the use of a material as a photovoltaic. In addition, time-resolved photoluminescence measurements allowed for determination of the lifetime of the exciton, from which the presence of defect states could be inferred; more defect states would provide more recombination pathways and thus a faster recombination rate, which is detrimental to photovoltaic applications. Morphological properties such as the size of the QDs were estimated using dynamic light scattering and scanning electron microscopy probed the surface of the QD. NMR was conducted in order to confirm the success of the ligand exchange.

Chapter 1: Introduction

1.1 Introduction to Photovoltaics

In recent years, there has been a drastic increase in global demand for energy, which is only expected to increase further as countries develop economically and populations continue to rise [1]. However, our reliance on fossil fuels such as oil and gas must begin to wane as these sources inevitably become exhausted and we must focus on sustainable methods of energy generation, including wind and solar cells. Due to the abundant nature of solar energy, photovoltaic (PV) technology has emerged as one of the most promising candidates to reliably adhere to large demands. In fact, the amount of energy provided by the sun irradiating the Earth in one hour is equivalent to the amount of energy consumed globally in a single year [2]. If 0.1% of the Earth's surface was covered with solar cells of an efficiency of 10%, our present needs would be fulfilled [3]. Therefore, there is a clear potential for the use of solar power and as such, the development of novel materials for photovoltaic applications is paramount for the future of sustainable energy production methods.

Today's PV market is comprised of two types of PV devices, first- and second-generation, with the third-generation currently in research and development. The differences in the generation are attributed to the technology utilised in order to convert solar energy directly into electricity. For first-generation PV cells, the photoelectric effect is employed. First observed by Heinrich Hertz in 1887 and explained by Albert Einstein in 1921, the photoelectric effect is the extraction of electrons from atoms they were previously bound to as a result of light incident upon it [4]. A semiconductor, whose conductivity is intermediate between metals and insulators, has a forbidden region in-between the valence band (VB) and conduction band (CB) which the electrons move through in order to be excited to higher states (and escape the atom from which they are bound) (see Figure 1 [5]).

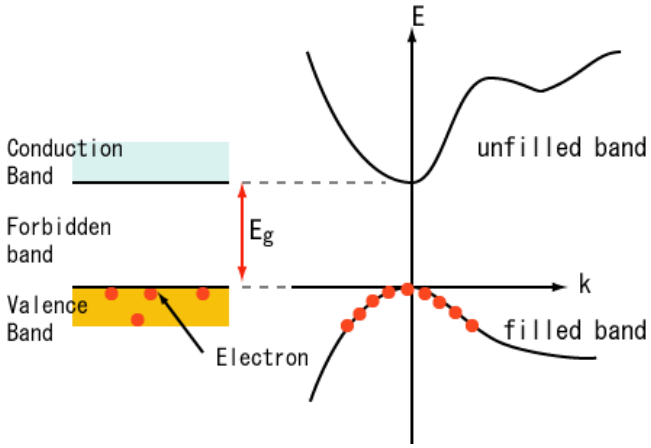

Figure 1: Diagram of the electronic structure of direct band-gap semiconductors, where E_g is the optical bandgap and k is the wavevector. Reproduced from: Kei [5]

First-generation solar cells utilise a crystalline semiconductor (e.g. silicon), with one layer containing an n-doped semiconductor stuck to another, p-doped semiconductor, hence forming a p-n junction (see Figure 2 [6]). The n-type material contains an excess of negative charge carriers (electrons), with the p-type material having an excess of positive charge carriers (holes). Both charge carriers are able to move about the crystal's lattice freely and at the junction, n-type electrons diffuse across to combine with the p-type

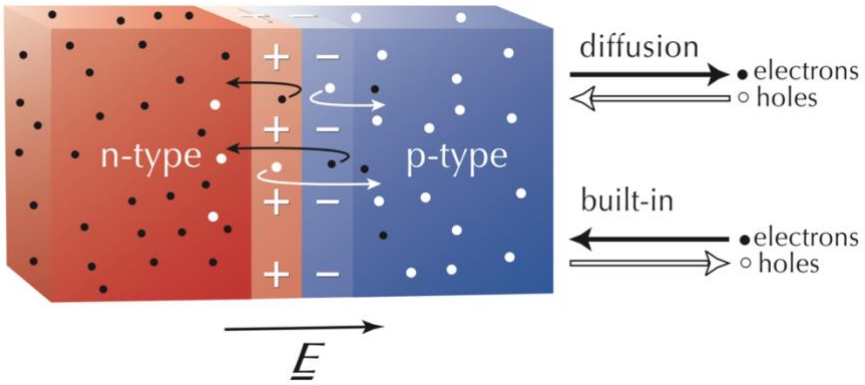

Figure 2: Illustration to show p-n junction formed from joining a p-doped and n-doped semiconductor. Reproduced from: Largent [6]

holes. Due to this diffusion, the n-type region close to the interface obtains a locally positive charge (as negative charge has moved away) and the p-type region close to the interface attains a locally negative charge. The layer between the n-type and p-type regions is known as the depletion region, since the charges have been cancelled out [7]. When a photon is absorbed inside the depletion region, the photo generated electron will move towards the n-region and the complementary hole will move towards the p-region. The highest reported efficiency of crystalline Si-based solar cells is 26.7% [8]. However, the limitation of first-generation solar cells can be attributed to high manufacturing and

processing costs, as well as the negative impact on the environment during fabrication. This paved the way for a new, second-generation solar cell.

Thin film technology was implemented in order to offset the high costs in production of first-generation solar cells by omitting the use of bulk material. However, the efficiencies of second-generation materials were significantly lower than their first-generation counterparts, so there remained a challenge of improving the efficiency without compromising the cost of them [9]. Cadmium telluride (CdTe) emerged as a candidate for thin film technologies, with a direct – and thus more efficient – band-gap and large absorption coefficient, with Rangel-Cárdenas et al [10] reporting 10^4 cm^{-1}; absorbing approximately 92% of visible light in a thickness of 1 μm. However, cadmium is a toxic material and as such, its commercial applicability is severely hindered [11].

Third-generation solar cells are tasked with superseding the efficiency of previous technologies, whilst keeping manufacturing and processing costs low, with materials such as perovskites and dye sensitised solar cells (DSSCs) providing possible solutions. Perovskites, commonly hybrid organic-inorganic lead or tin halide-based materials, are cheap and possess properties that would make them suitable for use in solar cells such as broad absorption spectrums and long carrier separation lifetimes, which allows for greater opportunity of extracting the electron to the external circuit. To date, the highest solar efficiency was achieved by Oxford PV's perovskite-silicon tandem solar cell (active area 1 cm^2), which attained a 28% conversion efficiency [12]. However, long-term instability remains a problem and can lead to toxicity issues with lead-based perovskites; their breakdown forms a toxic and possibly carcinogenic product and lead itself is known to be a pollutant [13]. For all perovskites, the long-term instability is due to changes to their crystal structure upon heating which affects their performance. DSSCs form part of the thin-film solar cell branch and are promising due to their simple and low-cost fabrication, as well as low toxicity. The optically active dye is soaked onto the anode and the counter electrode is surrounded by an electrolyte. The dye absorbs the photons and produces excitons, with the electrons then extracted and passed from the dye to the anode where they are oxidised due to the presence of the external circuit. However, the issue with DSSCs is the low abundance and therefore high cost of the dye material, as well as issues with their long-term stability [14]. To date, the best performing dye material operated at a solar cell efficiency of 14.3% using an alkoxysilyl-anchor dye of ADEKA-1 and a carboxy-anchor organic dye of LEG4 [15].

Another novel material that has shown much promise are quantum dots (QDs); zero-

dimensional semiconductor crystals of nanometre scale whose properties can be tuned by changing the size of the QD.

1.2. Quantum Dots

1.2.1 Overview of Quantum Dots

Quantum dots are inorganic semiconductors on the nanoscale whose size is confined in all three spatial directions. They can be categorised by composition, such as binary III-V and II-VI QD semiconductors and ternary I-III-VI QD semiconductors. The former are made using elements from group III in the periodic table (e.g. aluminium and gallium) and group V (e.g. phosphorous and arsenic). II-VI QD semiconductors are made using transition metals in group II (e.g. zinc, cadmium) and group VI (e.g. selenium and tellurium). Ternary semiconductors show particular promise for future integration into photovoltaics as they provide a greater degree of freedom in compositions and can be manufactured without using heavy metals which are toxic to humans, but still produce QDs with similar optoelectrical properties.

As QDs are semiconductors, the Fermi-Dirac equation indicates that the conduction band is predominantly devoid of electrons at room temperature, with only a partial amount having the necessary thermal energy to occupy it. The probability that an electron is in a state with energy *E* is given by the Fermi factor:

$$f(n) = \frac{1}{e^{\frac{E-E_F}{K_B T}} + 1} \tag{1}$$

where E_F is the Fermi level, k_B is the Boltzmann constant and T is the absolute temperature [16]. The Fermi level describes the energy state within a material at a finite temperature, *T*, which has a 50% chance of being occupied. The Fermi energy is the highest occupied energy state at absolute zero. In other words, the Fermi energy is the Fermi level at absolute zero. As the temperature increases, the Fermi function (Equation (1)) determines the fraction of charge carriers above the Fermi Level. The probability that a hole with energy *E* is in the valence band is found using

$$f(p) = 1 - f(n) = 1 - \frac{1}{e^{\frac{(E-E_F)}{K_B T}} + 1} \tag{2}$$

In a semiconductor, the Fermi level is altered by impurities, both chemically and

structurally. These impurities can donate extrinsic electrons which behave as donor states between the conduction and valence band. For p-type semiconductors, the Fermi level lies closer to the valence band and for n-type semiconductors, the Fermi level lies closer to the conduction band. An intrinsic semiconductor possesses a Fermi level exactly midway in the band gap [17]. In QDs, the Fermi level increases as the electrons occupy higher energy states due to the same number of electrons occupying a smaller volume as shown in Equation (3).

$$E_F = \frac{\hbar^2}{2m}(3\pi^2 n)^{\frac{2}{3}} \tag{3}$$

where *m* is the effective mass of an electron and *n* is the density of the electrons (number per unit volume) [18].

Techniques for the production of QDs usually fall within one of two approaches: top-down or bottom-up (Figure 3 [19]). In the former, the bulk material is stripped down to zero dimensions using methods such as e-beam lithography or X-ray lithography. Alternatively, bottom-up procedures synthesise colloidal QDs from the self-assembly of precursors in a solution following chemical reactions, which include hot-injection and heat-up methods [20]. Solution-based colloidal syntheses offer large degrees of control over the morphology with selection of the coordinating surfactants and solvents of the particles, whilst minimising particle polydispersity [21].

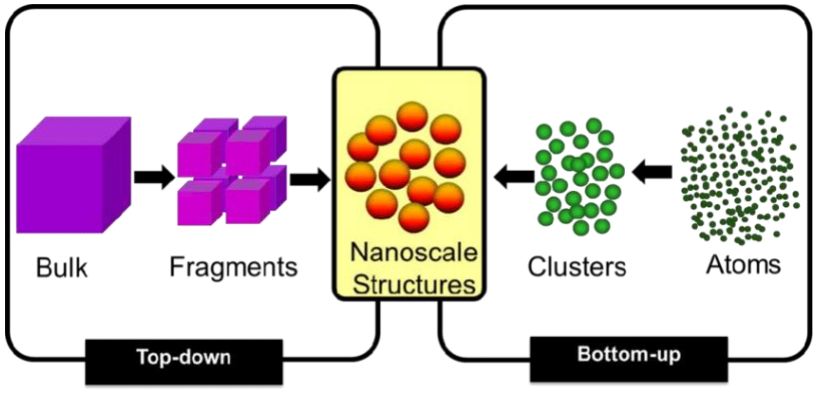

Figure 3: Illustration depicting top-down and bottom-up methods for the synthesis of nanocrystals. Reproduced from Some [18]: Some, 2018.

The hot-injection method rapidly injects the reagents into a hot solvent to nucleate

homogeneously. Nucleation occurs when a number of monomers surpass the energetic barrier required in order to form an ultra-small cluster which is thermodynamically stable; determined by the change in Gibbs free energy:

$$\Delta G = n\left(\mu_{Crystal} - \mu_{Solution}\right) + 4\pi r^2\sigma \quad (4)$$

Where *n* is the number of atoms, $\mu_{Crystal}$ is the chemical potential of the crystal phase, $\mu_{Solution}$ is the chemical potential of the solution phase, and $4\pi r^2\sigma$ represents the total surface energy, with σ the surface tension and $4\pi r^2$ the surface area of the cluster.

When a cluster is formed, if $\mu_{Crystal} < \mu_{Solution}$, then the change in free energy is greater than zero and the cluster is unstable, thus a stable interface is not possible between the cluster and the surrounding medium. However, once the cluster reaches a critical size, r_c, the change in free energy is negative, and the cluster is stable as the energy gained by creating the volume is sufficient to maintain a stable interface between the cluster and surrounding medium [22].

Following nucleation, the growth of the QDs is controlled with diffusion; larger particles grow more slowly than smaller particles. Conversely, the heat-up method gradually heats the precursors in the presence of ligands in a single, one-pot method. The resulting crystals are more polydisperse with a larger size distribution than the hot-injection since there will be numerous nucleation events occurring at different times. However, with the heat-up method, the process is far simpler, cheaper and can easily be scaled up in order to synthesise large batches of quantum dots. Furthermore, both methods of synthesis can be done colloidally; whereby the growth can be more accurately controlled and the size distribution more evenly distributed.

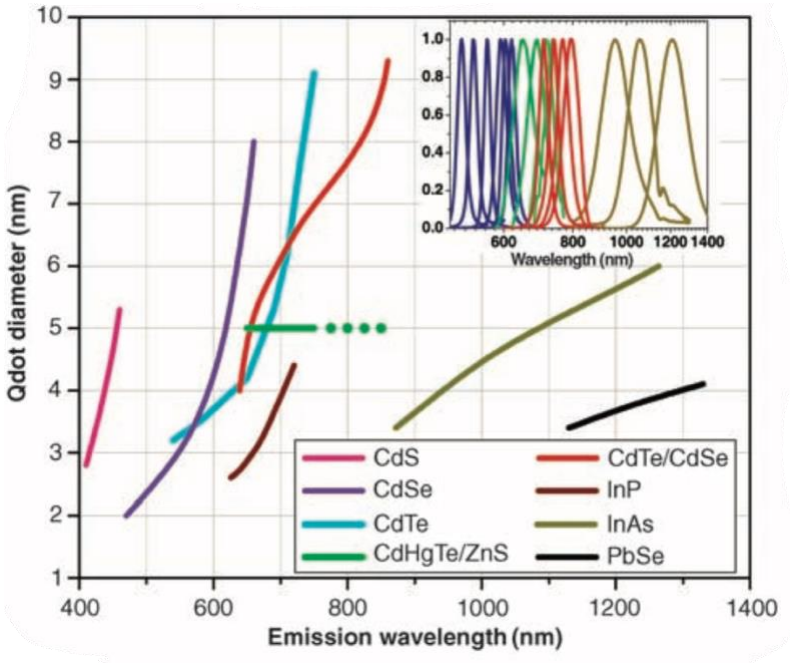

Figure 4: Figure to show tuneable photoluminescence of QDs by composition and size: Reproduced from: Michalet [21].

The size of the QD has significant effects on the PL emission of the QDs and so control over the size during synthesis is crucial. The composition of the QDs also affects the PL emission of the QDs. For QDs of different compositions, CdS QDs have optical emission at the highest energy and PbSe QDs at the lowest energy photons during exciton recombination (Figure 4 [23]). All QD composition types show the trend of increasing emission wavelength photons with greater QD size, though the rate is different in each. For example, in CdS, small changes to the QD size has much less of an effect than in PbSe, whereby a small increase to the size of the QD significantly increases the wavelength of the emitted photon [23].

The success of QDs in photovoltaics relies on the production of QD solids with low defect concentrations and efficient charge carrier transport. Therefore, several approaches are being considered to overcome the limitations facing QDs. For example, a counter measure to the trapping effect at the surface is to coat the QD core with an inorganic material to act as a shell, such as zinc sulphide (ZnS), with the passivation transferring the surface defects to the outer layer of the inorganic shell. This is due to atoms at the QD surface with unbonded electrons resulting in “dangling bonds”, which are ambiphillic and thus provide sub-bandgap, alternative recombination routes that reduce the exciton lifetime. Coating with a wider band gap semiconductor reduces the number of unsatisfied

valences in the QD. This has been shown to vastly increase the photoluminescence quantum yield (PLQY) by decreasing non-radiative recombination losses [24]. However, passivation with a large band gap material could have detrimental effects on the charge transport between neighbouring QDs, as the charge carriers could become trapped within the shell with their probability to tunnel decreased [25].

The capping ligands on QDs also play a significant role in their charge transport performance, since the length and type of ligand determine the spatial separation between QDs and by extension the tunnelling barrier height or hopping mechanism for charge carriers. Ligands are generally required in the synthesis to prevent particles from aggregating and provide colloidal stability. However, these are organic, long-chain ligands which increase the space between quantum dots, thus hindering their conductive efficiency (Figure 5 [26]). However, ligand exchange procedures have successfully been completed which substitute long-chain ligands for shorter chain ligands, such as ethanedithiol (EDT) or mercaptopropionic acid (MPA), thus decreasing the distance between QDs [27]. In a paper by Yun et al. [28], the film mobility of the holes increased from 4.33×10^{-5} $cm^2V^{-1}s^{-1}$ to 1.65×10^{-3} $cm^2V^{-1}s^{-1}$ after substituting long chain ligands with shorter chain ligands in copper indium selenide (CISe) QDs.

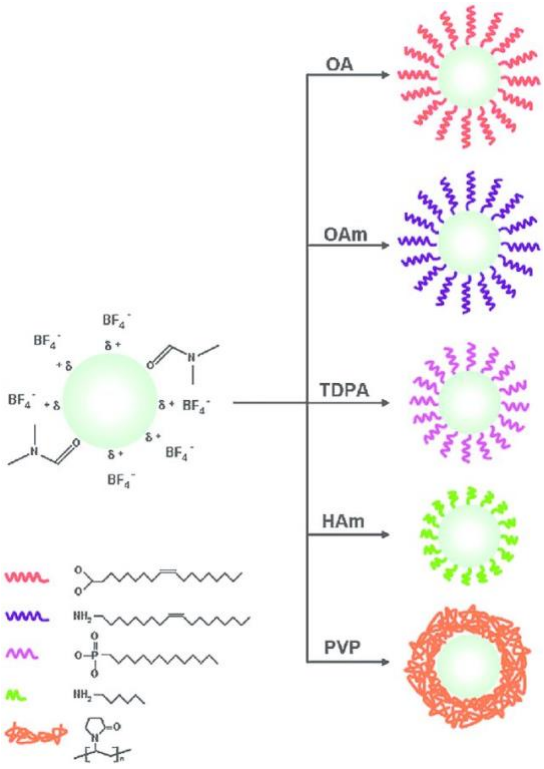

Figure 5: Illustration to show possible ligand exchange reactions. Left: Quantum dot with as-synthesised ligand attached and examples of ligands below. Right) QD surrounded by new ligands. Reproduced from: Sedlmeier [24].

1.2.2. Properties of Quantum Dots

QDs have garnered much interest for their applicability in photovoltaics due to their properties, such as tuneable optoelectrical properties, carrier multiplication effects, long exciton recombination times and low-cost fabrication methods [29]. To fulfil third-generation photovoltaic criteria, the efficiency of solar cells must be increased without proliferating the cost and if possible, reducing the price. Whilst there are some QDs that are produced using expensive and toxic precursors, such as lead and cadmium, there are other types of QD that use abundant (and therefore usually cheap) and non-toxic materials, such as carbon/graphene and zinc. These precursors can then be synthesised in a colloidal solution cost-effectively (i.e. using a heat-up method [30] which gradually heats the precursors in the presence of a ligand), which provide reasonable control over their size and composition. The synthesis and duration of QD growth time is imperative, since this is how the properties - such as absorption and band gap – are tuned.

A particularly auspicious property of semiconductors which is even more abundant in quantum dots (due to confinement) is multiple exciton generation, whereby a single high energy photon is capable of producing multiple excitons or several low energy photons

are still capable of producing an exciton. In current PV devices, there are two dominant energy loss mechanisms. The first being the non-absorption of photons with $E < E_g$ of the semiconductor, since the energy would be insufficient to produce an exciton. Secondly, for a photon with $E > E_g$ of the semiconductor, the excess energy results in the rapid cooling of the charge carriers, with some of the initial photon energy lost as heat. Shockley and Quessier evaluated the theoretical limit for single-junction PV devices to a maximum power conversion efficiency of 33.7% [31].

However, there are concepts capable of counteracting these loss mechanisms. For example, photon up-conversion mechanisms allow for the energy from sub-threshold photons with $E < E_g$ to be recovered; creating one higher energy photon from multiple (≥2) transmitted photons. Other mechanisms target the rapid cooling from high energy photons. A common approach to reducing losses from rapid cooling is employing multi-junction PV devices using semiconductors of different band gaps. Furthermore, carrier multiplication (CM) effects have successfully been exhibited whereby the energy from photons with $E > 2E_g$ is distributed among multiple charge carriers producing multiple excitons. This phenomenon is called multiple exciton generation (MEG). Following a MEG process, the electron-hole pair either recombine in a non-radiative process and transfer their energy to an additional charge carrier (Auger Recombination) or dissociate into free charges which can be extracted [32]. The implication of MEG is that one high energy photon can produce multiple excitons or, alternatively, the energy from a photon with $E < E_g$ can still be harvested and be used to produce an exciton (with absorption of another photon).

1.2.3. Quantum Confinement

Size-tunable properties of QDs are a result of quantum confinement, where charge carriers are limited to a “quantum box”; below a critical rate (twice the size of the Bohr radius), the electronic density of states becomes quantised from the bulk material’s continuous band to atom-like discrete energy levels (see Figure 6 [33]). The extent of the quantum confinement effect (QCE) is established by the diameter of the semiconductor crystallite. As the size of the QD decreases, a larger QCE is observed. In other words, the confining region decreases and the bandgap widens, thus shorter wavelength light is emitted [34].

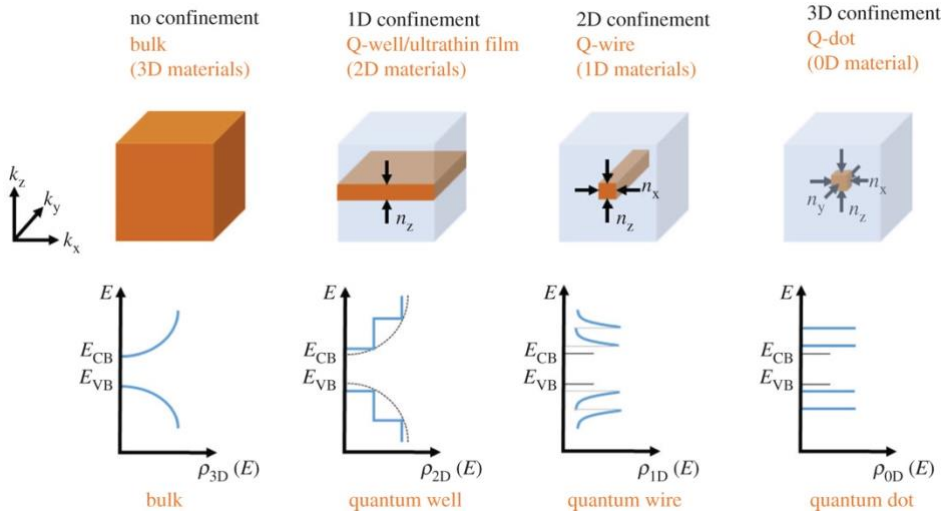

Figure 6: Illustration of the density of states in 3D, 2D, 1D and 0D materials. Reproduced from Edvinsson [31].

When a QD is excited by electromagnetic radiation, electrons are promoted to higher energy levels and leave behind a hole. However, upon relaxation to the ground state, QDs emit photons; the energy of which is dependent on the size, composition and shape of the QD. The electron's wavefunction, $\Psi(x,t)$, can be used to calculate properties of the electron as a function of position, *x*, and time, *t*. Upon normalisation, $|\Psi(x,t)|^2$, the probability of finding the electron at a given position can be found. Outside of the quantum dot, the potential energy, $V(x)$, is infinite such that $\Psi(x,t) = 0$ outside; thus there is zero probability of finding it there. Hence, nodes (positions of zero amplitude) are found at the QD boundary [35].

Quantum dots can be modelled as a particle in a box; a theoretical construct from quantum theory in which a particle is bound to a region. In this case, the electron and hole within the semiconductor nanocrystallite. In one dimension, with a box of side lengths *a*, the potential energy is zero inside the region and infinite outside:

$$V(x) = \begin{cases} 0, \ if \ 0 < x < a \\ \infty, \ otherwise \end{cases} \tag{5}$$

Equation (5) can also be rewritten in three dimensions for further accuracy:

$$V(\vec{r}) = \begin{cases} 0, \ if \ 0 < x < a_1 \quad 0 < y < a_2 \quad 0 < z < a_3 \\ \infty, otherwise \end{cases} \tag{6}$$

where a_1, a_2 and a_3 represent the three spatial dimensions. Using this representation,

Schrodinger's equation can be solved to calculate the energy of the QCE

$$\frac{-\hbar^2\nabla^2}{2m}\psi(\bar{r}) + V(\bar{r})\psi(\bar{r}) = E\psi(\bar{r}), \tag{7}$$

where $\hbar$ is the reduced Planck Constant, ∇ is the divergence, m is the mass of the QD, $\psi(\bar{r})$ is the wavefunction in three dimensions, and E is the energy. The equation can be rewritten in terms of each dimensional coordinate and then solved via separation of variables, leading to the QCE:

$$E_i = \frac{\pi^2\hbar^2}{2ma_i^2}n_i^2 \tag{8}$$

where i is the state (i.e. i = 1 refers to the ground state) and n_i is an integer quantum number for each dimension and ≥ 1.

However, we can rewrite the energy equation to account for spherical quantum dots (rather than cuboidal) and to account for the electron-hole pair.

$$E_i = \frac{\pi^2\hbar^2}{2m_e^*R^2}n_i^2 + \frac{\pi^2\hbar^2}{2m_h^*R^2}n_i^2 \tag{9}$$

where m_e^* and m_h^* are the effective masses of the electron (0.16 m_e^* for $CuInS_2$) and hole (1.13 m_h^* for $CuInS_2$) [36], respectively, and R is the radius of the QD. The ground state energy, n = 1, of the QDs is therefore:

$$E_i = \frac{\pi^2\hbar^2}{2m_e^*R^2} + \frac{\pi^2\hbar^2}{2m_h^*R^2} \tag{10}$$

Using the ground state energy of the QD, as well as the confinement energy of the QD, the equation for the energy bandgap can be found. One further consideration is that QDs do not move within a vacuum (which is an assumption of the particle in a box model), but inside bulk semiconductor crystals. As such, the energy gap of the bulk material determines the ground state energy of the system. In addition, there is an additional component that arises due to the attraction between the oppositely charged electron and hole:

$$E_{g\,(QD)} = E_{bulk} + \frac{\pi^2\hbar^2}{2R^2}\left(\frac{1}{m_e^*} + \frac{1}{m_h^*}\right) - \frac{1.786e^2}{\varepsilon R} \tag{11}$$

where E_{bulk} is the energy bandgap of the bulk semiconductor material and ε is the permittivity (for optical CIS $\varepsilon = 6.3 - 7.8$ Fm^{-1} and static $\varepsilon =$ 10.2 Fm^{-1}) [37-39]. From literature, the size of the QD should decrease as the PL peak wavelength position increases, as shown from the work by Booth et al. [39] in Figure 7.

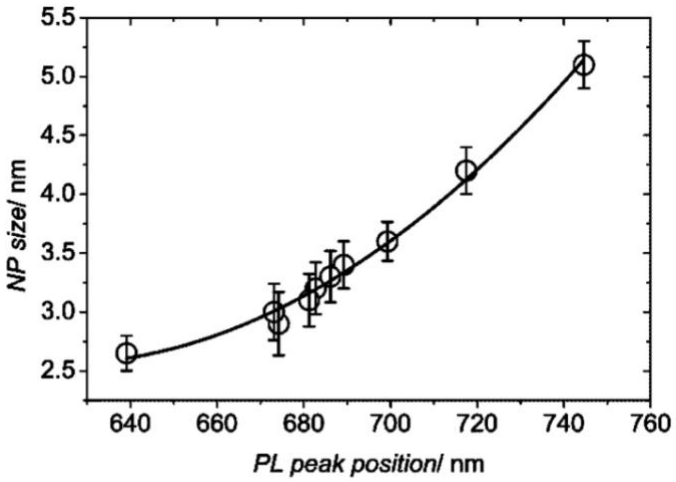

Figure 7: Plot of quantum dot size per PL peak position. Reproduced from Booth [37].

1.2.4. Copper Indium Disulphide Quantum Dots

Among the ternary semiconductors are copper indium disulphide (CIS), $CuInS_2$, nanocrystals whose absorption can be tuned from ultraviolet to visible light and emission tuned into the infrared. CIS is a direct bandgap semiconductor with a band gap of 1.53 eV and a Bohr exciton radius of 4.1 nm [40]. CIS QDs have a tuneable band gap of approximately 1.7 eV to 3.3 eV for size ranges between 6 nm to 1 nm, respectively [41]. However, other morphological aspects, such as composition, also directly alter the properties of QDs. For example, in CIS nanocrystals the valence band, comprising of copper 3d and sulphur 3p orbitals, reduces with copper deficient QDs; thus, widening the band gap [42].

Absorption spectra for CIS QDs are without sharp excitonic peaks, but display shoulders, likely contributed to by large size distributions and defect-related emission. The PLQY for CIS QDs is typically very low; often reported at 1% [43]. The emission spectra are broad, with full width at half maxima (FWHM) values ranging from 90 – 150 nm [44]. The Stokes shift is characteristically large at 130 nm – 170 nm and the fluorescent decay times are in the order of hundreds of nanoseconds, likely due to a large presence of defect states [43]. The work by Li et al. [45] produced CIS QDs with a PLQY of 8% and found that coating the QD with a zinc sulphide increased the PLQY up to 60%. ZnS is

effective as a shell material for CIS QDs for multiple reasons. Firstly, it is a large band gap (3.6 eV [46]) semiconductor which exhibits a type I band alignment with CIS, thus electrons and holes are confined to the QD core [25]. Furthermore, there is relatively low lattice mismatch between the two semiconductors (2 – 3%), owing to the fact that the crystal structure of CIS is derived from zinc blende, where Cu and In ions replace the Zn ions. Therefore, the ZnS shell can epitaxially grow on the $CuInS_2$ core and efficiently reduce the number of surface defects [47]. The additional benefit of using this material is that ZnS is non-toxic and is chemically stable.

For CIS QDs, a solvothermal, heat-up method can be employed in order to grow them. By modifying the reaction time, Frank et al. [48] produced $CuInS_2$ QDs with a band gap ranging from 1.55 eV with the quickest synthesis (3 h) to 1.44 eV with the longest synthesis (48 h). The sizes of the QDs were estimated using X-ray diffraction (XRD) and the 3 h-fabricated QDs were 39 nm ± 4 nm and the 48 h-fabricated QDs were 9 nm ± 1 nm. During the solvothermal method, a solvent in moderate to high pressure and temperature facilitates the reaction between precursors (copper, indium and sulphur) during synthesis, with the solvent adjusting the balance between the reactivity of copper and indium towards sulphur [49].

The charge transport mechanism in ordered solid films of CIS QDs has yet to be fully explored or understood. Properties such as interparticle spacing, doping, defects and electrode surface are known to directly impact the charge transport [50]. In CIS QDs, the existence of two anions and two cations increases the likelihood of defect states

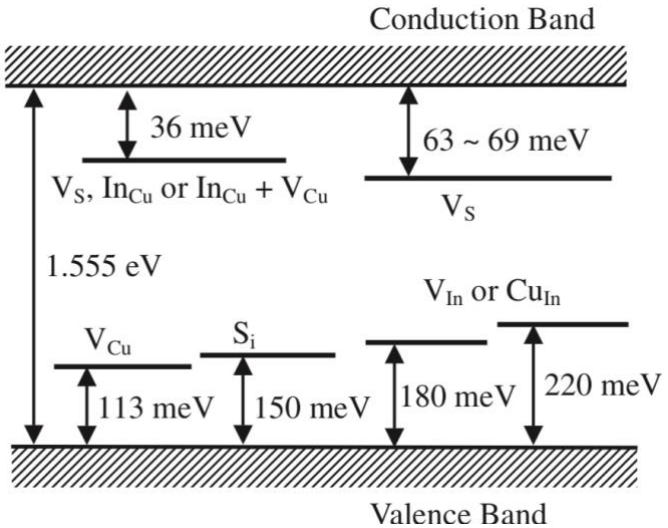

Figure 8: Illustration showing electronic band structure of CuInS2 nanocrystals including donor and acceptor states due to vacancies or substitutions. The donor levels: VS, InCu and VCu are sulphur vacancies, indium-substituted copper sites and copper vacancies. Reproduced from Onishi [49].

which can directly impact the charge transport through tapping effects and acting as electronic dopants. For example, cation vacancies (V_{Cu}) and a Cu^{+} cation occupying an In^{3+} site (Cu_{In}) act as acceptor states that allow for p-type transport. Alternatively, anion vacancies (V_S) and an In^{3+} cation occupying a Cu^{+} site (In_{Cu}) act as donor states that enable n-type transport (see Figure 8 [51]). However, the large number of native defects presents opportunity in that, if properly controlled, the doping levels and transport polarities could be tuned in a similar manner to other tuneable properties. In fact, harnessing control of the defect states within CIS QDs could complement or replace traditional methods of defect-state counter measures, such as surface passivation [28].

There are a number of mechanisms governing the absorption and emission in $CuInS_2$ nanocrystals, depending on the morphology and condition of states and defects. However, it is important to note that the precise nature of the transitions remains debated.

In CIS QDs, QD absorption (excitation) is primarily a result of the VB-CB transitions, with some papers arguing the emission (relaxation) is due to the radiative recombination of the CB electron with a hole positioned in an intragap Cu_x state, where x = 1+ or 2+ [52] (see Figure 9 [52]). Previous bulk and QD Cu-doped II-VI material studies have demonstrated a substitutional Cu^{2+} defect can be regarded as an active state occupied by a permanent hole, which would be able to couple to a band-edge CB electron through a radiative transition resulting in slow-decay; the electron is then transferred non-radiatively to the valence band [53]. The Cu^{1+} state is also a radiative defect, but

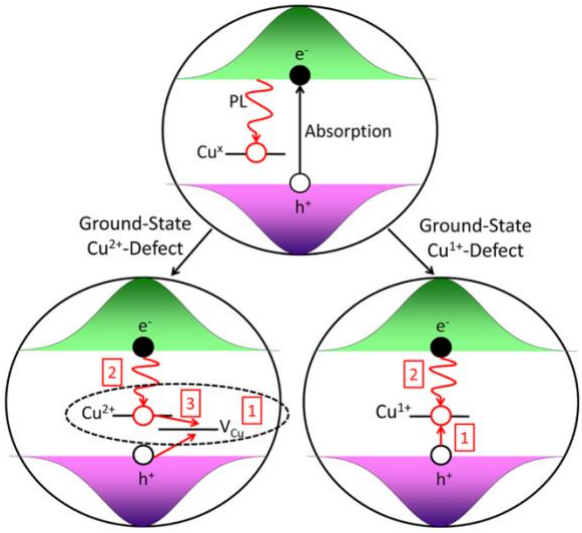

Figure 9: Illustration showing the exciton recombination routes in Cu-defect CuInS2 QDs. Reproduced from Fuhr [50].

necessitates a prior activation by capture of a photoexcited VB hole; thus is said to be optically passive. In this case, if the photogenerated holes are long-lasting, the emission of the QDs should be dominated by band-edge (BE) transition; a process faster than transitions involving Cu sites [52].

1.3 Quantum Dot Sensitised Solar Cells

Quantum dot sensitised solar cells (QDSSCs) are derived from conventional dye sensitised solar cells (DSSCs) which are constructed using two separate electrodes; namely, the photo-anode and the counter electrode with a suitable electrolyte in between the two electrodes. The photo-anode is assembled on a transparent conductive substrate by deposition of a large band-gap semiconductor, followed by the deposition of a layer of optically active sensitised dye. The longevity and commercial applicability of DSSCs is somewhat limited, however, owing to the limited efficiency due to narrow absorption ranges and low thermal and long-term stability. By replacing the optical dyes with QDs, these shortcomings are expected to be overcome and increase the efficiency of these solar cells [54].

In QDSSCs, solar energy incident upon the cell is absorbed by the QDs and produces excitons, assuming the photon has sufficient energy when absorbed by the QD. With the exciton produced, the electron and hole are separated. The electron is then transported to the external circuit via the CB of the semiconductor and the hole is transported to the external load via the Red-Ox coupled electrolyte where it is reduced. However, there are multiple pathways that allow exciton recombination, which is detrimental to the efficiency of a QDSSC, as shown in Figure 10 [55].

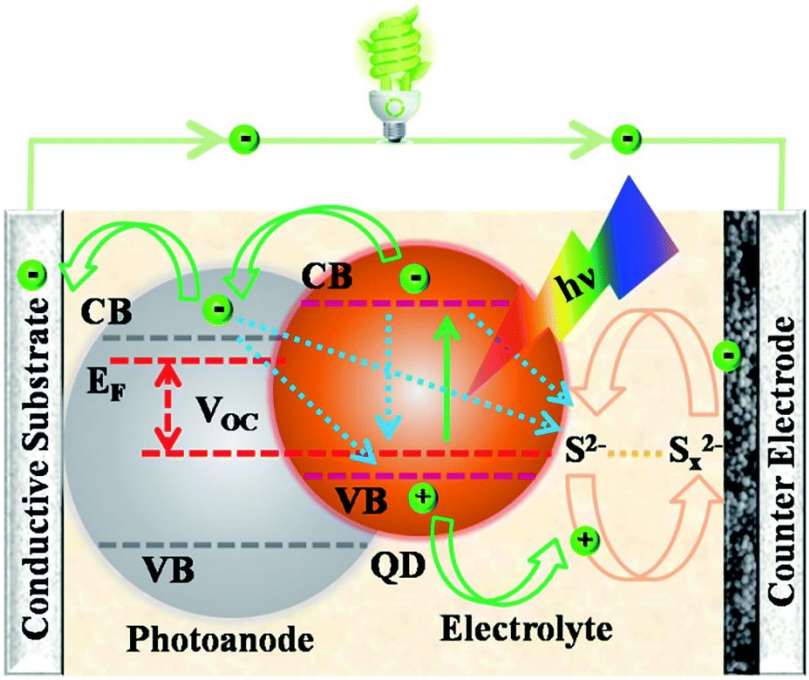

Figure 10: Illustration of working quantum dot sensitised solar cell. Desired mechanism shown with green arrows. Possible recombination routes shown with blue arrows. Reproduced from Ye [53].

Upon the absorption of a photon, where the electron in the QD is excited to the conduction band and the hole is in the valance band, the first possible recombination pathway is within the QD itself. The electron can recombine with a hole in an intragap state, since this is more energetically favourable than returning to the valance band of the QD. Alternatively, the electron in the CB of the QD could recombine with a hole in the electrolyte. If the QD successfully transitions to the CB of the large band gap semiconductor, there are still opportunities for it to recombine with a hole in the valence band or intragap state within the QD, or with a hole in the electrolyte.

1.4 Quantum Dot Solids

Quantum dot solids offer an alternative to QDSSCs as they inhibit the deterioration associated with the long-term stability of liquid electrolytes [56]. The means by which charge carriers move within a QD lattice is possibly due to a hopping mechanism; whereby electrons overcome potential barriers between neighbouring, localised states, depending on the barrier height and width. Alternatively, the mechanism could be quantum tunnelling where electrons penetrate through potential barriers depending on barrier width. Moreover, the conductivity within QDs is expected to follow two principles. Firstly, that there must be stable and partial occupation of the scarce and identifiable QD states and secondly, that the charges must be able to hop between such states in separate particles. However, there remains the possibility that the transport mechanism could also be intra-molecular, or band transport, where the movement of charge carriers is dictated by scattering events. Two separate studies on CdSe QDs and PbSe QDs proposed that as the temperature decreased the mobility increased, akin to the behaviour of metallic nanomaterial solids which show band transport, due to reduced scattering [57-59]. However, the trend of increasing mobility with decreasing temperature is the only evidence for band-like transport at this stage and hopping could also explain this trend due to the reliance on a temperature dependant factor (and has been shown that at above temperatures of $T = E_a / k_B$, where E_a is the activation enthalpy and k_B is the Boltzmann constant, the trend was demonstrated). Einstein showed this with the Einstein-Smoluchowski Relation

$$\mu = \frac{ed^2}{6\tau_{hop}kT} \tag{12}$$

Where μ is the mobility of the particle, e is the charge of an electron, d is the diffusion constant, τ_{hop} is the effective hopping rate, k_B is the Boltzmann Constant and T is the temperature [60]. In QD solids, the large degree of disorder makes band transport hugely unlikely. For example, there exists disorder in the energy levels owing to the quantum confinement effects, which scales with size, composition and size distribution. Similarly, there is disorder associated with the electron-electron repulsion in small QDs, though as the dot separation decreases, the disorder decreases. Finally, there is disorder in the coupling between the particles during ligand exchange, since this results in a new, inconsistent local arrangement. However, if the interparticle distance post ligand exchange reduces, then the coupling increases. At the same time, with the decreased distance, the likelihood of sintering between similarly order crystals increases, thus increasing the disorder.

However, whilst ample research has been devoted into colloidal QDs, aspects – such as the charge transport mechanism in QD solids - remain that require further understanding or overcoming. One of the critical features limiting their potential as viable photovoltaics are the trapping effects which provide pathways for nonradiative exciton recombination; likely arising from the defects within the QD or at the surface. As such, efficiencies of QD solar cells have thus far fallen below currently established generations, let alone QDSSC theoretical efficiencies that could reach upwards of 60% [61]. To date, the highest reported efficiencies of QDSSCs have surpassed 12%, with Jiao et al. [62] reporting a certified efficiency of 12.07% for ZnCuInSe-based QDs. The limiting factors surrounding the application of QDs as solar cells are the significant exciton recombination routes provided by defects states (thus reducing efficiency) as well as the electrolyte (hole transport material) coupled to the QD; where stability is poor and regeneration of the sensitizer is slow (which also limits efficiency) [63].

1.5 Aims and Objectives

The development of novel materials for photovoltaic applications is of paramount importance for the future of sustainable methods of energy production. Colloidal quantum dots (QDs) could offer exciting opportunities for the development of the 3rd generation of photovoltaics due to their tuneable properties, high processability and the fact that they are expected to overcome the efficiency limitations of current solar cells. Copper indium disulphide QDs were chosen due to their relative low-toxicity and low production costs. $CuInS_2$ QDs also have a long lifetime providing slow exciton recombination rates, hence favourable opportunity to extract the charge.

The aim of this research project is to investigate the effect of QD surface passivation with different organic ligands and an inorganic shell on optical and morphological properties of $CuInS_2$ QDs.

$CuInS_2$ QDs were synthesised using a simple, one-pot, solvothermal method with the intention of producing colloidal, stoichiometric QDs with a small size distribution. Following the synthesis, some of the QDs were coated with a zinc sulphide (ZnS) shell in order to passivate the core and remove trap states that are known to be common in $CuInS_2$ QDs. Of the coated QDs, a ligand exchange replaced the dodecanethiol (DDT) ligands from synthesis with short-chain mercaptopropionic acid (MPA) ligands to decrease the distance between the QDs.

Optical analysis was conducted on the three samples to probe their absorbance and emission features and consequently compare changes due to the effect of shelling or ligand substitution. This was done using absorption and photoluminescence spectroscopy, the latter of which also measured their photostability and photoluminescence decay rate.

Morphological analysis was conducted to identify information about the size, shape and composition of the different quantum dots. Dynamic light scattering (DLS) was used to measure the size of the QDs, scanning electron microscopy (SEM) was used to observe the large-scale morphology of drop-casted QD films and energy dispersive X-ray (EDX) spectroscopy provided compositional information, X-ray diffraction (XRD) probed the crystalline structure of the QDs and nuclear magnetic resonance (NMR) spectroscopy was used in order to confirm the success of the ligand exchange.

Chapter 3 covers the materials used and methods of the project; including synthesis of

the nanocrystals, growing the ZnS shell and the ligand exchange. In addition, the characterisation techniques are outlined and background information is provided as well as the set-up parameters used where necessary. Chapter 4 is the results and discussion where results and plots are shown and calculations have been used to find properties of the QDs such as radial size and optical bandgap. Finally, Chapter 5 is the conclusions.

Chapter 3: Materials and Methods

3.1. Materials

All materials were purchased from Sigma Aldrich and were used without further purification. Copper(I) iodide (>99.5%), indium(III) acetate (99.99%), zinc stearate, octadecane (ODE) (99%), dodecanethiol (DDT) (>98%), chloroform (>99.5%), hexane (95%), mercaptopropionic acid (>99%), dimethylformamide (99.8%), trimethylamine (99.8%), methanol (>99.9%) and acetone (>99.9%).

3.2. Synthesis and Ligand Exchange Methods

3.2.1. Synthesis of $CuInS_2$ Quantum Dots and Coating with ZnS

Measurements of precursors were made using an electronic balance (±0.001g). 0.382 g (2.0 mmol) copper iodide (CuI) and 0.583 g (2.0 mmol) indium acetate ($In(ac)_3$) were dissolved in 40 mL (122.1 mmol) octadecane (ODE) and 10 mL (41.7 mmol) Dodecanethiol for a final QD crystal Cu:In molar ratio of 1:1. The solvents (DDT and ODE) were in excess so as to more likely attain the required composition, since copper and indium differ in their reactivity towards sulphur and require balancing in order to form Cu and In metal-thiolate complexes prior to nucleation. Separate measurements of 2.537 g (26.0 mmol) and 3.790 g (38.9 m mol) were made of zinc stearate to grow the zinc sulphide shells during later synthesis.

The precursors were transferred to the 100 mL three neck round-bottom flask (Figure 11 – 12 [64]), situated inside the electronic heating mantle. A magnetic stirrer was then added to the flask and the solution was stirred for the duration of the synthesis. The mantle was heated to $T = 80°C$ for 30 minutes and monitored using a digital thermometer to fully dissolve the precursors in the solvent. The neck in which the precursors were entered was closed off with a cap but allowed for the thermometer to be submerged in the solution whilst maintaining the seal. The tip of the thermometer was placed in the deepest part of the flask. In the central neck, the reflux column was positioned to prevent the loss of any solvent due to evaporation. The reflux column had water-in and water-out apertures which helped cool the column, thus allowing for any evaporated solvent to condense and return to the reaction vessel. The tubes were clamped at the apertures in order to prevent spillages. The syntheses were performed under N_2 flow to remove as much oxygen from the system as possible. In the third neck, N_2 gas was bubbled into the solution by inserting a pipette into the end of a tube connected to the N_2 gas tap.

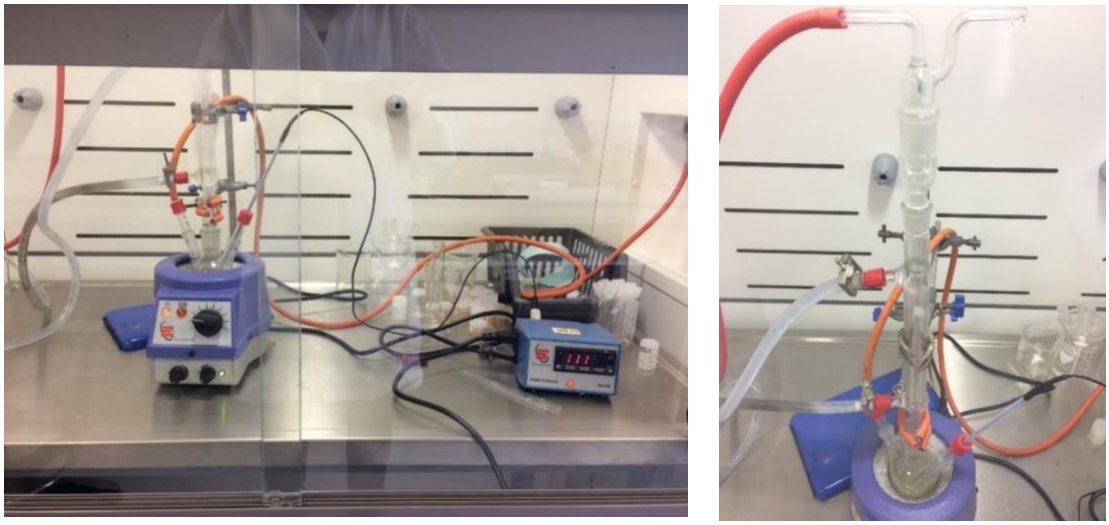

Figure 12: Left) Photograph of set up of colloidal synthesis of copper indium disulphide quantum dots. Digital thermometer (right) connected to the heating mantle (left) where the 100 ml three-neck round-bottom flask is situated. Right) Photograph of reflux column attached to flask: N_2 gas flow into top of the column, water-in and water-out apertures at the middle and bottom of the column, respectively.

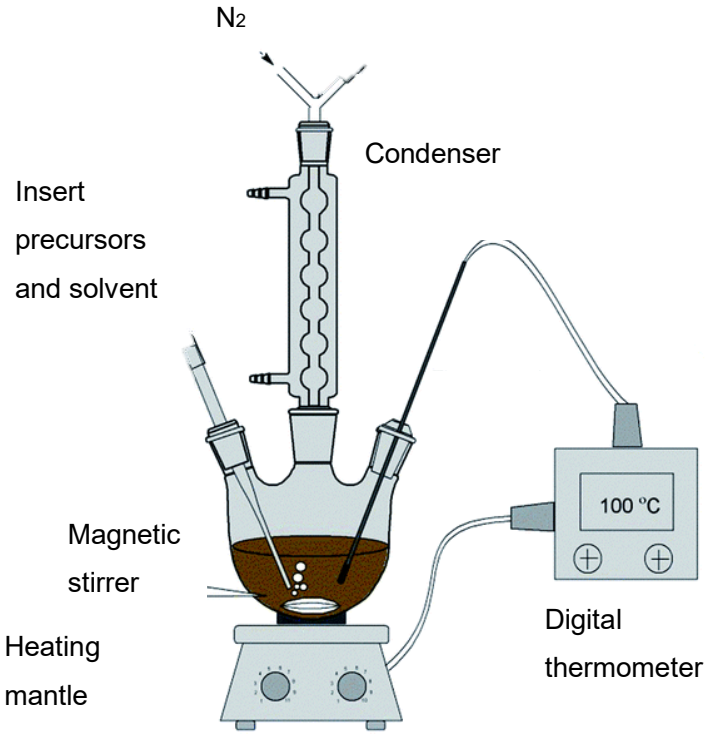

Figure 11: Schematic diagram for solvothermal synthesis of colloidal quantum dots. Reproduced from: Zhang [62].

Once dissolved, the colloidal synthesis method could begin, with the precursors heated at T = 120° for 30 minutes to allow for the metal-thiolate intermediates to form which function as monomers for nucleation of the nanocrystals. Afterwards, the temperature

was increased to T = 215°C for a further 30 minutes to begin the nucleation of the nanocrystals (mantle set to high heating rate). Some of the reaction mixture was removed after this time using a pipette and then 2.537 g zinc stearate was added to the ongoing reaction and remained heated at T = 215°C for 30 minutes. Another sample from the reaction mixture was then removed and a further 3.790 g zinc stearate was added into the flask and heated at T = 215°C for an additional 30 minutes. Then, the temperature was reduced to T = 190°C for 15 minutes and then reduced again to T = 180°C for a further 15 minutes. The two separate samples and reaction mixture were cooled to room temperature and stored at T = 6°C.

3.2.2. Purification of Quantum Dots

The samples were purified to remove unreacted precursors and obtain QDs dispersed in solvent. From one sample, 5 mL of QDs were pipetted into a 50 mL PTFE tube and a second 5 mL of QDs were pipetted into a different PTFE tube. The two PTFE tubes were both topped up to the 40 mL mark with methanol acetone 1:1 (in the centrifuge, this collected the impurities and separated the QD sample out). Methanol and acetone were used as cleaning agents as the QDs and surface ligands were not damaged and the unreacted precursors dissolved in the solvents and the QDs precipitated out. Before being placed in the centrifuge, however, the tubes were weighed. It was essential that the tubes were balanced within approximately 0.5 g of each other in order to prevent damage to the centrifuge. In the centrifuge, the tubes were placed on opposite sides so that the balance was as perfect as possible, and the lid was firmly secured. The settings were adjusted such that the spin lasted for 10 minutes at the maximum revolutions per minute (rpm) (in this instance 7830 rpm) at 5°C.

Following centrifugation, the QDs precipitated in the PTFE tube and solvent supernatant was discarded. The PTFE tubes were inverted on top of an absorbent (e.g. paper towel) to ensure all methanol acetone was removed from the tube. A small amount of hexane (approximately 10 mL) was then added to one tube. This was then shaken until the QDs had dissolved and then poured entirely into the second tube, which was again shaken until the QDs had dissolved. The washed sample was then pipetted into a new glass vial and labelled (including that it had been washed). The centrifugation process was repeated to purify the samples further.

3.2.3. Ligand Exchange using Mercaptopropionic acid

To decrease the distance between the QDs and thus improve the charge transport

between the QDs, the long-chain DDT ligands needed to be replaced with shorter ligands. 3-mercaptopropionic acid (MPA) is a hydrocarbon (three carbon chain) with thiol and carboxylic acid groups at either end (see Figure 13).

Figure 13: Diagram to show chemical structure of dodecanethiol (right) and mercaptopropionic acid (left)

With the same set-up as section 3.2.1, a pipette was placed inside one of the three necks of the flask and N_2 gas was blown through for approximately 10 minutes to remove oxygen from the reaction vessel. Afterwards, the gas was turned off with the neck remaining sealed with the pipette and separate syringe needles were then used to transfer 0.174 mL (2 mmol) mercaptopropionic acid (MPA) into 1 mL methanol (24.7 mmol) into the three-neck round-bottom flask. The QDs were washed via centrifugation and the precipitate was dispersed in 10 mL (124.8 mmol) chloroform and also transferred to the reaction vessel. A magnetic stirrer was placed into the flask and the thermometer from the digital heater was placed into one of the necks, with the central neck being used for the reflux column. Water and N_2 were again allowed to flow in the column in order to allow any evaporated products to condense and return to the reaction vessel.

The reaction was stirred for 2 h at room temperature with the mantle and afterwards the MPA-substituted were extracted using deionised water. Ethyl triamine was added dropwise until the QDs dispersed into the water. The QDs were stored at T = 6°C.

3.3. Optical Characterisation

3.3.1. Photoluminescence Spectroscopy

Photoluminescence (PL) spectroscopy was used to measure the optical emission of the QDs. High intensity light (200 nm < λ_{Ex} < 1700 nm) from an excitation source within the spectrometer is directed into an integrating sphere, where photons interact with the QDs. This causes excitation of an electron from the valence band into the conduction band and upon recombination of the electron and hole the photon is emitted with the energy equal to the energy gap (see Figure 14 [65]). The emitted photons are detected and a spectrum of the intensity of the emitted photons per wavelength is plotted, and is used

to estimate the optical band gap of the QD. However, in CIS QDs defects are known to be prevalent, thus the exciton recombination transition could occur via defect states. The probability of a photon being emitted is given by the photoluminescence quantum yield (PLQY) of the QD.

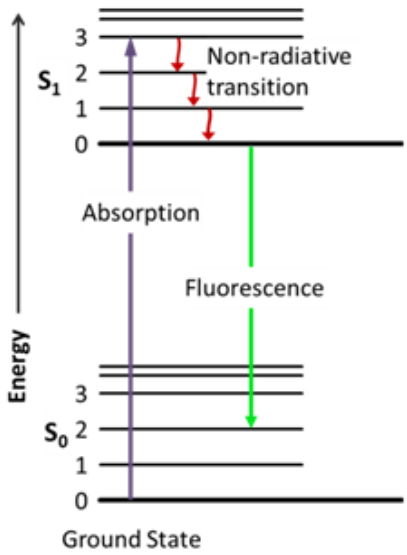

Figure 14: Diagram showing the processes and transitions during photoluminescence spectroscopy. Reproduced from: Teledyne Princeton Instruments [63].

Photoluminescence spectra were collected using an Edinburgh FLS980 spectrometer (see Figure 15 for schematic diagram). Data were acquired using the FLS980 spectrometer control software package. The QD sample was transferred to a quartz cuvette and positioned within the integrating sphere. The integrated sphere spatially integrates radiant flux and is constructed using a material with a reflectance > 99% over the spectral range of 400 nm to 1500 nm and a reflectance > 95 % within the spectral range 250 nm – 2500 nm. The λ_{ex} slit width was set to 3.00 nm and the λ_{em} slit width was initially set to 0.10 nm. The λ_{em} slit width was then adjusted until the signal caps of the emission signal was approximately $1x10^6$ caps s^{-1}, with the final λ_{em} slit width set to 0.15 nm. The slits were responsible for determining the amount of light able to reach the sample or detector, without compromising on resolution (due to slit being too wide) or the signal-to-noise ratio (due to slit being too narrow) with the monochromators determining the wavelength. The scanning range was set from 400 nm to 800 nm, with a step size of 1.00 nm and a dwell time of 1.00 s. The excitation wavelength, λ_{ex}, was increased from 400 nm in steps of 10 nm up to 590 nm for the core-only samples and

550 nm for the core/shell samples. Excitation was provided by the Xe1 Xenon Arc Lamp.

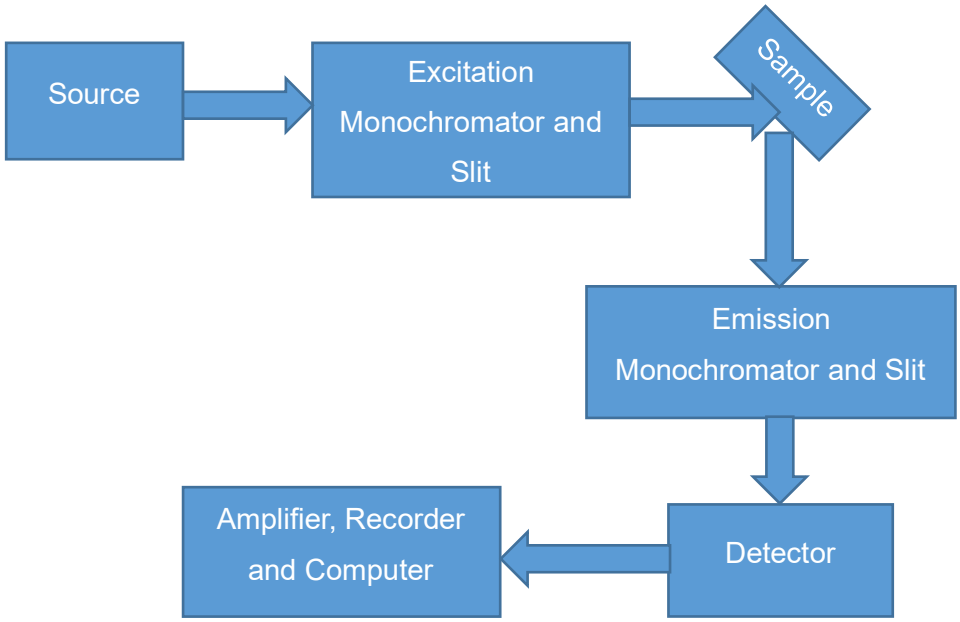

Figure 15: Diagram to show general schematic of photoluminescence spectrometer where the arrows indicate the path of light. Source: Xe1 Xenon Arc Lamp emits continuous light in the range 230 nm to 2600 nm which is then focused onto the excitation monochromator by an off-axis epsilloidal mirror. Excitation monochromator: ensure only the desired wavelength reaches sample with use of reflection gratings and computer controlled shutters ensures sample is not subject to prolonged exposure which could cause photodegradation. Slits: determine band pass of light incident on the sample and intensity of fluorescence from sample. Larger slit width reduces resolution but increases detected signal. Sample cell: excitation light source interacts with the sample housed in the sample holder and emits photons. Emission monochromator: ensures high resolution and minimizes diffraction of light. Amplifier and Recorder: count photons reaching the detector, whilst monitoring the Xenon lamp to ensure correct wavelength being emitted. Signal then passed to computer.

3.3.2. Absorption Spectroscopy

When light is incident upon a sample of QDs, the light can either be absorbed, transmitted or scattered (see Figure 16 [66]). Absorbance occurs when the incident light and QD sample have similar frequency of molecular vibration or when the energy of the incident light is similar to the transitions in electronic energy-level states within the QD. The absorbance of the sample is dependent on the path length through the QD suspension, as well as the concentration of the sample, as characterised by the Beer-Lambert law:

$$A(\lambda) = \varepsilon(\lambda)Cl \quad (13)$$

where $A(\lambda)$ is the absorption of the QD solution, $\varepsilon(\lambda)$ is the molar extinction coefficient of the QD (probability for an electronic transition), C is the concentration of the solution and l is the path-length of the light. When a photon of sufficient energy is absorbed by the QD, an electron is promoted from the VB into the CB. In absorption spectroscopy, the transmitted light is detected and from this the absorption profile is produced (as scattered light is assumed to be negligible), since the light that is not transmitted is absorbed.

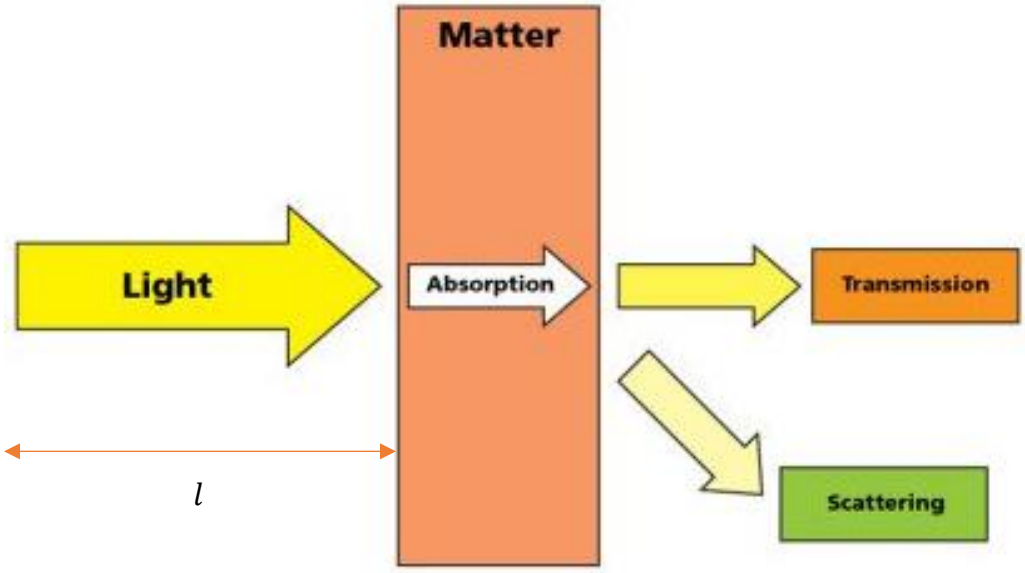

Figure 16: Diagram of light interactions with matter, where l is the path length. Absorption) Photon absorbed by QD sample and produces an exciton. Transmission) Light passes through QD sample without any interaction. Scattering) Light collides with QD particles which changes its direction. Reproduced from: Ocean Optics [64].

The absorption spectra of QDs presents the range of wavelengths that are absorbed. The first excitonic peak (i.e. the lowest energy) of the absorption spectra can be used in order to estimate the band gap of the QD, since this will reveal the band to band transition (rather than band to defect transition).

Absorbance spectra were recorded using the Edinburgh FLS980 spectrometer. Synchronous scans were taken of the samples and then absorption spectra were produced using the in-built absorbance analysis feature on the embedded FLS980 software. The sample was transferred to a quartz cuvette and positioned inside the integrating sphere. The integrated sphere ensures that almost all the transmitted light and scattered light is recorded at the detector, thus giving a more reliable absorption

spectrum (since the absorption is the light that does not reach the detector).

The λ_{ex} slit width was set to 4.00 nm and the λ_{em} slit width was initially set to 0.10 nm. The λ_{em} slit width was then adjusted until the signal caps of the emission signal was approximately 1x10$_6$ caps s^{-1}, with the final λ_{em} slit width set to 0.15 nm. The scanning range was set from 400 nm to 800 nm, with a step size of 1.00 nm and a dwell time of 1.00 s.

3.3.3. Kinetic Characterisation

To test the stability and decay rates of the QDs, time-resolved PL measurements were conducted. The stability measurements probed the sample with a constant wavelength and the decay rates were measured by opening and closing a shutter and measuring the PL response time of the QDs from max PL to zero.

The FLS980 spectrometer was used to assess the fluorescence times of the QDs. The excitation wavelength was kept constant for a given duration of time (300 s for stability). The change in the intensity of emitted photons was recorded. A profile of the PL intensity vs time was plotted (Figure 17 [67]). For use in photovoltaic applications, it is paramount that the semiconducting material does not readily degrade under UV to infrared wavelengths as this would make it unsuitable for actual use, hence decay times were also measured under UV excitation.

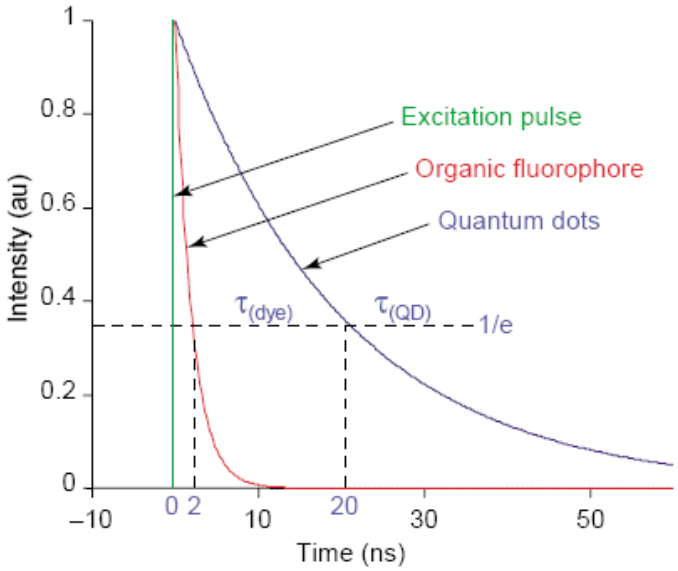

Figure 17: Diagram to show decay time of quantum dots using time-resolved photoluminescence. Reproduced from: Gao [65].

The QD sample was transferred into a cuvette and placed within the sample holder. The software package in conjunction with the FLS 980 spectrometer was used in order to setup decay parameters. Each sample was placed in the spectrometer for 300 s under wavelengths of 300 nm up to 500 nm, with the photoluminescent intensity outputted. Generally, the samples showed a large degree of stability. The core/shell sample was also deposited onto a glass slide and its stability measured, as this would more closely reflect the behaviour of the QD film within a PV device.

Time-resolved photoluminescence measurements were taken to measure the decay times of the QDs. Between the excitation source and sample, a shutter was intermittently opened and closed; with the PL signal at a maximum when open and zero when closed. Therefore, the lifetime of the QDs (i.e. the time for an exciton to recombine) could be measured as the PL would decay to zero when the shutter was closed after the PL was at maximum (where the maximum PL intensity was determined by λ_{Ex}= 400 nm for both samples). Origin was used in order to fit exponential decay fits to the data points, with time constants, τ, generated using the data fitting. The sample was again placed into the sample holder and the FLS corresponding software package was set to a lifetime scan, with the scanning time set at 20.00 s and the step time at 0.01 s.

3.4. Morphological Characterisation

3.4.1 Dynamic Light Scattering

Dynamic Light Scattering (DLS) is a technique whereby light of a single wavelength is directed towards the sample and scattered by the particles within the sample (see Figure 16). DLS uses the principle of Brownian motion - the random movement of particles due to collisions with solvent molecules - in a sample which can then be related to the size of the particles suspended in the liquid. Larger particles have slower Brownian motion, whereas smaller particles will move more rapidly. The size of the particle is determined from how a particle diffuses within a fluid, and as such is an approximation of the size called the hydrodynamic diameter (Equation 14), where the particle is modelled as a sphere with the same translational diffusion coefficient as the particle being measured. The rate at which particles are diffusing, as a result of Brownian motion, is determined by measuring the rate at which the intensity of the scattered light fluctuates. DLS produces a speckle pattern (intensity of light pattern), where dark points are visible where the phases of scattered light have destructively interfered and bright points appear where the phases constructively interfere. The rate at which the positions of the dark and bright points changes indicates how quickly the particles diffuse, with the intensity fluctuating

more with smaller particles.

$$d(H) = \frac{kT}{3\pi\eta D} \quad (14)$$

Where $d(H)$ is the hydrodynamic diameter, k is the Boltzmann constant, T is the temperature, η is the viscosity and D is the translational diffusion coefficient.

The hydrodynamic radius of the quantum dots was acquired using the Zetasizer Nano and 633 nm light with the detector measuring backscattered electrons at 173°. It was expected that 633 nm light would be partially absorbed by the QDs, but assumed the same across the different samples. The stock solution was filtered before being separated into 5 concentrations; with the concentration decreasing by 10-fold each time. The sample was pipetted into a cuvette and placed into the spectrometer such that the red light passed through. The parameters were set by selecting the type of quantum dots and the solvent, with known refraction index at a given temperature. The measurement was then repeated three times.

3.4.2. Nuclear Magnetic Resonance

Nuclear Magnetic Resonance (NMR) is a technique for analysing the composition and structure of organic molecules in solution. Using the knowledge that nuclei are electrically charged and most have spin, the application of an external magnetic field and radiofrequency (RF) radiation at a given frequency is sufficient in providing enough energy to stimulate an energy transfer from the ground state to a higher energy level (see Figure 18 [68]). The frequency of RF is dependent on a number of factors, such as the characteristic of the type of nucleus (e.g. $_{12}C$ or $_{13}C$) and secondly the chemical environment of the nucleus, since protons attached to different elements absorb at different frequencies. Finally, the RF frequency also depends on spatial location in the magnetic field if the field is not uniform everywhere.

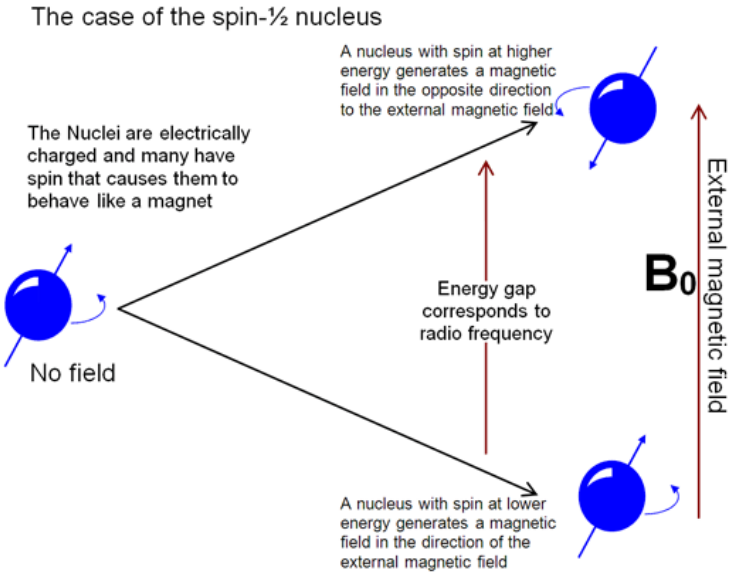

Figure 18: Energy level splitting from radio wavelength energy to show basic principle of nuclear magnetic resonance spectroscopy. Reproduced from: Gidron [66].

In a large magnetic field, a nucleus can swap between two energy states, though infrequently. However, if energy is applied to the nuclei with the same energy as the difference between both states (ΔE), the rate at which the nucleus changes between energy states is increased. The energy required to do so is in the RF range and is applied in short pulses. The absorption of RF energy to the nuclear spins causes excitation to higher states and relaxation to lower states, i.e. a resonance process. The energy required to cause the swapping between the states is dependent on the magnetic field strength.

$$\Delta E = \frac{\gamma h B_0}{2\pi} \tag{15}$$

Where h is Planck's constant and γ is the gyromagnetic ratio; a constant for a particular nucleus-type and directly proportional to the magnetic strength of the given nucleus. Equation 14 also demonstrates that nuclei of different elements will yield characteristic energies in a given magnetic field (see Figure 18).

Overall, the resonant frequency of the energy transition is dependent on the effective magnetic field at the nucleus and is modified by an electron shield which is governed by the chemical environment. Therefore, the resonant frequency can indicate information regarding the chemical environment in the nucleus. There are factors that give rise to resonant frequency shifts, or chemical shifts, including bond strain.

NMR was conducted in order to confirm the presence of MPA following the ligand exchange using a Bruker Avance III 500. A small amount of the sample (<1 mL) was pipetted into an NMR tube with a drop of deuterium (D_2O) in order to exchange the proton in an OH group and thus remove the dominating presence of OH groups. ^{13}C-NMR was selected in order to isolate the carbon from the carboxylic (COOH) group in MPA. The tube was loaded into the carousel and an overnight scan was scheduled with 4096 scans at 298 K.

3.4.3. Scanning Electron Microscopy and Energy-Dispersive X-ray Spectroscopy

Scanning electron microscopy (SEM) is a technique that probes the surface of a sample in order to produce an image at the micron scale. Electrons are used since the wavelength of light would make it too crude for imaging such small sizes; whereas an electron has a de Broglie wavelength small enough that it can penetrate crystal lattices. A beam of high energy electrons is scanned over the sample and depending on the accelerating voltage of the beam and the density of the QDs, the electrons will penetrate up to a few microns into the sample (see Figure 19 [69]). As a result of these interactions, secondary electrons, backscattered electrons and characteristic X-rays are generated,

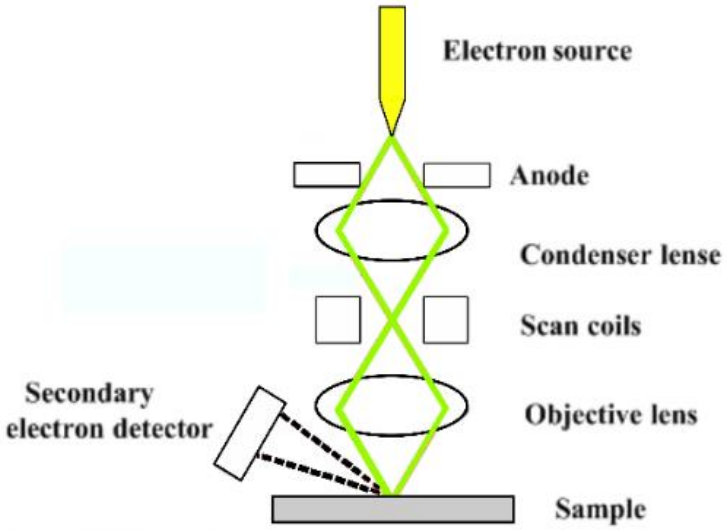

Figure 19: Diagram to show schematic of scanning electron microscopy. Electrons are generated through thermionic emission and accelerated by the positively charged anode. The condenser and objective lens converge the electron beam, with the condenser lens determining the size of the electron beam which dictates the resolution. The electron beam then scans over the sample and the secondary electron detector receives the secondary electrons which is processed before producing the image. Reproduced from: Nanakoudis [67].

some of which (secondary and backscattered) are used to display the image. Secondary electrons arise from the sample surface and are produced from the inelastic interaction

between the electron beam and the sample and backscattered electrons arise from the beam itself and are produced from the elastic interaction between beam and deeper parts of the sample. Secondary electrons are useful in imaging a sample's topography whereas backscattered electrons are primarily used in distinguishing the composition of a sample, since the number of backscattered electrons is proportional to the Z number in atoms. Energy dispersive x-ray analysis (EDX) can be performed in conjunction with SEM and uses the X-rays in order to distinguish the elemental composition of the sample by measuring their energy.

To observe the film morphology, an FEI Inspect S SEM was used with an Oxford Instruments EDX detector to collect information on the composition of the QDs. The QDs were drop cast onto aluminium stubs and then dried in a fume cupboard overnight before conducting any measurements. Once sufficiently dried, the QDs were loaded into the sample holder where a high energy beam of electrons was scanned over their surface.

3.4.4. Powder X-ray Diffraction

X-ray diffraction (XRD) is an analytical technique that exhibits the crystalline structure of crystals. X-rays are directed towards the crystal sample where the planes of the lattice can act as diffraction gratings. If the interaction between the x-rays and sample is coherent i.e. they are in phase and satisfy Bragg's Law, diffracted rays are produced which leave the crystal at an angle equal to the incident beam

$$n\lambda = 2d \sin\theta \tag{16}$$

where *n* is an integer, λ is the wavelength of the incident x-ray, *d* is the interplanar spacing of the crystal and θ is the angle of incidence (see Figure 20 [70]).

XRD was conducted using a Bruker D8 and was used to confirm the crystalline structure within the QDs and identify if they were reminiscent of chalcopyrite, wurtzite or zinc-blende structure. The QDs were centrifuged in order to precipitate them and left in the fume cupboard until dried before being deposited onto an XRD slide and into the sample holder.

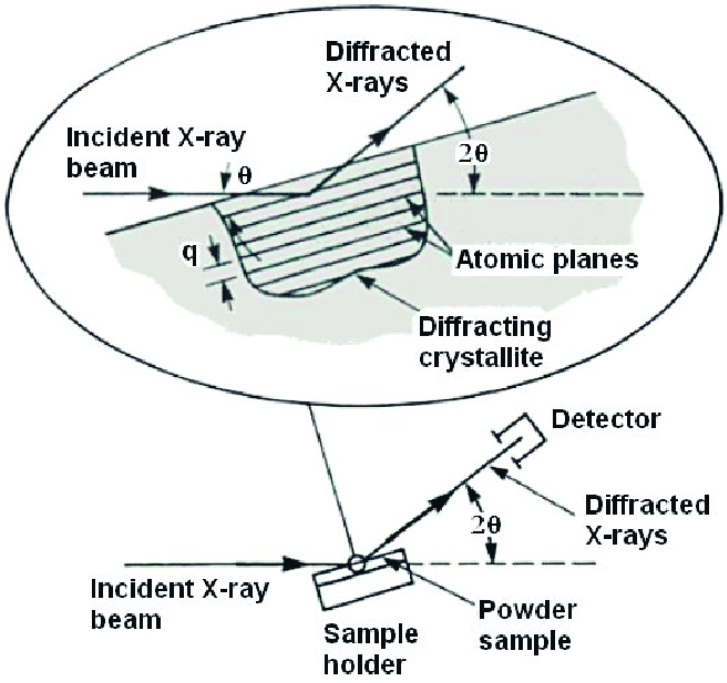

Figure 20: Diagram to show schematic of x-ray diffraction. Reproduced from Hudl [68].

Chapter 4. Results and discussion

4.1. Synthesis and Ligand Exchange of $CuInS_2$ Quantum Dots

QDs were synthesised following the modified procedure developed by Li et al. [71] with the precursors mixed in DDT and ODE and heated at various temperatures. The initial heating at T = 80°C was used to fully dissolve the powdered precursors in an excess of solvent. The ODE was used to increase solubility and with the DDT, assisted with control of the final composition and morphology of QDs. In these conditions, it was expected that metal-thiolate intermediates were allowed to homogeneously form and act as monomers for nucleation [22]. During heating, colour changes were observed and used as indicators of the stage of reaction. Following heating to T = 120°C, a clear yellow solution was formed. Heating to T = 210°C was used to facilitate nucleation of the nanoclusters. The colour of the solution changed from yellow to orange and then to red and to maroon-red.

At this stage, the temperature was decreased to T = 190°C to produce QDs with narrow size distribution. It is expected that the decrease in temperature reduces the possibility of nucleation events occurring at the same time as the growth stage, which would lead to an increased rate of Ostwald ripening. The process of Ostwald ripening is characterized by digestion of smaller clusters by larger nanocrystals, leading to an increase in size distribution and an increase in their average size [22]. Since the morphology of the QDs directly affects features such as bandgap, a large size distribution amongst QDs would produce broadening of the PL line and absorption spectrum.

Under UV illumination, the fluorescence of the core-shell samples was observed and was much brighter than the core-only QDs. From literature, it is widely accepted that coating the QDs with ZnS does improve fluorescence but the precise nature of this phenomenon remains debated. Passivating the QD core could reduce the number of defects on the surface of the CIS QD core, with ZnS and $CuInS_2$ having similar crystal lattice parameters [72]. Alternatively, since the bandgap of ZnS is much greater than in $CuInS_2$, the electrons and holes are confined more strongly in the core region and thus the probability of exciton recombination is greatly enhanced. The dominant mechanism could be identified by measuring the lifetime of the QDs, since band to band transitions have been shown to have longer lifetimes (of order 100 ns), whereas intragap defect states, commonly Cu_x-states (where x represents the oxidation state), have shorter lifetimes (of order 10 ns) [22]. Therefore, if the decay of the QDs with a shell is significantly quicker than the core-only samples, it would suggest the shell is removing

defect states and hence improving the fluorescence by that manner. If the ZnS shell does not affect the PL lifetime, it would suggest that the coating had been unsuccessful.

4.2. Model of Bandgap versus Radius

Bulk $CuInS_2$ has a bandgap energy E_g = 1.53 eV and the exciton Bohr radius of r_B = 4.1 nm [40]. For $CuInS_2$ QDs, the dependence of the energy gap of the QD is dependent on the radius and was calculated using Equation (11) and shown in Figure 21 (with the assumption that QDs are spherical, rather than tetrahedral). The inverse square relationship ($E_{g\ (QD)} \propto 1/R^2$) is observed with increasing radius of the QDs, the band gap decreases inversely squared.

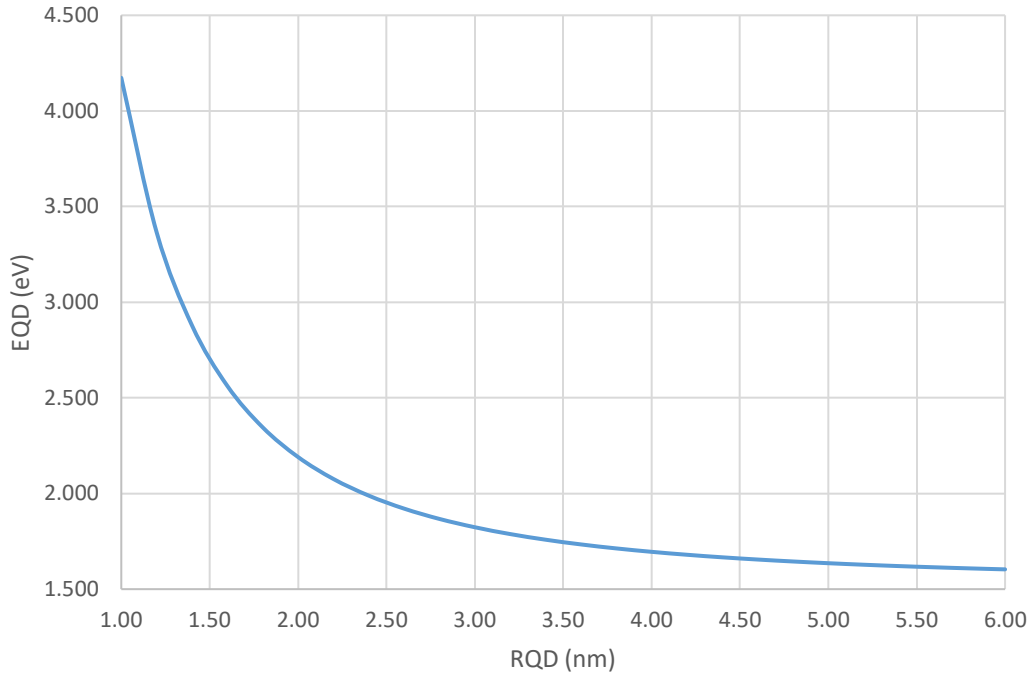

Figure 21: Dependence of band-gap energy, E_g, on the radius of the QD, estimated using the quantum confinement energy of a $CuInS_2$ QD (Equation 10) from [35].

The size of the QD, d_{QD}, defines the strength of spatial confinement in the QDs, hence the band gap of the QD. Using the particle in a box approximation, we find that a smaller QD has a larger barrier height, h, resulting in a larger band gap, $E_{g(QD)}$. There are other factors that contribute to the barrier height, such as capping ligands and/or shell (including thickness, composition and band structure) used to passivate the QD.

The capping ligands alter the quantum confinement of the quantum dot through localisation or delocalisation of the electrons and holes depending on their size and

structure. Localisation decreases the size of the box and thus increase the quantum confinement, whereas delocalisation decreases confinement [73]. Furthermore, from Equation (11), it is expected that an increase of dielectric constant (e.g. from substituting ligands) will lead to increased strength of confinement hence increasing the band gap value. For example, MPA ligands have been shown to induce surface trap states in CdSe QDs due to the thiol functional group, with the electron wavefunction delocalising to the QD surface and thus decreasing the confinement [74].

Zinc sulphide, with a bulk band gap of 3.6 eV, can be used as a protective shell for the $CuInS_2$ QDs. The degree to which the shell and ligands affected the confinement of the QD was compared using optical studies; as larger confinements would result in larger optical band gaps (blue-shifting in optical measurements). If the presence of the inorganic shell also reduces the amount of charge trapping defects on the surface of the QD core, then the quantum efficiency is expected to increase.

The diameter of the QD can be estimated from the PL peak position using the following equation:

$$d_{QD} = 68.952 - 0.2136\lambda_{PL} + 1.717 \times 10^{-4}{\lambda_{PL}}^2 \quad (17)$$

where d_{QD} is the diameter of the QD and λ_{PL} is the peak PL position in nm [39].

4.3. Optical Properties

4.3.1. Photoluminescence

The fluorescence of the quantum dots was measured to estimate the size of the QDs and subsequently find the value of the optical band gap of QDs. A range of excitation wavelengths were selected so the sample could be probed with photons at various energies. During each measurement, some of the photons were absorbed by the QDs and electrons were excited to higher states leaving behind holes in the valence band. Upon recombination of an electron and hole, a photon with energy equal to the relaxation transition is emitted. The electron could recombine with the hole in the valence band or alternatively, a hole pre-existing in an intragap defect state between the bands. The greater the PL intensity measured, the greater the number of photons detected at that wavelength. Equation (17) was used to estimate the diameter of the QDs and this was

then used in Equation (11) to calculate the optical band gap for QDs with that diameter.

The photoluminescence spectra of $CuInS_2$ quantum dots have Gaussian shape. Figure 22 displays the PL spectra of DDT-capped QDs at excitation wavelengths between 400 nm and 590 nm. Generally, the PL spectra revealed the same positions with some red-shift in the PL peak with smaller excitation energy. Figure 23 shows the PL peak at λ_{Ex} = 400 nm with a Gaussian fit added.

Figures 24 – 26 display summary figures of the PL results with the Gaussian fit, as shown in Figure 23, used to find the standard error for the peak PL, intensity and FWHM results. Figure 24 shows the peak position for every PL peak at the corresponding excitation wavelength and Figure 25 shows the full width at half maxima (FWHM) value for every PL peak at the corresponding excitation wavelength. Figure 26 shows the PL intensity for each PL peak per excitation energy.

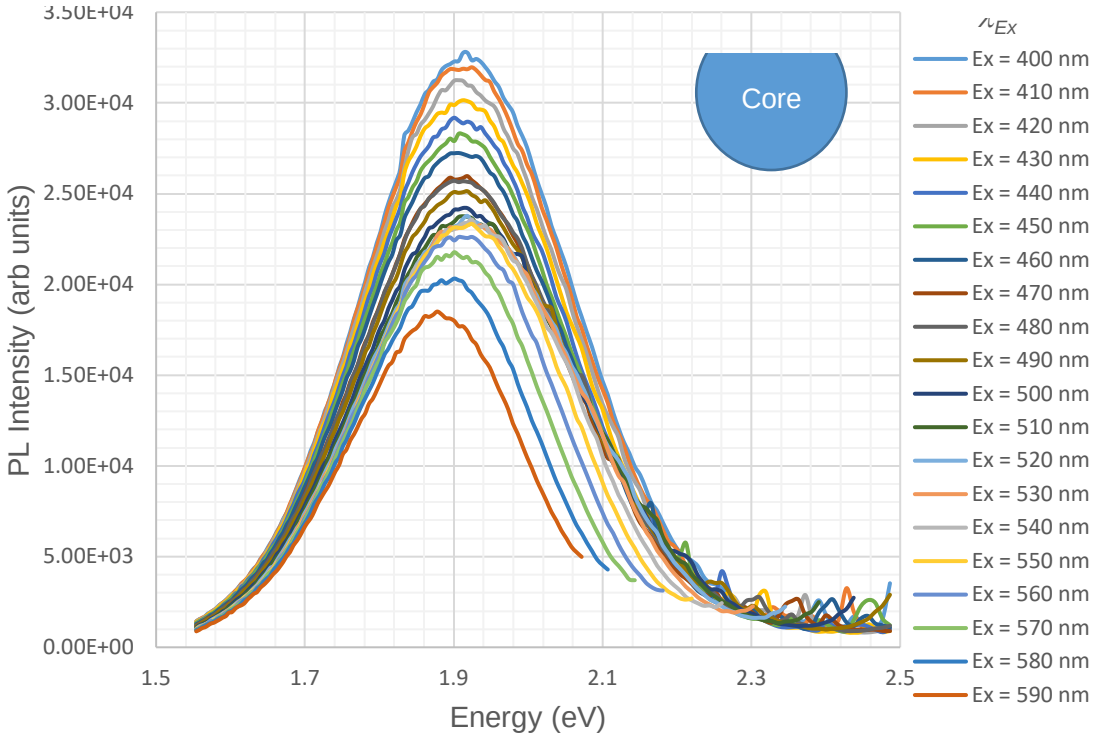

Figure 22: Photoluminescence spectra of DDT-capped core-only $CuInS_2$ QDs at different excitation wavelengths in terms of energy (eV). Excitation was provided by FLS 980 Spectrometer, with a step size of 1.00 nm, a dwell time of 1.00 s and slit widths of 3.00 nm and 0.15 nm, for the excitation and emission, respectively. Excitation wavelength key displayed on right.

For 400 nm < λ_{ex} < 550nm, the PL peak was centred at (1.9200 ± 0.0004) eV as shown

in Figure 22. The lowest excitation wavelength, λ_{Ex} = 400 nm, had a peak at (1.9195 ± 0.0004) eV and the greatest excitation wavelength, λ_{Ex} = 590 nm, had a peak at (1.8831 ± 0.0004) eV. The range between the PL peak positions was 0.04 eV. With comparison to other reported PL peaks of CIS QDs from literature, the peak positions were in agreement, but the size, morphology, surface chemistry and exact composition of CIS QDs can have significant shifts on the PL maximum [75]. The peaks were broad, with the peak starting at 2.3 eV and the red side extending towards 1.6 eV. The broadness was likely due to a large size distribution within the sample, coupled with this PL likely being a defect-related phenomenon with energetic positions that are largely dependent on local properties of the crystal structure. The range of energetic positions is therefore vastly increased with a larger sample of QDs. Furthermore, it would be feasible that the PL spectrum comprised of multiple peaks since there were likely to be multiple emission processes occurring within the QD and the spectrum is likely thermally broadened.

For the longest excitation wavelength peaks, the peak PL position red-shifted slightly. At λ_{Ex} = 560 nm, there was a red-shift in the peak position of approximately 0.01 eV from the previous PL peaks, with a subsequent red-shift of approximately at a rate of 10 meV per 10 nm up until λ_{Ex} = 590 nm, where the peak position was at the smallest energy of (1.8831 ± 0.0004) eV. The red-shift may have been caused by the recombination of the photo-generated electron with a hole closer to the conduction band, most likely due to a defect state.

Using Equation (17), the diameter of the PL peaks at 1.92 eV corresponded to a QD diameter of 2.7 nm. The PL peak at 1.88 eV corresponded to a QD diameter of 2.8 nm. Using Equation (11), the QDs with a diameter of 2.7 nm and 2.8 nm had optical band gaps of 2.98 eV and 2.88 eV, respectively.

The intensity of the PL peaks arose from the number of photons emitted from the QDs upon exciton recombination. Therefore, the greater intensity, the greater the frequency of radiative exciton recombination events. In general, the longer the excitation wavelength, the less the PL intensity and thus the less likely a radiative recombination event. Longer excitation wavelengths possess smaller energies, thus a photon is less likely to be absorbed.

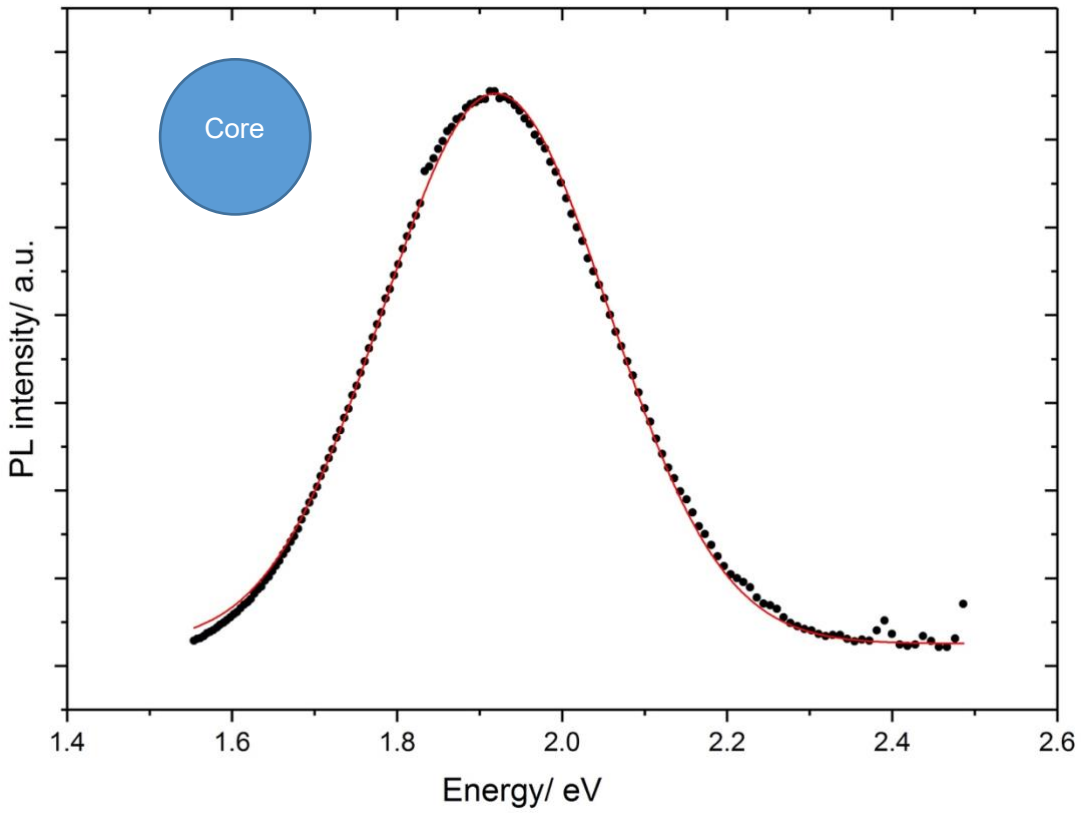

Figure 23: Plot of PL peak (black) for DDT-capped core-only $CuInS_2$ solution with Gaussian fit at Ex = 400 nm (red). Plotted using OriginLab.

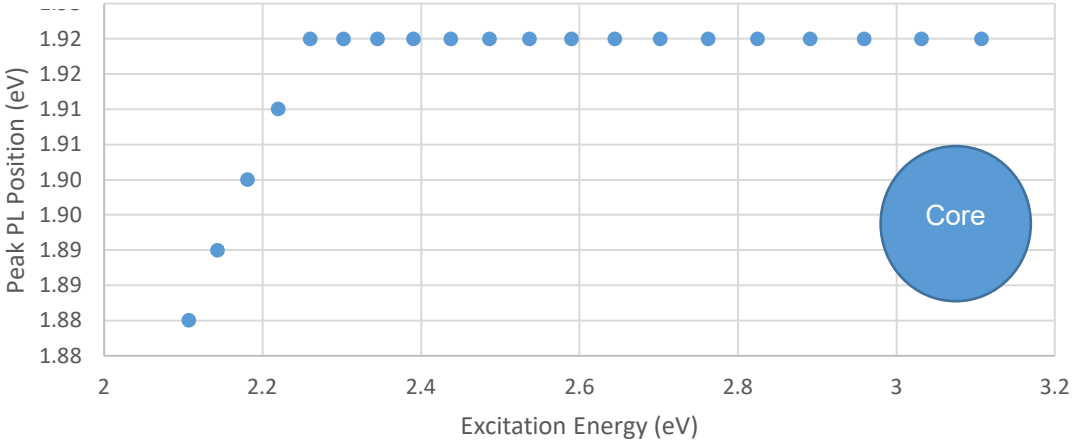

Figure 24: Dependence of peak PL position on photoluminescence emission energy for the DDT-capped core only $CuInS_2$ QDs. Excitation was provided by FLS 980 Spectrometer, with a step size of 1.00 nm, a dwell time of 1.00 s and slit widths of 3.00 nm and 0.15 nm, for the excitation and emission, respectively. Error bars calculated from Gaussian fitting with OriginLab, with a standard error of ± 0.0004 eV.

The PL peak energies were plotted against the corresponding excitation energies in Figure 24. Generally, the peak energy was the same, with most of the results at approximately (1.9200 ± 0.0004) eV. There was redshift as the excitation energy decreased, possibly indicating the presence of defect states in between the valance and conduction band which enabled lower energy transitions via emission of lower energy photons.

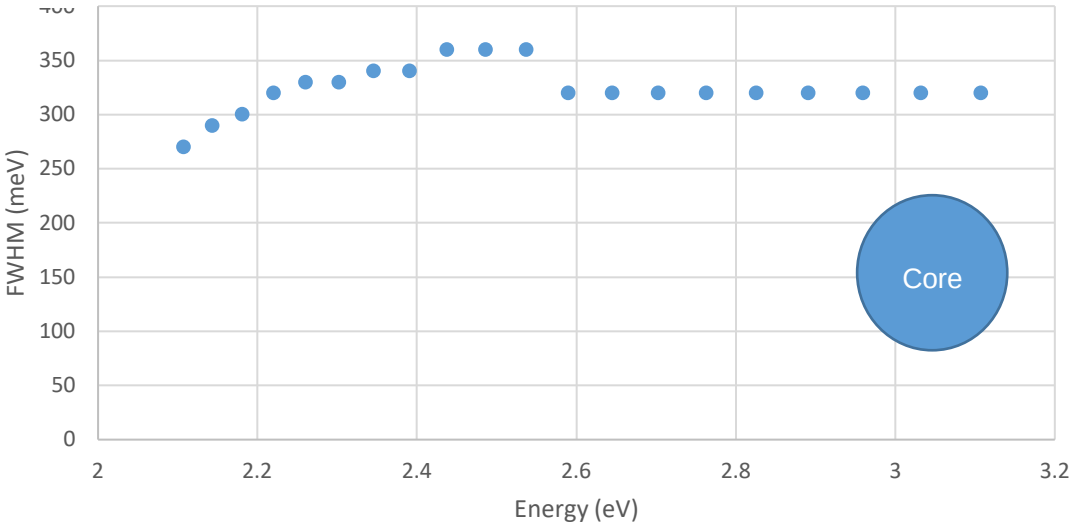

Figure 25: Dependence of full width at half maxima on photoluminescence emission energy for the core only $CuInS_2$ QDs. Excitation was provided by FLS 980 Spectrometer, with a step size of 1.00 nm, a dwell time of 1.00 s and slit widths of 3.00 nm and 0.15 nm, for the excitation and emission, respectively. Error bars were estimated from Gaussian fitting with OriginLab, with a standard error of 1 meV.

The FWHM values shown in Figure 25 increase from 260 and 360 meV at E_{ex} = 2.1 eV to E_{ex} = 2.5 eV; the FWHM decreased to approximately 320 meV and remained unchanged up to E_{ex} = 3.1 eV. CIS QDs characteristically have FWHM values ranging between 200 – 400 meV [76], likely due to large size and compositional distributions. Therefore, these data were in good agreement with the literature.

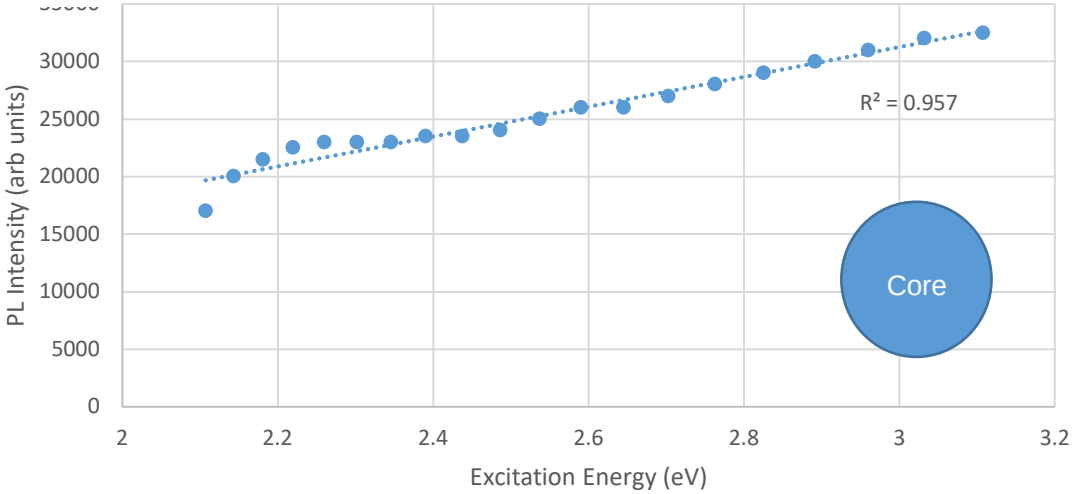

Figure 26: Dependence of photoluminescence intensity on photoluminescence emission energy for the core only DDT-capped $CuInS_2$ QDs. Excitation was provided by FLS 980 Spectrometer, with a step size of 1.00 nm, a dwell time of 1.00 s and slit widths of 3.00 nm and 0.15 nm, for the excitation and emission, respectively. Error bars calculated from Gaussian fitting with OriginLab, with standard error or ± 62 (arb units).

The PL intensity per excitation energy was plotted in Figure 26. A linear line of best fit was drawn on the data points to show that as the excitation energy increased, the PL intensity increased linearly, with the R_2 value, 0.957, indicating a good fit. For photoluminescence energy greater than 2.4 eV, the fit was even more accurate. This demonstrates that as the excitation energy decreased, the PL intensity decreased proportionally as well. At lower excitation energies between 2.4 and 2.1 eV, the trend did not fit as well, with the PL intensity briefly levelling out before decreasing non-linearly at ~ 2.2 eV.

The photoluminescence spectra of core-shell DDT-capped CIS/ZnS QDs are shown in Figure 27. The PL peak is centred at 1.98 eV and the same for wavelengths 400 nm < λ_{ex} < 530 nm (Figure 31). At λ_{ex} = 530nm to λ_{ex} = 550 nm, blue-shift of the PL emission by ~ 0.04 to 0.07 eV was observed from the rest of the PL peaks, respectively. The dependence of intensity on excitation energy is shown on Figure 28, the Gaussian fitted PL using OriginLab is shown on Figure 29, the peak PL position plotted against excitation energy is shown on Figure 30 and finally the FWHM values plotted against excitation energy were plotted and shown in Figure 31, respectively. The error bars were calculated using the Gaussian fitting feature on OriginLab.

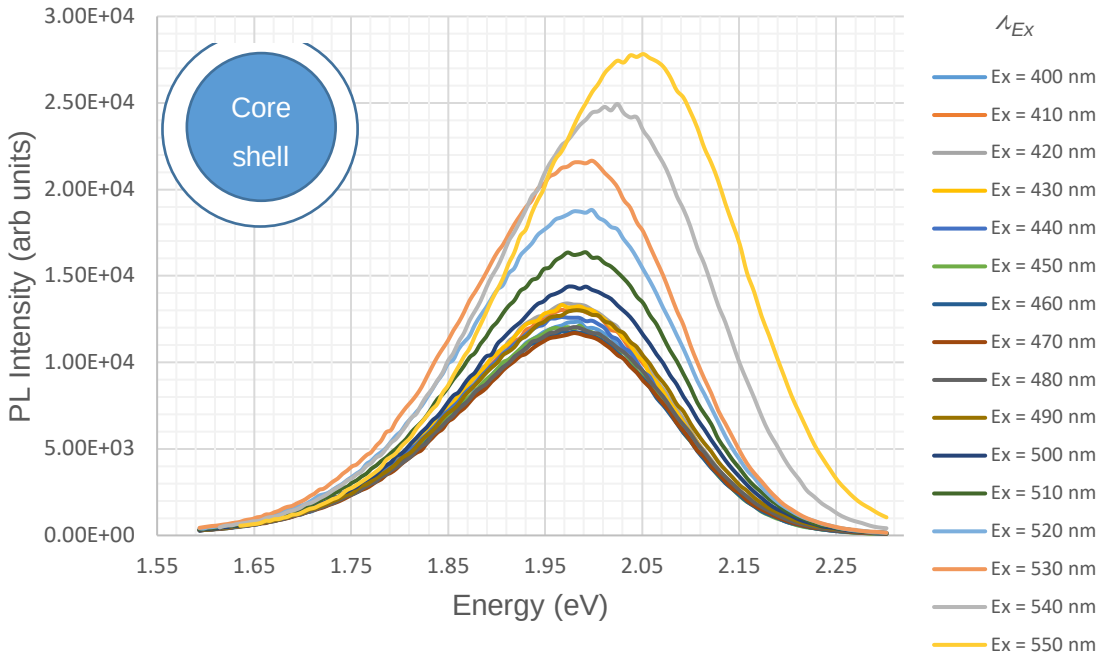

Figure 27: Photoluminescence spectra of core-shell DDT-capped $CuInS_2$/ZnS QDs in terms of emission energy. Excitation was provided by FLS 980 Spectrometer, with a step size of 1.00 nm, a dwell time of 1.00 s and slit widths of 3.00 nm and 0.15 nm, for the excitation and emission, respectively.

For almost all λ_{ex} used, the PL emission peak was observed at approximately (1.980 ± 0.001) eV, which was blue-shifted from the core-only samples by ~ 0.06 eV. The blue shift from the core sample can be attributed to either Zn-alloying leading to an increase in the band gap of the material since the band gap of bulk ZnS is greater than that of $CuInS_2$, or to cation exchange at the surface of the NC yielding a gradient alloy, where Zn^{2+} ions replace Cu^{+} and In^{3+} ions resulting in a smaller CIS core, thus increasing the band gap through quantum confinement effects [77]. However, at λ_{Ex} = 530 nm the peak position was blue-shifted by ~10 meV from the modal 1.98 eV and subsequent blue-shifting was observed at a rate of ~ 10 meV for every 10 nm until λ_{Ex} = 550. The changes in PL peak position indicated a range of possible recombination routes within the QD. In a study by Yan et al. [78], a similar observation was noted that an increasing excitation wavelength resulted in a blue-shift of the PL peak. This lead to the conclusion that the PL of $CuInS_2$/ZnS contained multiple emission routes, owing to different structures of the QD: $CuInS_2$, $Cu_xZn_{1-x}InS_2$, ZnS:Cu (where Zn diffused into the core and replaced Cu, thus resulting in a Cu doped ZnS interface) and ZnS. At lower excitation energies, the ZnS:Cu and ZnS cannot be excited. However, the PL can be blue-shifted at lower excitation energies where Zn diffused into the $CuInS_2$ core ($Cu_xZn_{1-x}InS_2$) since this interface has a smaller band gap than the outer shell (ZnS:Cu and ZnS).

Using Equation (17), we estimate that the PL peaks at 1.98 eV, corresponded to a QD diameter of 2.53 nm and using Equation (11) this diameter corresponded to an optical band gap of 3.18 eV. The PL peaks at 1.99 eV, 2.02 eV and 2.05 eV corresponded to QD diameters of 2.52 nm, 2.53 nm and 2.55 nm, respectively and optical band gaps of 3.20 eV, 3.18 eV and 3.16 eV, respectively using Equation (11). The diameters estimated using Equation (17) suggested that, with the exception of the PL peaks at 1.98 eV, the larger photoluminescence emission energies corresponded to larger diameters of QDs. This is contradictory to quantum confinement, as a larger photoluminescence emission energy would suggest a larger optical band gap and thus a smaller QD with a larger quantum confinement.

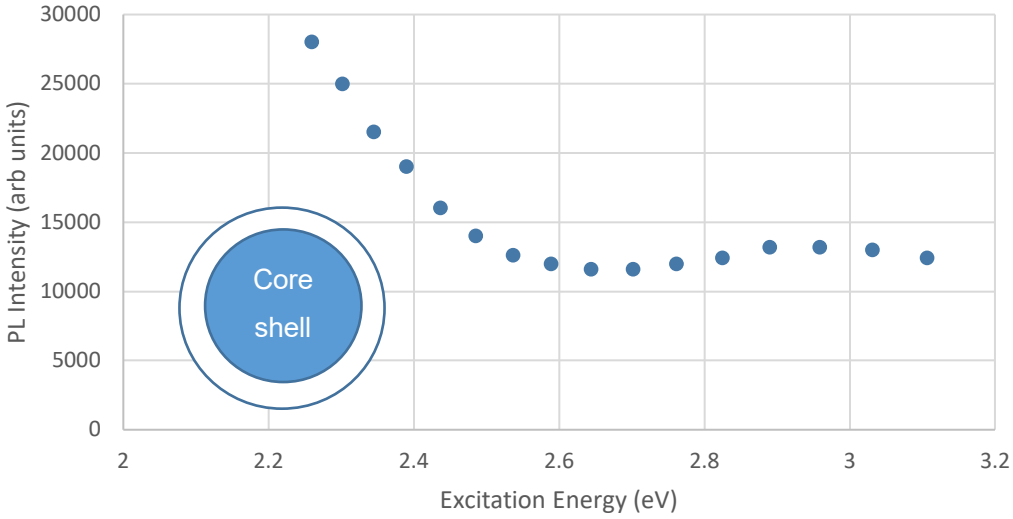

Figure 29: Dependence of PL peak intensity on photoluminescence emission energy for core shell $CuInS_2/ZnS$ QDs. Excitation was provided by FLS 980 Spectrometer, with a step size of 1.00 nm, a dwell time of 1.00 s and slit widths of 3.00 nm and 0.15 nm, for the excitation and emission, respectively. Error bars calculated from Gaussian fitting with OriginLab, with standard error of ± 48 (arb units)

For 2.48 eV < λ_{ex} < 3.11 eV, the PL intensity remained steady as shown in Figure 29. Thus, the number of radiative exciton recombination emitting photons remained relatively constant. However, for λ_{Ex} = 500 (2.48 eV), the PL intensity increased for subsequent larger excitation wavelengths up to λ_{Ex} = 550 nm (2.26 eV), thus indicating an increased frequency of exciton recombination events. This may have been analogous to the report by Yan et al. [78] whereby the lower excitation wavelength only provided photons capable of exciting the $Cu_xZn_{1-x}InS_2$ and $CuInS_2$ core which have a lower band

gap than the ZnS:Cu and ZnS structures. In this case, the increased intensity at lower wavelengths may have reflected an increased number of total exciton recombination events, since only the $Cu_xZn_{1-x}InS_2$ and the $CuInS_2$ core were able to be excited by the lower energy photons and the ZnS:Cu and ZnS shell, with a larger band gap, were not. Therefore, there was a greater probability of exciton recombination.

The peaks produced from the core-shell samples were less broad than the core-only QDs, as shown by the FWHM values in Figure 32. The fitting of the core-shell QDs was much less precise than the core-only QDs, as such the error bars were all larger in the core-shell graphs.

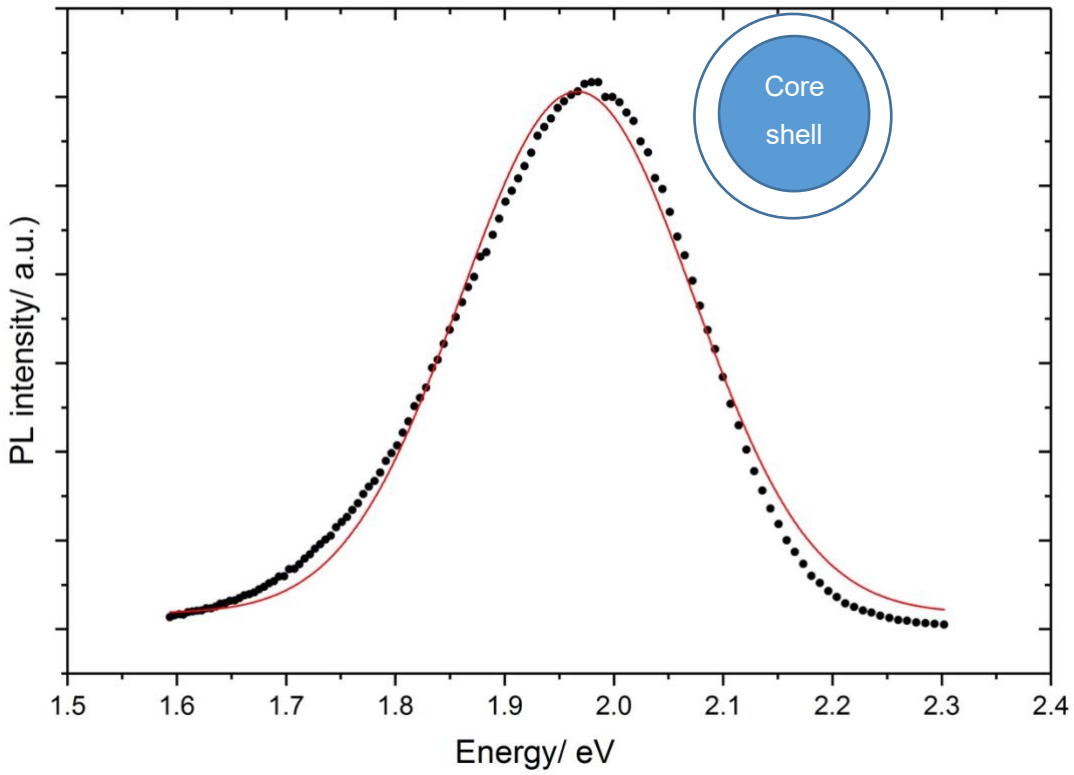

Figure 30: PL plot of core-shell DDT-capped $CuInS_2$/ZnS QDs (black) at Ex = 400 nm with Gaussian fit (red). Excitation was provided by FLS 980 Spectrometer, with a step size of 1.00 nm, a dwell time of 1.00 s and slit widths of 3.00 nm and 0.15 nm, for the excitation and emission, respectively. Plot created using OriginLab.

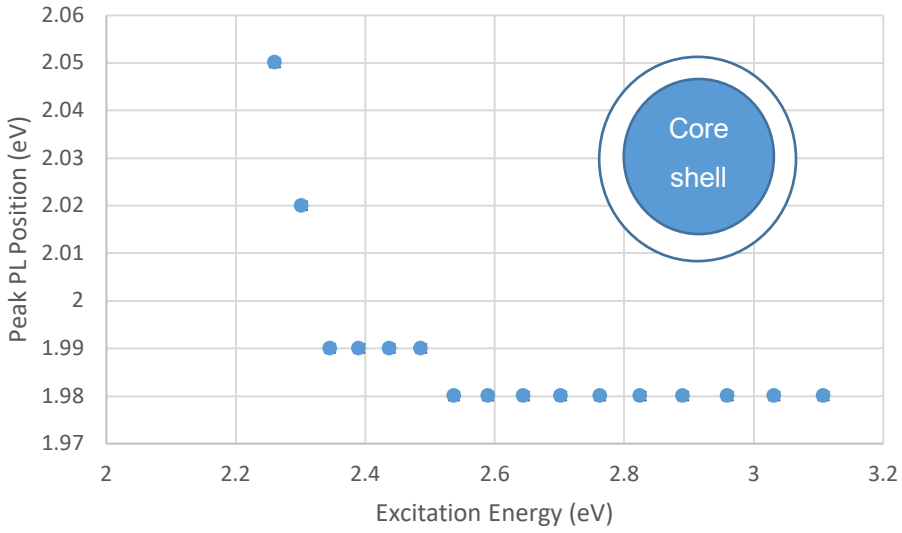

Figure 31: Dependence of PL peak position on photoluminescence emission energy for the core shell $CuInS_2/ZnS$ QDs. Excitation was provided by FLS 980 Spectrometer, with a step size of 1.00 nm, a dwell time of 1.00 s and slit widths of 3.00 nm and 0.15 nm, for the excitation and emission, respectively. Error bars estimated from Gaussian fitting with OriginLab with a standard error of ± 0.001 eV.

For E_{ex} > 2.3 eV, The peak position was stable at (1.980 ± 0.001) eV and (1.990 ± 0.001) eV as shown in Figure 31. However, some blue-shift of the PL does occur with lower excitation energy which seems counter intuitive, but has been reported in literature as the result of multiple emission bands within the $CuInS_2/ZnS$ QDs. The work from Yan et al. [78] displayed contradictions to the previously believed mechanism of cation diffusion at the core-shell interface resulting in an alloyed CuZnInS layer between the CIS core and ZnS shell. Instead, their optical measurements indicated that Zn ions diffused deeper into the CIS core and lead to the complete conversion into $Cu_xZn_{1-x}InS_2$. Furthermore, they suggested that Cu ions also diffused into the ZnS shell which lead to the formation of a ZnS:Cu shell. The ZnS:Cu shell has a large bandgap and is thus not excited by low energy photons, but absorbs via interband transition; with the excited electron moving between energy levels of the copper ion to emit orange (low energy) light. The $Cu_xZn_{1-x}InS_2$ core, however, has a smaller band gap than the shell and is able to be excited by low energy photons and emits green (higher energy) light. Therefore, it was postulated that as the excitation wavelength increased, the superimposed (due to two emission bands) asymmetrical PL peak is gradually blue shifted.

The sizes estimated from PL peak position may not be reliable as indirect band

transitions are also possible. Other transitions within the QD can cause PL emission, such as radiative recombination due to a transition from a quantised conduction-band state to a localised intra-gap defect state. An alternative method of calculating the band gaps is through absorption spectra and subsequent Tauc plots, as shown in Chapter 4.3.2.

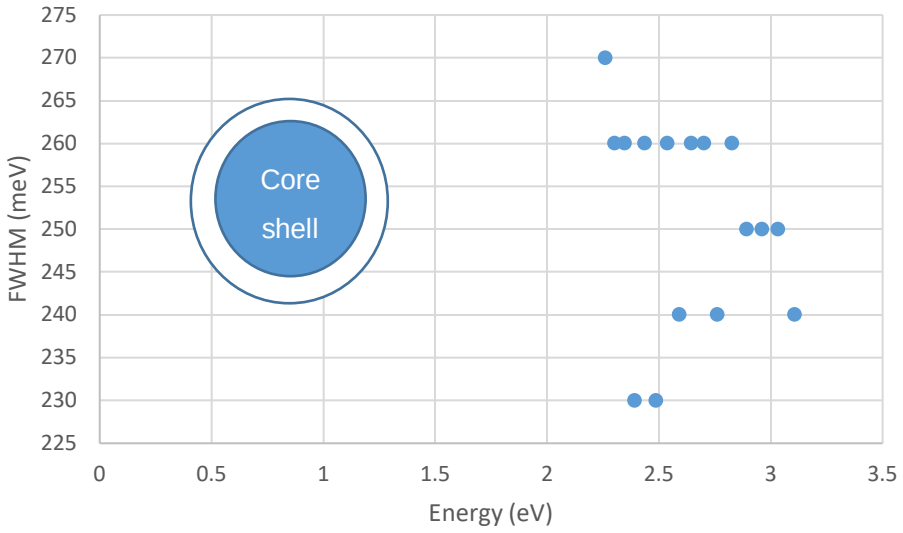

Figure 32: Dependence of full width at half maxima on photoluminescence emission energy for the core shell $CuInS_2/ZnS$ QDs. Excitation was provided by FLS 980 Spectrometer, with a step size of 1.00 nm, a dwell time of 1.00 s and slit widths of 3.00 nm and 0.15 nm, for the excitation and emission, respectively. Error bars estimated from Gaussian fitting with OriginLab with the standard error of ± 3 meV.

The FWHM values for the core-shell ranged between 230 and 270 meV as shown in Figure 32. This showed a decrease from the core samples, possibly indicating a reduction in the number of defect states that could be responsible for emissions other than band to band transitions. However, the FWHM values still fall within the 200 – 400 meV reported for CIS QDs [76].

The core-shell samples were drop-cast onto a glass slide and the photoluminescence spectra was also measured. Figure 33 shows the PL spectra of deposited core-shell DDT capped QDs. Unlike the colloidal core-shell QDs, the deposited QDs did not appear to show an increase in PL intensity of blue-shift for longer excitation wavelengths. The peak positions remained similar (1.955 ± 0.005 eV) for all excitation wavelengths with extended tails towards longer wavelengths. Despite the PL intensity remaining similar for

the colloidal and deposited QDs, the latter had significantly more noise in the spectra.

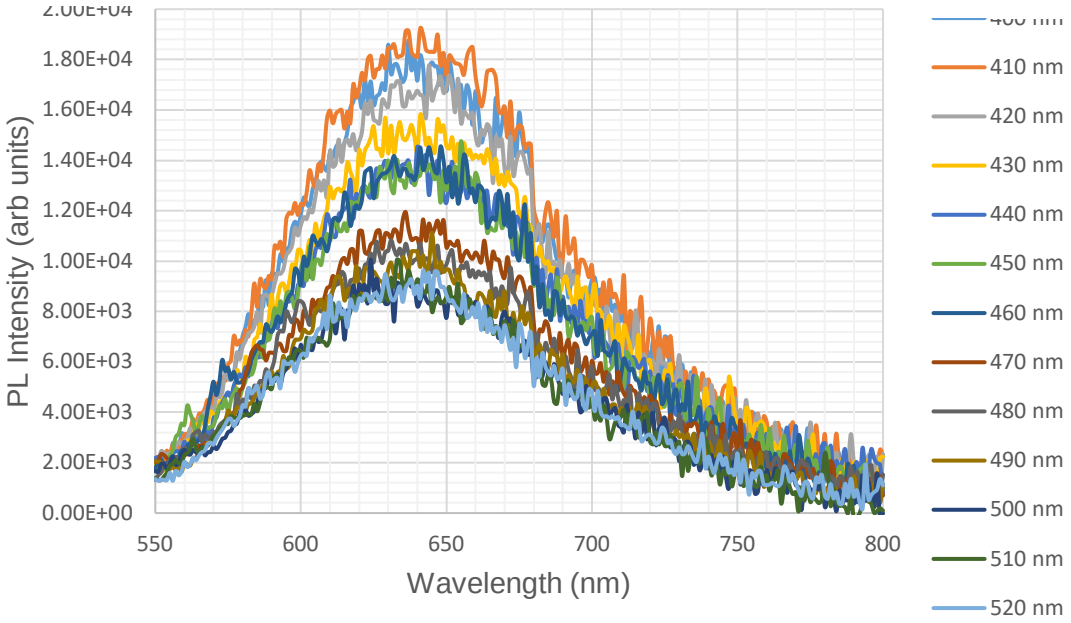

Figure 33: Photoluminescence spectra of core shell $CuInS_2$/ZnS QDs deposited onto a glass slide at different excitation wavelengths. Excitation was provided by FLS 980 Spectrometer, with a step size of 1.00 nm, a dwell time of 1.00 s and slit widths of 3.00 nm for the excitation and emission, respectively.

For all λ_{ex}, the PL peak was stable at 1.95 eV and 1.96 eV, which was red-shifted from the colloidal core-shell samples by ~ 0.02 to 0.04 eV. The red-shift could have been caused by fluorescence/Förster resonance energy transfer (FRET) due to the deposited QDs being situated closer together than when in colloidal solution. FRET involves a non-radiative energy transfer of an excited QD (following absorption of a photon) to another QD in the ground state via dipole-dipole interactions. In this process, a small QD emitting a high energy photon could be absorbed by a larger QD which consequently emits lower energy photons, thus the resultant PL spectrum reflects mostly the lower energy photons from the larger QDs [79]. The work from Yagenetfere et al. [75] similarly reported a red-shift of powdered QDs from the colloidal QDs and attributed the observation to the fact that the surfactant molecules, which aid in confinement of electrons and holes within the QDs, were substantially removed which allowed the QDs to directly contact adjacent ones. Thus the red-shift of the PL emission was assigned to the leakage of electrons and holes because of a partial breakdown of the quantum confinement effect. As such, the PL behaviour of the deposited QDs leans towards the bulk behaviour.

In addition, the deposited sample did not show a blue-shift at λ_{Ex} = 500 nm nor for

subsequent, longer wavelength excitations, unlike the colloidal counterpart. Moreover, the intensity decreased with longer excitation wavelengths, with the exception of λ_{Ex} = 410 nm which showed the highest intensity of all excitation wavelengths with a slight increase in intensity over λ_{Ex} = 400 nm.

Using Equation (17), the PL peaks at 1.96 eV corresponded to a QD diameter of 2.53 nm and Equation (11) estimated the optical band gap was 3.18 eV. However, the noise in the spectrum meant that the peak position was unreliable due to a high uncertainty in the measurement.

Following the ligand exchange with MPA of the core-shell sample, the PL spectrum redshifted significantly from the colloidal core-shell spectra (as shown in Figure 34). The peak PL position increased to approximately 1.92 eV, thus showing an increase by 0.06 eV. In fact, the peak position was more similar to the core-only QDs. However, the shape of the PL peak was significantly different compared to the previous PL measurements as the Gaussian form was disrupted at approximately 1.82 eV where there was a sharp increase (possibly due to a lamp change). Nevertheless, the MPA ligands were expected to decrease the distance between neighbouring QDs (though in solution this would be dependent on concentration), therefore FRET may have occurred more frequently which resulted in the red-shift. During FRET, the emission of high energy photons from QDs can be reabsorbed by larger QDs which in turn emit shorter energy photons upon exciton recombination. In a report by Xu et al. [27], it was shown that the MPA ligands red-shifted the photoluminescence due to the MPA ligands reducing the inter-dot separation which augmented the electron coupling and lead to decreased quantum confinement.

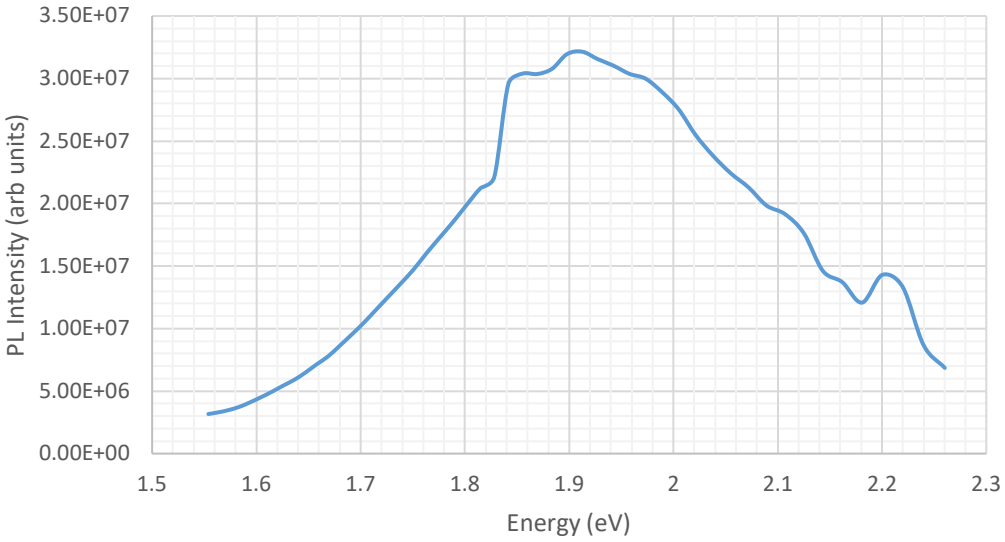

Figure 34: PL spectrum of core-shell MPA-capped QDs. Excitation was provided by FLS 980 spectrometer, with excitation energy of 450 nm, dwell time 1.00 s, step size 5.00 nm. Slit widths were 4.00 nm and 1.00 nm for the excitation and emission, respectively

4.3.2. Absorbance

The absorption of the QDs was measured in order to determine the wavelengths that were absorbed by the QD leading to exciton generation. The absorption was used to estimate the bandgap of the QDs. For a photon to be absorbed by the QD, its energy must be greater than the bandgap of the QD. Upon photon absorption, an electron is excited into the conduction band from the valence band.

The absorption spectra of $CuInS_2$ QDs typically either show a small or no feature and often do not reveal a distinctive excitonic peak, even with small size distributions [76]. The measured absorption profiles for the DDT-capped core and core-shell QDs (see Figure 35 and 36) did not display any indication of an excitonic peak. However, in the absorption profile for the MPA-capped QDs (see Figure 37), a possible excitonic peak from the QDs was observed between 570 – 590 nm.

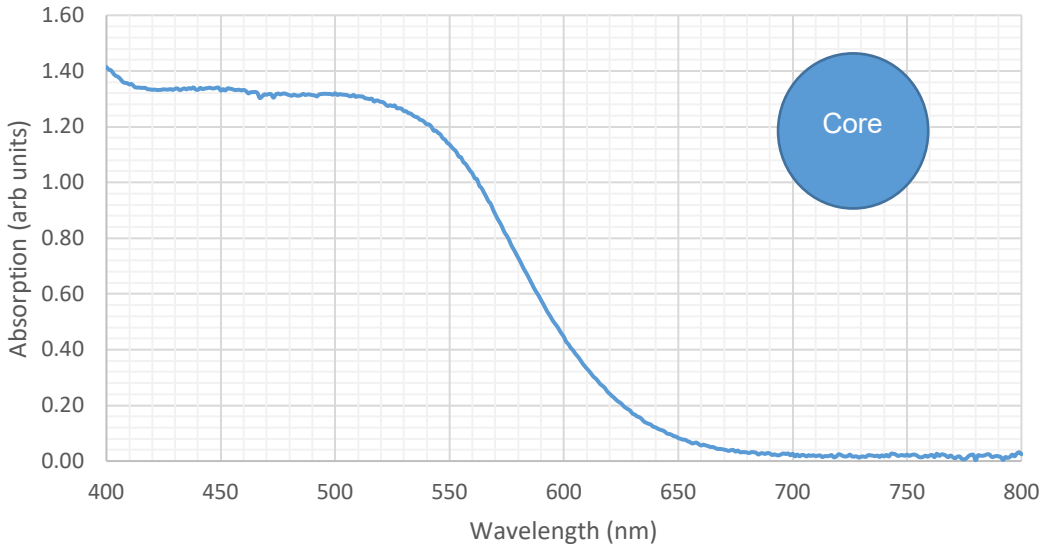

Figure 35: Absorption spectrum for the core only $CuInS_2$ QDs. Excitation wavelength provided by FLS 980 spectrometer. Measurement conducted using integrated sphere with a step size of 1.00 nm, a dwell time of 1.00 s and slit widths of 3.00 nm and 0.15 nm, for the excitation and emission, respectively. Hexane was used as the reference sample.

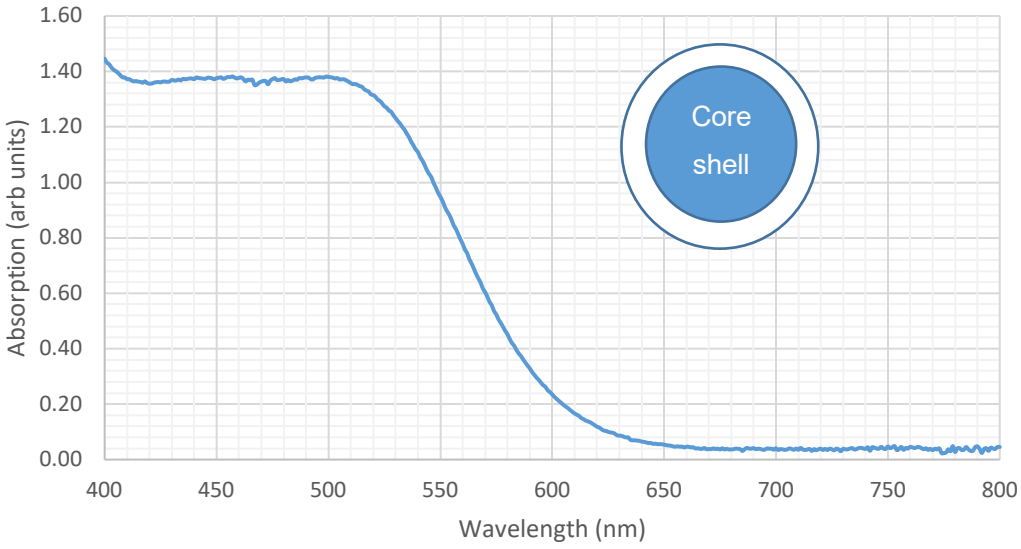

Figure 36: Absorption spectrum for the core shell $CuInS_2/ZnS$ QDs. Excitation wavelength provided by FLS 980 spectrometer. Measurement conducted using integrated sphere with a step size of 1.00 nm, a dwell time of 1.00 s and slit widths of 3.00 nm and 0.15 nm, for the excitation and emission. Hexane was used as the reference sample.

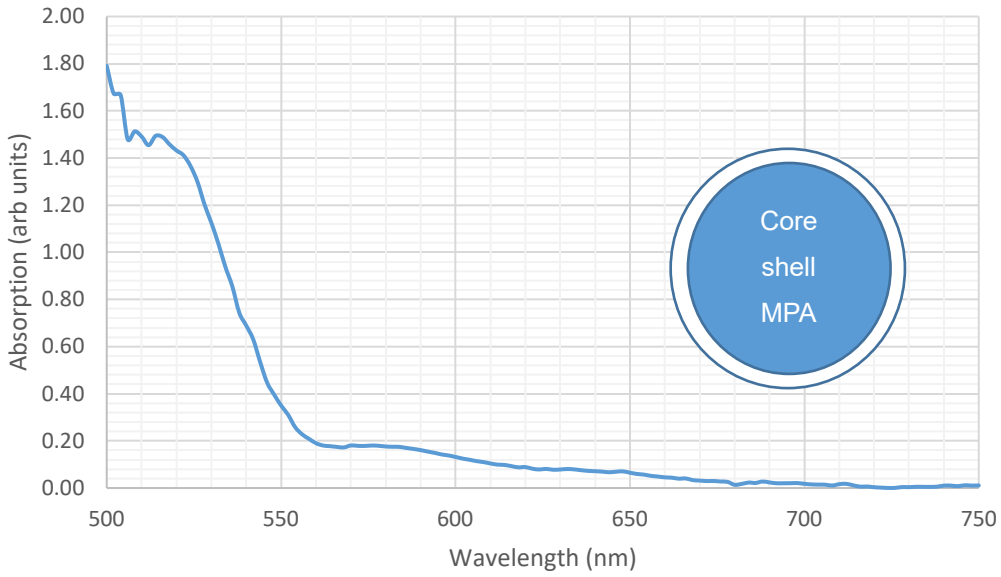

Figure 37: Absorption spectrum for the core shell MPA-capped $CuInS_2/ZnS$ QDs. Excitation wavelength set at 520 nm using the FLS 980 spectrometer. Measurement conducted using integrated sphere with a step size of 2.00 nm, a dwell time of 1.00 s and slit widths of 4.00 nm and 1.00 nm, for the excitation and emission. Deionised water was used as the reference sample.

The absorption spectra for the DDT-capped core and core-shell samples do not reveal distinct exciton peaks, possibly due to inhomogeneity in the sample; specifically, broad size and/or composition distributions. Alternatively, it has been suggested that the lack of a peak could be a characteristic feature of CIS nanocrystals, possibly owing to a strong exciton-phonon coupling [40, 76]. In our samples, we envisage that a very broad morphological distribution is present within the samples and leads to the absence of a distinctive exitonic peak. We note that for the sample with a ligand replacement there is a slight shoulder in the MPA-capped QDs at approximately 580 nm.

A blue shift of ~ 15 nm (by measuring the change in wavelength from the difference in intensity at *A* = 1.00) is also observed in the absorbance spectra from the core to the core/shell. A much more significant blue shift was observed from the DDT-core-shell to the MPA-core-shell QDs of approximately 40 nm. In the literature, the reported blue shift in absorbance is comparable to that of the photoluminescence, but in other cases a weaker change is observed. In PL, the emission is likely dominated by carrier recombination on defect states within the core of the nanocrystal [52]. However, since absorption is not defect-dominated, the blue-shift is not expected to change as much as in PL since the position of the VB does not vary as much with altering QD diameter; it is predominantly the CB that changes energy with size (see Equation 11, where $m_e^* = 0.13\ m_0$ and $m_h^* = 1.16\ m_0$). For these results, the blue-shift from the core-shell QDs with DDT ligands was comparable to the blueshift in the PL spectra. In order to calculate the blue-shift in the absorption spectra, the 2nd derivative of the absorption spectrums could be found and then the peak positions of the core-only and core-shell absorption profile could be found separately and the change between them calculated. However, 2nd derivative of these absorption profiles was not possible since the profiles were relatively featureless. Therefore, the wavelengths at various absorbance values was used to calculate the blue-shift. At absorbance *A* = 0.8, the corresponding absorbed wavelength for the core only samples was 575 nm ± 5 nm, which was blue-shifted by 15 nm to 560 nm ± 5 nm for the core shell sample. At absorbance *A* = 0.4, the absorption wavelength was 600 nm ± 5 nm for the core sample and 585 nm ± 5 nm for the core shell sample, again displaying a blue shift of 15 nm. Finally, at *A* = 0.20, the absorption wavelength was 625 nm ± 5 nm for the core sample and 600 nm ± 5 nm for the core shell sample, showing an increased blue shift at the tail section of the spectra by 25 nm. The blue-shift observed in samples with MPA ligands suggested that the optical band gap increased, in turn indicating that the size of the QDs decreased. This may have been caused by the Zn from the shell etching further into the QD core. Alternatively, the MPA ligands could have allowed for the QDs to become less separated and increase the number per unit

area, thus shorter wavelengths (higher energy photons) were less likely to pass through the colloidal solution without interaction. However, since the QDs were in solution, this was less likely than the zinc etching.

Using the absorption spectra, Tauc plots (see Figure 38 - 43) can be plotted to estimate the band gap of the QDs. To generate a Tauc plot, the product of the absorption and corresponding excitation photon energies ($\alpha h\nu$) are squared ($\alpha^2 h^2 \nu^2$) and plotted against the excitation energies ($h\nu$). In the region where $h\nu > E_g$, i.e. where the energy of a photon is sufficient to produce an exciton, a linear line was fitted and the x-intercept indicated the energy of the bandgap. At low energies, the absorption is zero as the energy of the photon is less than the bandgap. As the photon energy increases to the bandgap, there is an exponential increase called the Urbach tail [80]. This is the result of defects near the band edge which allow for absorption into lower energy states compared to the conduction band. At the proposed Tauc band gap, the Tauc plots display a region of linearity in the squared-exponent plots. After the linear region, the absorption processes saturate and can be ignored [80]. Each Tauc plot was complemented with a separate plot of the linear region, with the line equation generated by the linear line of best fit used to determine the x-axis intercept.

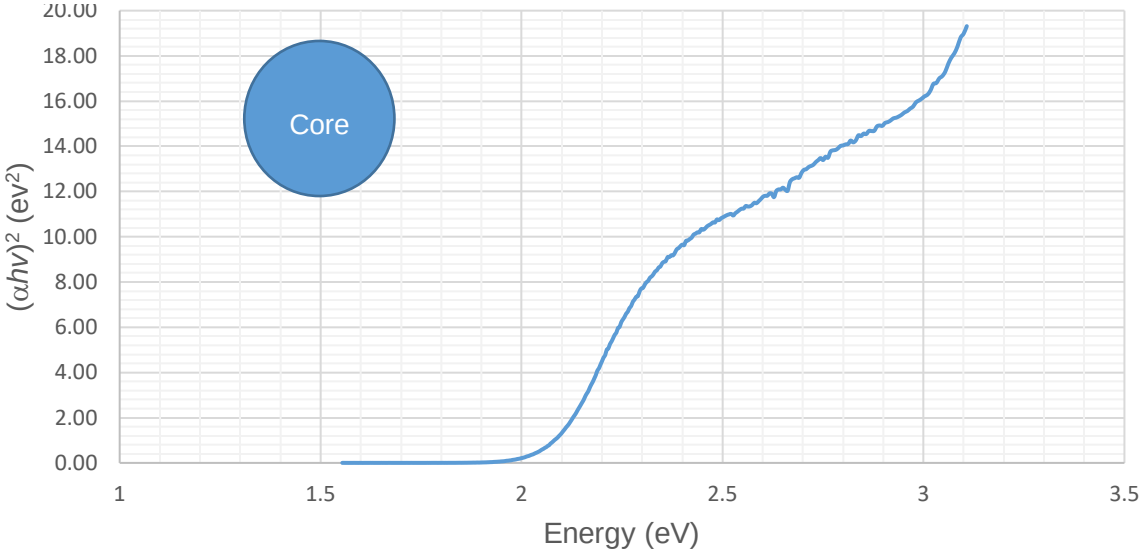

Figure 38: Tauc plot of core only $CuInS_2$ QDs. Linear line x-axis intercept indicates the band gap.

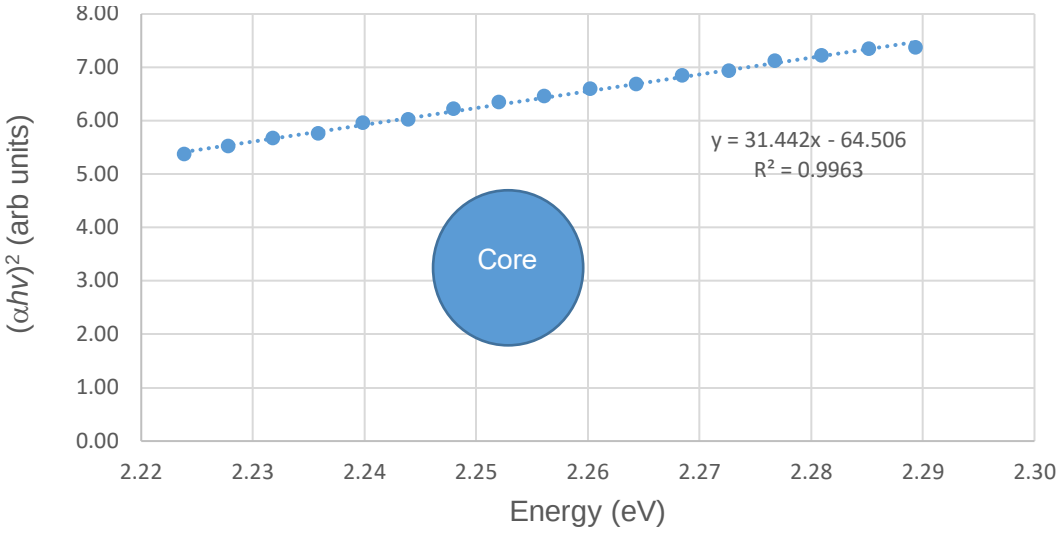

Figure 39: Linear line from Tauc plot for core only $CuInS_2$ QDs with equation of line of best fit to indicate x intercept.

For the core only sample, we estimated a band gap of ~ 2.05 eV. This would indicate QDs of radius 7.1 nm ± 0.3 nm from Equation (11). The R_2 value was 0.9963.

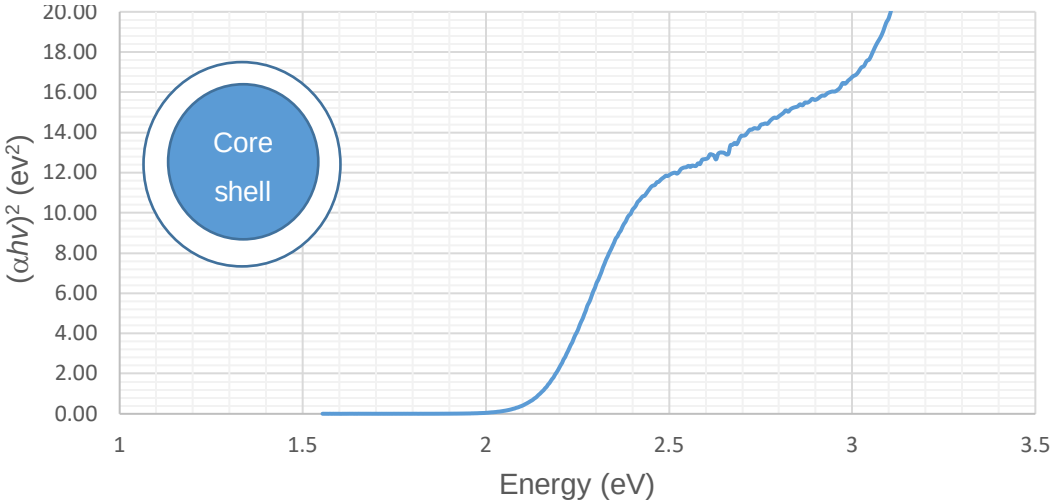

Figure 40: Tauc plot of core shell $CuInS_2/ZnS$ QDs. Linear line x-axis intercept indicates the band gap.

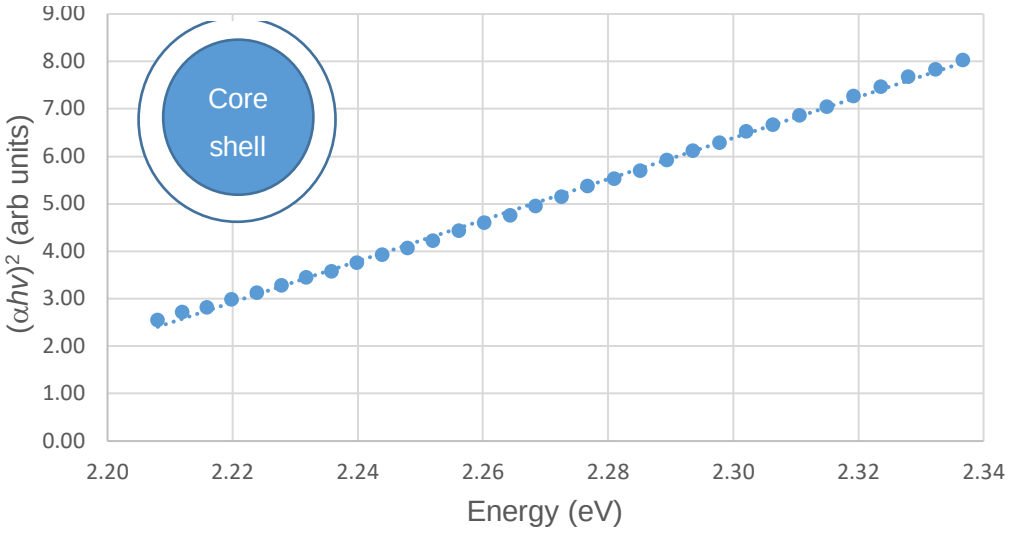

Figure 41: Linear line from Tauc plot for core shell $CuInS_2/ZnS$ QDs with equation of line of best fit to indicate x intercept.

The Tauc plot for the core-shell sample (see Figure 40 - 41) indicated a band gap of E_g ~ 2.15 eV. This would be the equivalent to a QD radius of 6.5 nm ± 0.3 nm using Equation (11). Therefore, this would show that the band gap of the core shell is 0.10 eV greater than the core only, which corresponds to a QD radius difference of 0.59 nm. The Fermi Level within the core shell sample would therefore be closer to the conduction band in the core shell sample than the core only sample. The R_2 value was 0.9987.

The band gaps estimated using the Tauc plots were larger than those found during PL spectroscopy and thus the sizes of the QDs were also estimated to be smaller. This was likely due to the fact that the emission was more likely a result of exciton recombination to intragap defect states, thus emitting a photon with energy less than the band gap. Absorption is more likely to involve band to band transition and thus analysis of the absorption spectra gives a closer reflection of the actual band gap.

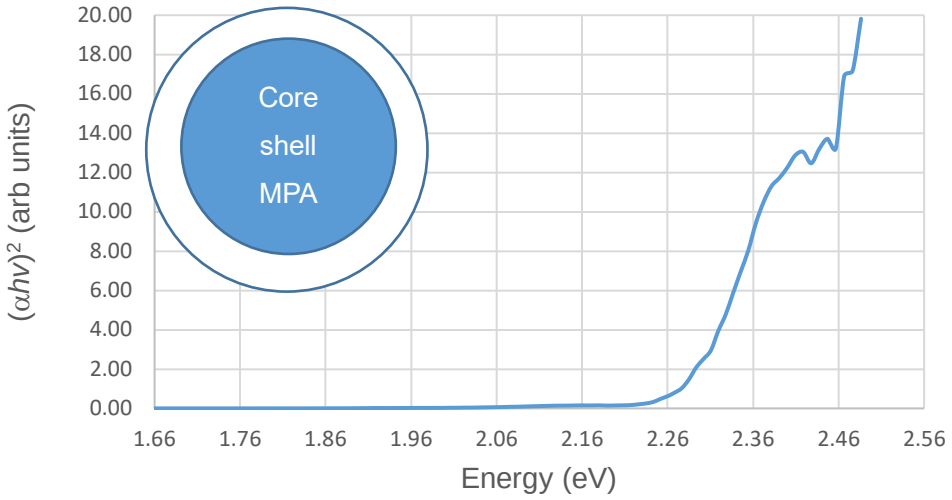

Figure 42: Tauc plot of core shell $CuInS_2/ZnS$ QDs post ligand exchange with mercaptopropionic acid. Linear line x-axis intercept indicates the band gap

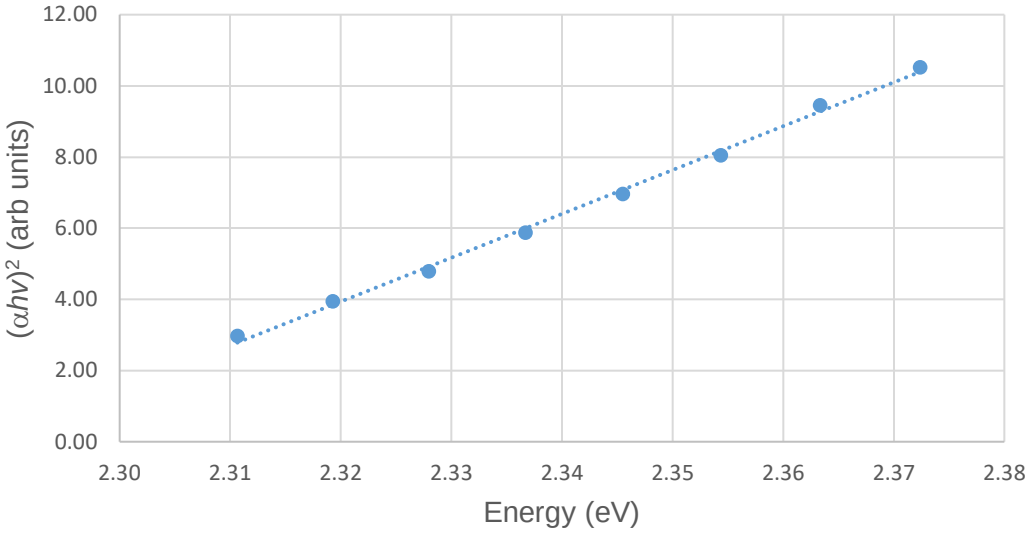

Figure 43: Tauc plot of MPA-capped $CuInS_2/ZnS$ QDs showing linear line obtained from Tauc plot with the equation of the fitted line used to determine the band gap value from the x-axis intercept.

The Tauc plot for the MPA-capped QDs suggested a band gap of approximately 2.29 eV, which was 0.14 eV greater than the DDT-capped core-shell QDs. The R_2 value was 0.9971. The increased band gap suggested the size of the QD decreased, likely due to the zinc etching into the QD core. However, the change in the energy band gap could have indicated a change in the crystal morphology of the QDs due to the different ligand-type. MPA ligands are considerably smaller than DDT ligands and thus the packing density from MPA is greater, thus likely increasing the concentration of ligands bound to

the surface of the QD. The different ligands lead to changes in the surface energies of the nanocrystalline structure, which in turn determined the equilibrium core shape of the nanoparticles and the atomistic arrangement on their surface [81]. Interestingly, in the core-shell samples, the PL and absorption profiles were both blue-shifted from the core-only. However, for the MPA samples, the PL red-shifted whereas the absorption blue-shifted compared to the DDT shell samples.

4.3.3. Emission and Absorbance Discussion

The PL and absorption profiles were plotted onto the same graphs to compare the emission and absorbance. Figure 44 and Figure 45 show the absorption (orange lines) of lower wavelength (higher energy) photons and emission (blue lines) of higher wavelength (lower energy) photons. This suggests the promotion of electrons from the valence band into the conduction band (and possibly higher states) from the absorption and the relaxation into intragap defect states from the photoluminescence spectra. The difference between the peak of the absorption spectrum and peak of the emission spectrum is given by the Stokes shift [25]. However, this was unable to be calculated since the measured absorption spectra did not have distinct peaks.

Emission maps were also plotted in Figure 46 and Figure 47 which display the intensity of the photoluminescence spectra over the range of the excitation wavelengths. Brighter spots indicate higher PL intensity, signifying a greater number of emitted photons likely due to energetically favourable transition routes.

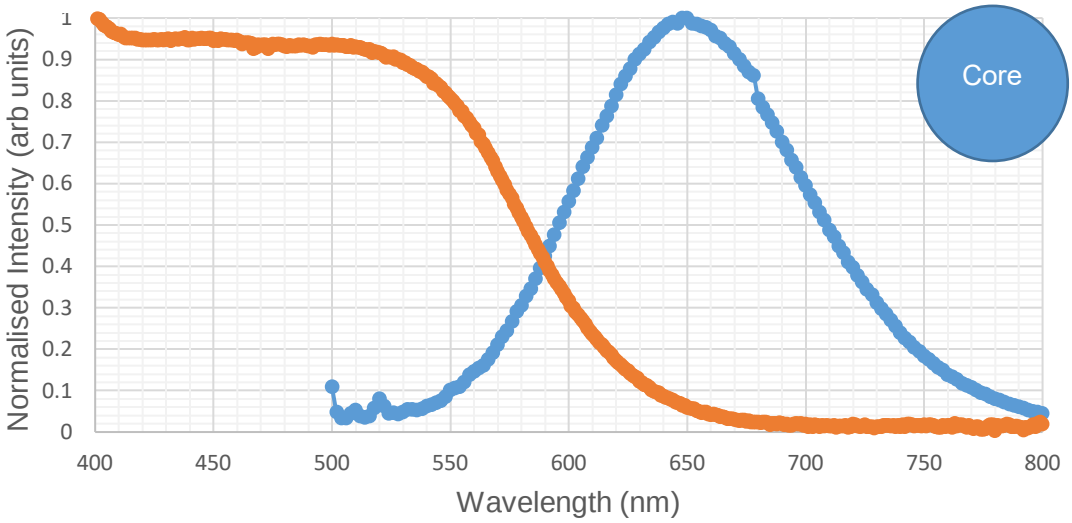

Figure 44: Plot of absorption (orange) and PL emission (blue) of core only $CuInS_2$ QDs. The QDs absorb lower wavelength photons and emit higher wavelength photons following exciton recombination.

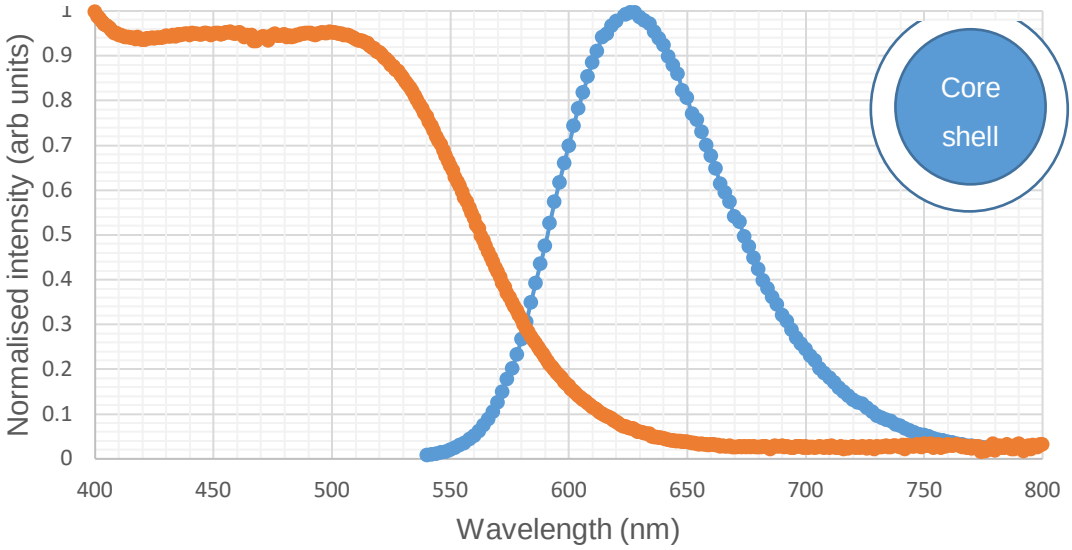

Figure 45: Plot of PL absorption (orange) and PL emission (blue) of $CuInS_2/ZnS$ QDs. The QDs absorb lower wavelength photons and emit higher wavelength photons following exciton recombination.

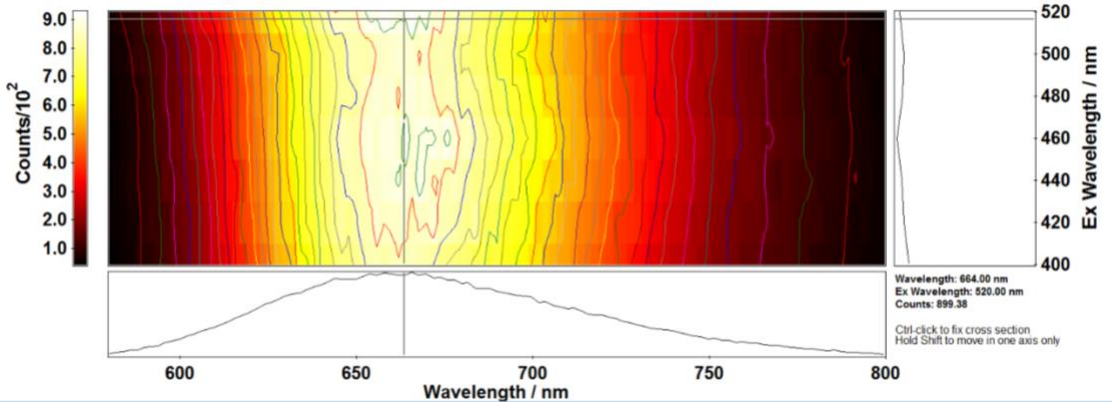

Figure 46: Emission map for core $CuInS_2$ QDs showing the intensity in counts (colour coded) of photoluminescence emission (x-axis) and excitation wavelength (y-axis).

The emission map for the core-only QDs shows that at the peak wavelength of the PL emission (664 nm), the excitation wavelength is approximately 520 nm and the emission intensity is at its brightest. There is a clear gradient emission pattern shown from Figure 46, whereby there is a large region of high emission intensity with decreased emission intensity either side, irrespective of the excitation wavelength (i.e. the excitation wavelength does not appear to affect the emission intensity). The map shows very high emission (respective to the intensity scale in Figure 46) between wavelengths of approximately 630 to 700 nm, with moderate emission towards the blue end of the spectrum between 610 and 630 nm and moderate emission towards the red end of the

spectrum between 700 nm and 745 nm.

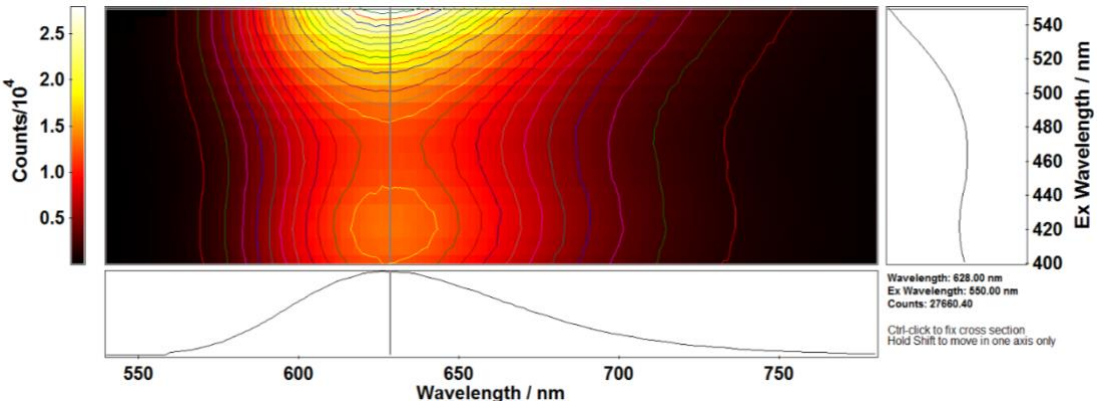

Figure 47: Emission map for core shell $CuInS_2/ZnS$ QDs showing the intensity in counts (colour coded) of photoluminescence emission (x-axis) and excitation wavelength (y-axis).

The emission map for the core shell QDs shows that for the peak PL wavelength (628 nm), the corresponding excitation wavelength is 550 nm, where the emission intensity is also at its brightest. Figure 47 does not display as distinct a gradient as the core only samples, with the emission intensity far more dependent on the excitation wavelength. The emission map shows high emission between approximately 600 and 675 nm, but only with excitations between 540 and 510 nm. Between approximately 600 nm and 700 nm (and excluding previously stated emission), moderate emission intensity is shown (respective to the intensity scale in Figure 47). There also appears to be a slightly higher region of emission intensity (but not so as intense as between an excitation wavelength of 540 and 510 nm) between 620 nm and 645 nm at excitation wavelengths between 440 and 400 nm.

For the core shell samples, the excitation wavelength dependence on the emission intensity could indicate the fewer number of transition routes available after passivating the surface with zinc sulphide, since the counts were much higher and more concentrated in a smaller range of excitation wavelengths (510 – 550 nm) at photoluminescence emission energies ranging from 600 – 660 nm (see bright yellow spot on Figure 47). In the core only samples, there are more intragap defect states which are involved in exciton recombination and hence the emission intensity is greater, since there are more possible energy transitions. However, the scale of the emission intensity for the core-shell is two orders of magnitude greater than the core-only sample, which shows that the emission intensity of the core-shell samples is greater than the core-only samples. This indicated that more photons were emitted by the core-shell sample.

4.4. Morphological Properties

4.4.1. Dynamic Light Scattering

Dynamic light scattering was used to measure the size and size distribution of the quantum dots. DLS measures the hydrodynamic radius, giving an overestimation of the physical size of the QDs. Figure 48 and Figure 49 show the DLS profile of the core-only QDs and the core-shell QDs, respectively.

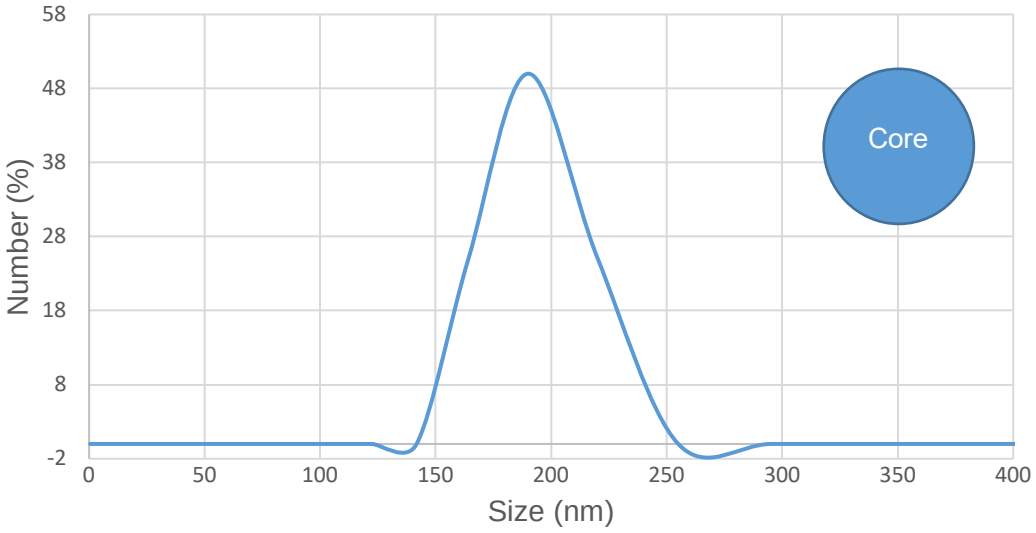

Figure 48: Size distribution of core only $CuInS_2$ QDs in hexane solvent, 0.1 mL: 1.0 mL measured using dynamic light scattering.

The size of the quantum dots were expected to be between 2 – 10 nm and using the bandgap estimations from the PL measurements, should be between 2.5 - 2.8 nm and ~ 7 nm from the Tauc plots. However, DLS of the core sample showed that QD size was 180 ± 15 nm. This indicated that the quantum dots had aggregated in solution, likely as a result of noncovalent interaction. This colloidal instability of the core QDs needs to be investigated further.

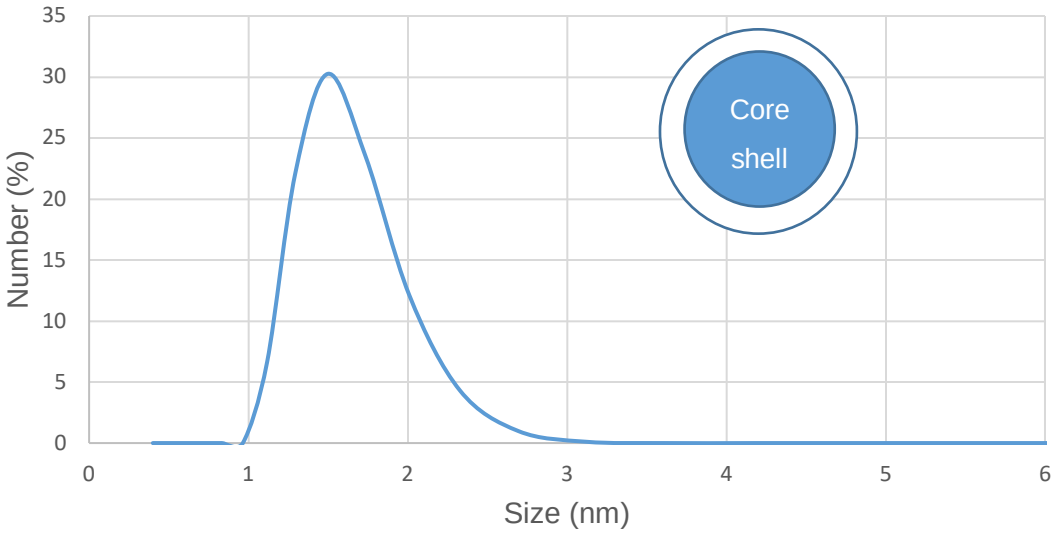

Figure 49: Size distribution of core shell $CuInS_2/ZnS$ QDs in hexane solvent, 0.001 mL: 1.00 mL measured using dynamic light scattering

The DLS measurement of the core shell sample revealed the presence of very small particles with a hydrodynamic size of 1.5 ± 0.4 nm. This result was not supported by our optical studies and is possibly due to fluorescence issues: for DLS we used 633 nm laser and optical absorption of the QDs could have interfered with the analysis. Hence, DLS equipped with a longer wavelength laser would be beneficial for the study of these QDs.

4.4.2. Nuclear Magnetic Resonance

To confirm the successful replacement of DDT ligands for MPA, we performed ^{13}C-NMR spectroscopy. We note that ^{1}H NMR was unable to distinguish the two ligands. The sample consisted of $CuInS_2$ QDs with a ZnS shell and MPA ligands attached to their surface. The QDs were dispersed in deionised water and deuterium, D_2O, was added and its signal used as a reference. Prior to the ligand exchange, the sample was purified by centrifugation and washed to remove solvent residues and unreacted precursors.

Figure 50 shows the full ^{13}C-NMR spectrum for the colloidal QDs. The three major peaks are characteristic for the solvent. Small peaks between 2.4 and 2.6 ppm confirm the presence of MPA and are assigned to the functional group of carboxylic acid. The remaining peaks are assigned to D_2O, methanol and acetone [82].

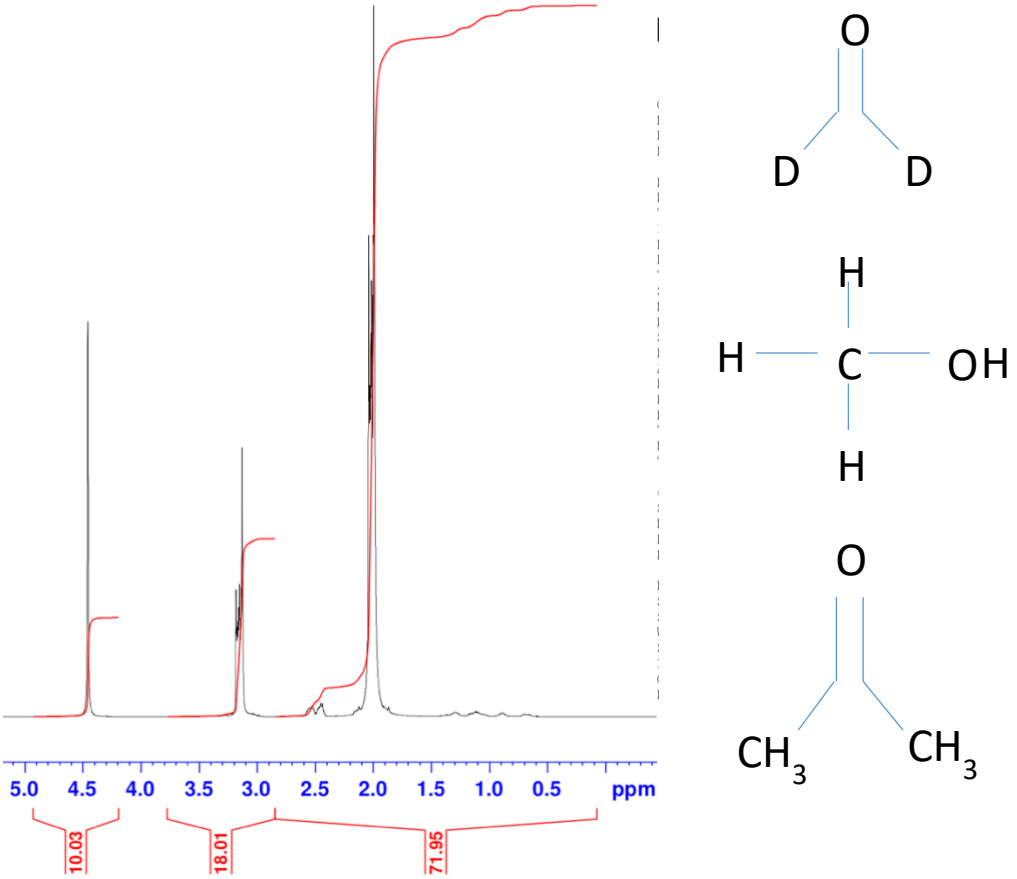

Figure 50: Carbon-13 nuclear magnetic resonance of mercaptopropionic acid exchanged $CuInS_2/ZnS$ QDs. The x-axis shows parts per million (ppm) and the y-axis is the relative intensity of the signal (i.e. the larger the peak, the more abundant the element). The peak at approx. 4.5 ppm is likely due to D_2O (top right), 3.1 ppm is likely methanol (middle right) and at 2.0 ppm due to acetone (bottom right).

Carbon-13 NMR of the MPA-exchanged $CuInS_2/ZnS$ QD confirmed successful ligand exchange.

4.4.3. Scanning Electron Microscopy

In order to examine the morphology of the QD films, SEM was used. Individual QDs would be indistinguishable as their scale was too small for the equipment used. Figure 51 shows the SEM image of the core-only samples and Figure 52 shows the SEM image of the core-shell samples.

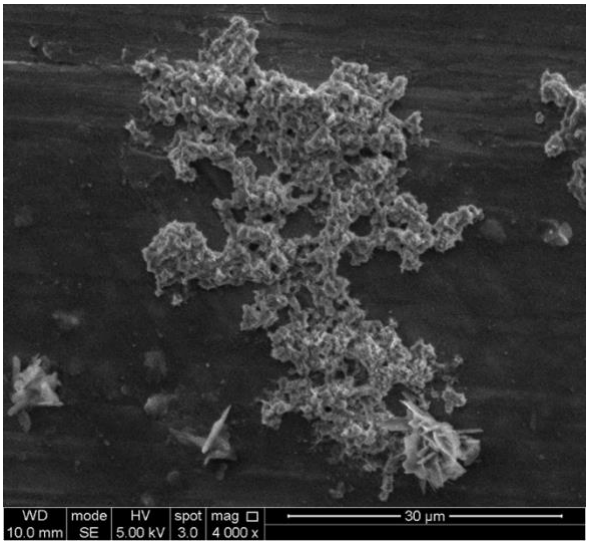

Figure 51: A representative SEM image of core only $CuInS_2$ QD film deposited on an aluminium substrate by drop-casting

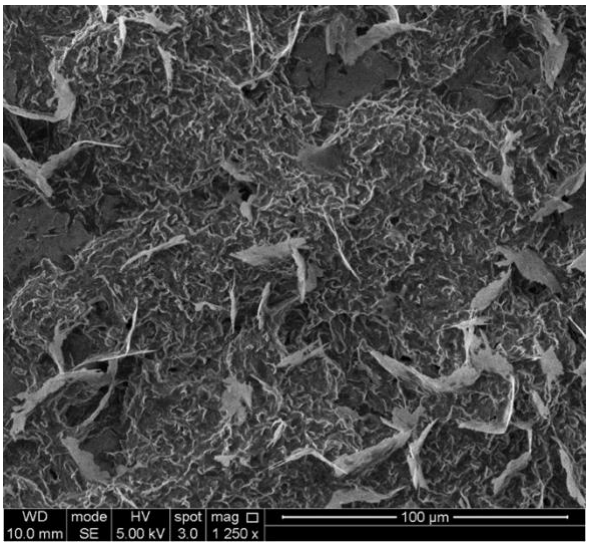

Figure 52: A representative SEM image of core shell $CuInS_2$/ZnS QD film deposited on an aluminium substrate by drop-casting

The SEM image of the core only film reveals little uniformity and formation of large clusters. The SEM image of the core-shell films revealed formation of the more uniform film with large, scattered fragments of zinc sulphide [83] which indicated an excessive amount was added during synthesis or further purification was needed. In order to observe individual QDs and thus estimate their size and shape, more refined instruments such as transmission electron microscopy would need to be used.

4.4.4. Energy Dispersive X-ray Spectroscopy

Energy Dispersive X-ray spectroscopy was used to compare the compositions of the quantum dots before and after passivation with a zinc sulphide shell. The QDs were synthesised with a copper to indium molar ratio of 1:1 and with sulphur in excess. By comparing the EDX spectra of the core-only and core-shell samples, the ratio of Cu:In may alter. This would suggest that zinc is replacing either Cu or In within the core, thus reducing the core diameter. Figure 53 shows the EDX spectrum of the core-only QDs and Figure 54 shows the EDX spectrum of core-shell QDs.

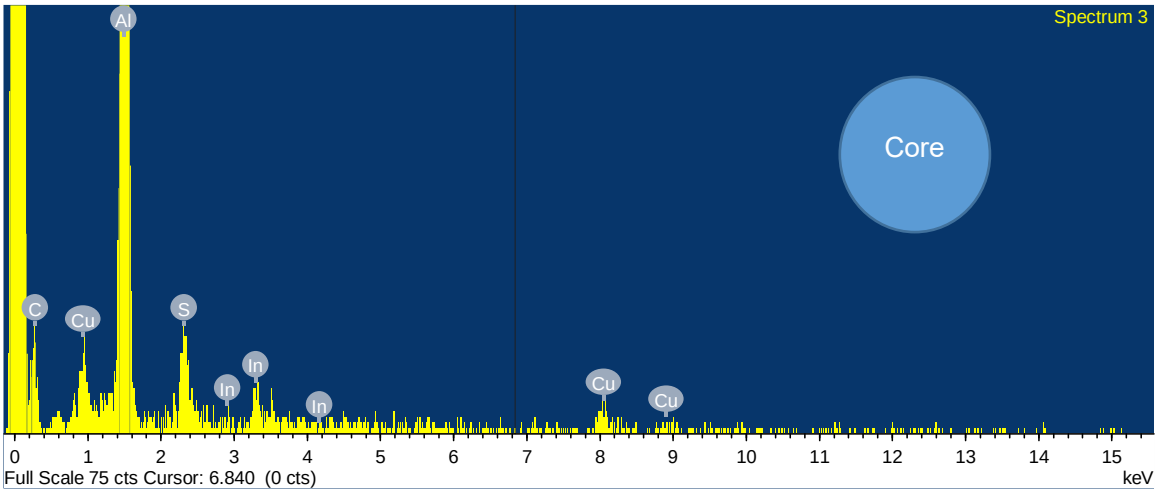

Figure 53: EDX of core $CuInS_2$ QDs

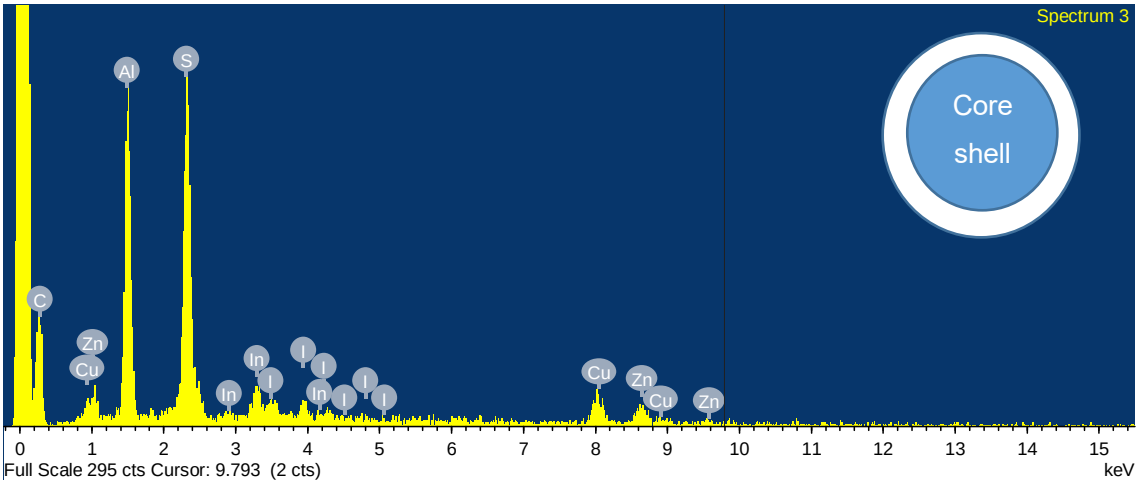

Figure 54: EDX of core shell $CuInS_2/ZnS$ QDs

Clear Zn peaks were observed for core-shell QDs. Also a large increase in the sulphur is observed for core-shell QDs compared to core-only, confirming the formation of the

ZnS shell. The spectrum In Figure 53, indicated the presence of a larger amount of copper compared to indium, thus suggesting an indium-deficient QD core. In Figure 54, the amount of indium seems relatively unchanged however, the amount of copper appeared to decrease, possibly suggesting the substitution of zinc ions for copper ions in the core and hence decreasing the size of the QD and increasing the confinement.

The detailed compositional analysis was not possible with these measurements, thus the stoichiometry of the Cu and In could not be quantitively compared before and after shell growth. Further studies are needed to correlate composition of QDs with the observed optical properties.

4.4.5. X-ray Diffraction

XRD was used to probe the crystalline structure of the nanocrystals and reveal which structure they most closely resembled. Bulk $CuInS_2$ has the chalcopyrite structure, but $CuInS_2$ QDs have also shown zinc blende and wurtzite structures (which all share characteristic peaks in XRD at approximately 27°, 46° and 55° [84]). In chalcopyrite structures, each S atom is surrounded by 2 Cu atoms and 2 In atoms, but the differing bond lengths between S-Cu and S-In result in anion displacement. In zinc blende structures, which are comparable to chalcopyrite structures, cations (Cu and In) are interchangeable, leading to cation displacement, in turn allowing for greater compositional differences compared to the chalcopyrite structures. Wurtzite structures are the hexagonal analogue of zinc blende structures where the structure is characterised as cation ordered [85]. XRD patterns for the core-only sample and core-shell samples are shown in Figure 55 and Figure 56, respectively.

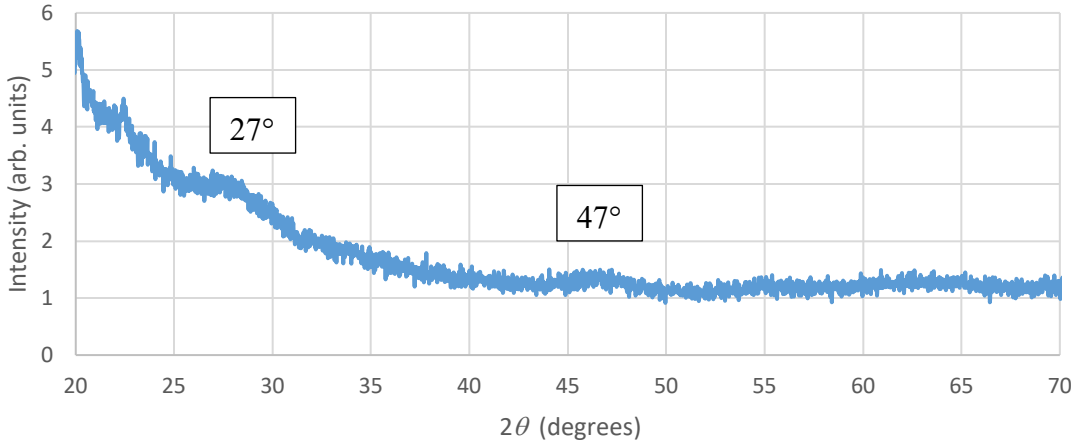

Figure 55: X-ray diffraction of CuInS2 QDs.

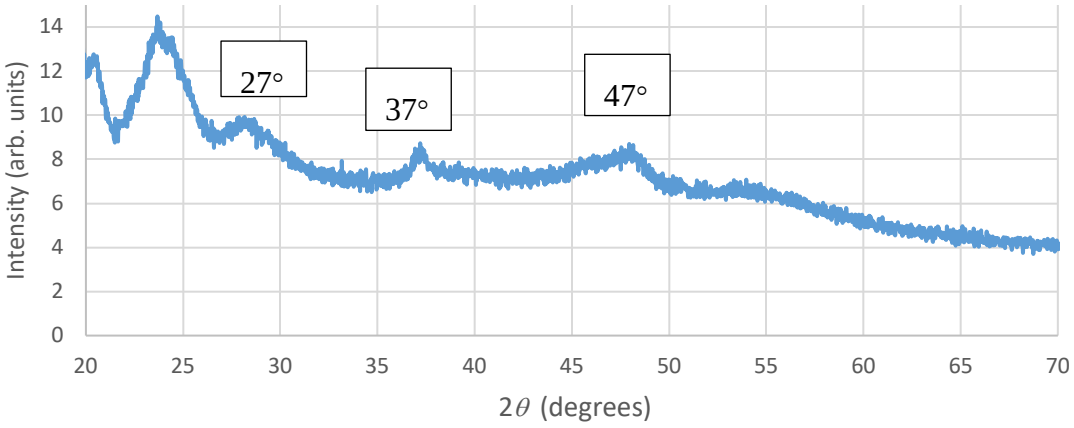

Figure 56: X-ray Diffraction of CuInS2/ZnS QDs.

Figure 55 shows the XRD pattern for the core-only $CuInS_2$ QDs and Figure 56 shows the XRD pattern for the core-shell $CuInS_2$/ZnS QDs. The XRD pattern for the core only sample was noisy, with undistinctive peaks. However, there appeared to be a peak at approximately 27° and a peak at 47°, indicating that the structure was either chalcopyrite, zinc blende or wurtzite, but there were no further peaks to distinguish between them. However, the peaks in the core-shell sample were more discernible, with peaks at 27°, 48° and a further peak at 37° (compared to the core only sample), which suggested the structure was closer to the zinc blende or wurtzite crystal formations. This was in agreement with other results which suggested the zinc was etching into the core structure and possibly replacing Cu or In cations, since in zinc blende and wurtzite structures the cation positions are interchangeable (which includes Zn). The peak below 25° in Figure 56 is likely due to organics including surface ligands and organic by-products that were not removed following purification, as such this was likely the explanation for the large signal up until 30° in Figure 55 [78].

4.5. Stability Analysis using Time-Resolved Photoluminescence Spectroscopy

4.5.1. Stability of Quantum Dots under Ultraviolet Light Conditions

For use in solar cells, quantum dots must be able to display good stability under high and low wavelength electromagnetic radiation, particularly ultraviolet light. Therefore, time-resolved photoluminescence measurements were conducted in order to test the PL response of the QDs for 300 s. The excitation source was set at a constant wavelength of 300 nm and the PL intensity was measured over the set time. A decrease over time

would indicate the QDs were degrading under the UV light, whereas a straight line would indicate the UV had no degrading effects on the QDs. Figure 57 - 59 show the time-resolved photoluminescence spectra of the DDT-capped: colloidal core-only, colloidal core-shell and deposited core-shell QDs, respectively

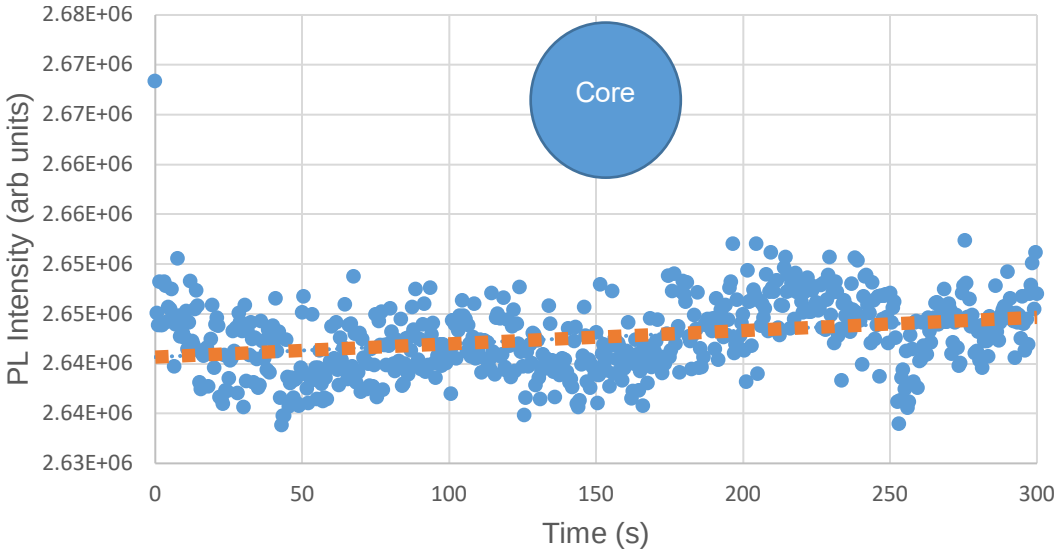

Figure 57: Time-resolved photoluminescence measurements for colloidal core only $CuInS_2$ QDs in hexane solvent. Excitation wavelength = 300 nm, provided by FLS 980 spectrometer. The orange points represent a line of best fit.

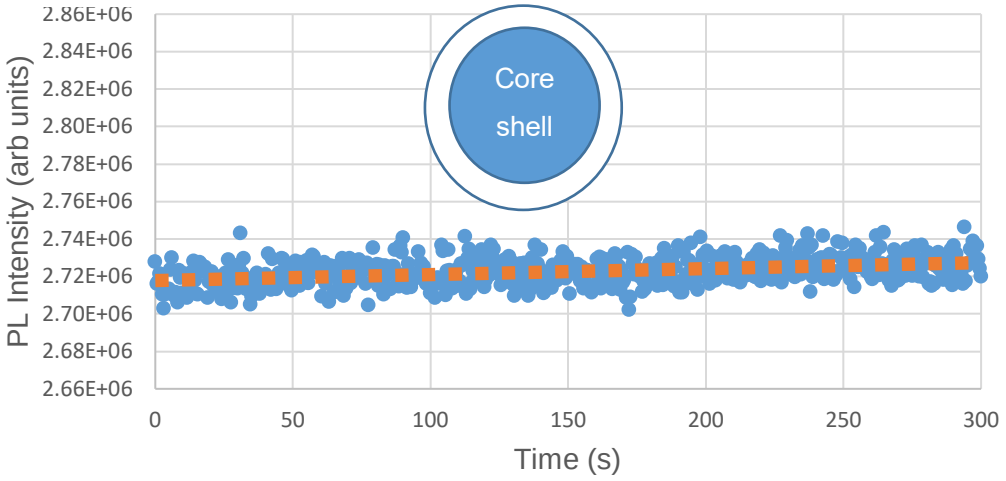

Figure 58: Time-resolved photoluminescence measurements for colloidal core shell $CuInS_2/ZnS$ QDs in hexane solvent. Excitation wavelength = 300 nm, provided by FLS 980 spectrometer. The orange points represent a line of best fit.

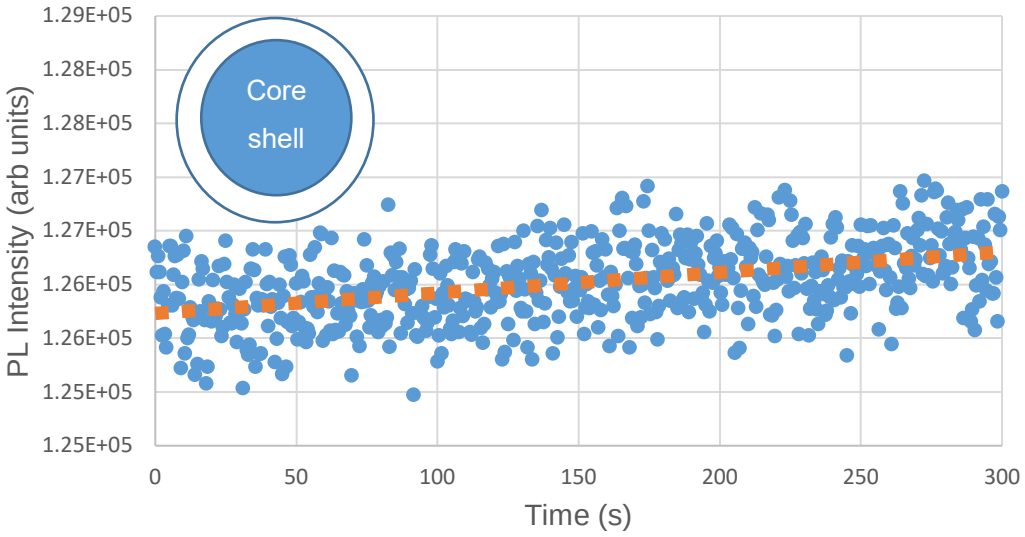

Figure 59: Time-resolved photoluminescence measurements for deposited core shell $CuInS_2/ZnS$ QDs. Excitation wavelength = 300 nm, provided by FLS 980 spectrometer. The orange points represent a line of best fit.

The time-resolved PL measurements show that the quantum dots showed a good degree of stability under λ_{Ex}= 300 nm ultraviolet light. Across the 300 s measurement, there was little indication among the samples of any decay, especially with the colloidal and deposited core shell samples. Lines of best fit were added to the stability figures which all showed slight positive correlation, thus indicating that with additional time the PL intensity under λ_{Ex}= 300 nm slightly increased. The slightly lower intensity at *T* = 0 s could be attributed to an initial absorption period where not all exciton recombination pathways were occurring, since the lifetime of CIS QDs is known to be relatively long. As such at *T* = 0 s, following absorption of the photons, some electrons may remain in higher energy states but with increased time have a larger probability of recombining with a hole in a radiative transition. However, since the exciton lifetime in $CuInS_2$ QDs is reportedly hundreds of nanoseconds [52] it was unlikely that the PL measurement was initially lower due to the long exciton lifetime, as the measurement was incremented by 0.5 s and thus significantly longer than the QD exciton lifetime. Therefore, the increase in PL intensity was more likely caused by an increase in thermal energy of the quantum dots over time (due to prolonged exposure to the excitation energy), increasing the probability of stimulating electronic transitions following the absorption of a photon.

Overall, these measurements demonstrated the promise of CIS QDs for use in photovoltaics, since there was little to suggest degradation under high energy photons. Needless to say, longer time-resolved measurements would be essential in assessing

long-term stability under UV conditions.

4.5.2. Lifetime Decay of Quantum Dots

Figure 60 shows three decay curves for the core-only samples and Figure 61 shows three decay curves for the core-shell samples. The time constants and correlation coefficients of the exponential decay fitted lines were collected in Table 1.

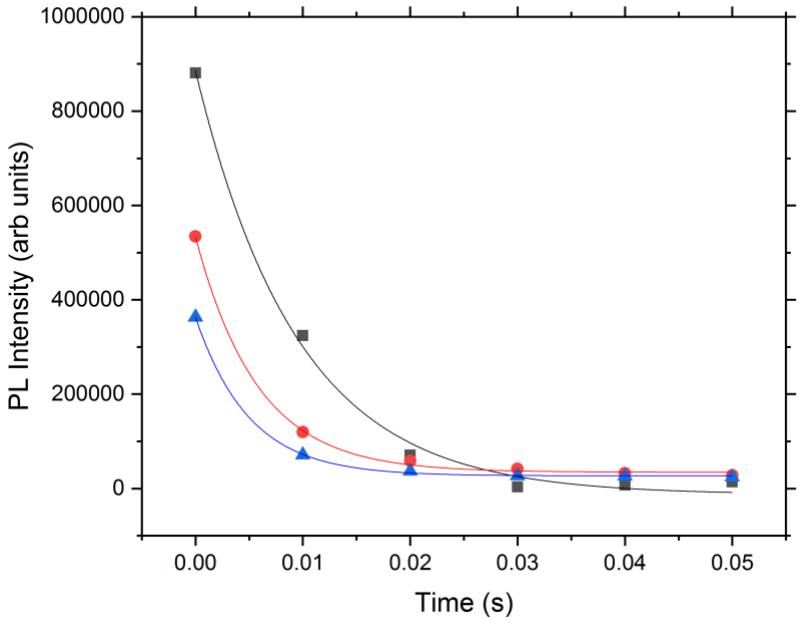

Figure 60: Repeated measurements of PL decay curves for core only DDT-capped QDs. The coloured plot points and lines of best fit show three separate measurements.

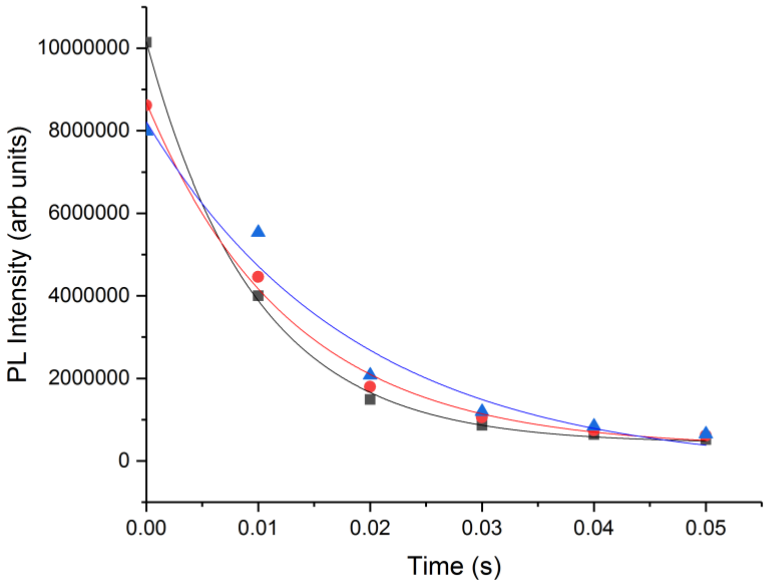

Figure 61: Repeated measurements of PL decay curves for core-shell DDT-capped QDs. The coloured plot points and lines of best fit show three separate measurements.

As shown by Figure 61 and Figure 62, the rate of decay in the core-only samples was faster than the core-shell. From Table 1, it was shown that the rate of decay in core-only QDs was an order of magnitude 10x quicker than the core-shell QDs. It was expected that a greater number of available exciton recombination transitions would be available, namely in the form of surface defects, in the core-only samples which would lead to a quicker decay. This would have shown that passivation of the QD core with a ZnS shell removed many defect states and thus the lifetime of the exciton was greater (slower decay). These results also explained the difference in the PL emission intensity between core-only and core-shell samples. The work from Chi et al. [86] postulated that long decay times can be described as 'population times'; instances where excited electrons need to escape from trap states and move to emission sites. Consequently, the trapping of electrons at defects not only lengthens the population processes of the emissive sites but also partly reduces the emission intensity. This would be supported by earlier PL measurements (Section 4.3.1) where the intensity of the core shell samples is much greater than in the core only samples.

$CuInS_2$-type	Time Constants and R_2 Values					
	τ_1 (s)	R_2 for τ_1	τ_2 (s)	R_2 for τ_2	τ_3 (s)	R_2 for τ_3
Core	0.00950	0.9963	0.00577	0.9993	0.00501	0.9998
Core-Shell	0.09680	0.9996	0.01291	0.9960	0.01864	0.9929

Table 1: Time constants, τ, and values for correlation coefficients, R_2, for the core and core-shell decay plots

Chapter 5. Conclusions and Future Work

The purpose of this work was to synthesise and characterise the optical and morphological properties of $CuInS_2$ QDs as they represent a promising candidate for the next generation of photovoltaics. They can be synthesised without using heavy metal precursors (which are toxic to humans) with a facile solvothermal method of synthesis which is able to be scaled-up; displaying their commercial viability. With the aforementioned method, colloidal QDs can be produced with a degree of control over their final size which directly determines their optical properties due to quantum confinement.

The core of the QD can be passivated with a zinc sulphide shell which aids the photostability of the QDs as well as removing surface defects which act as trap states; non-radiative recombination pathways. However, this is likely done at the expense of decreasing the core of the QD, as zinc ions are expected to replace either copper or indium ions within the core, thus shrinking the size of the core. This was suggested by the blue-shift of the PL and absorption spectra after passivation with a ZnS shell. However, to corroborate this, compositional EDX measurements would have been needed; whereby the compositional amount of copper to indium could have been viewed before and after addition of zinc sulphide. A change in the Cu:In ratio would have suggested that Zn was replacing either the Cu or In, thus this would be recommended for future work. Furthermore, photostability measurements of the QDs after shell formation showed no indication of greater photostability, as the time-resolved PL measurements indicated the core-only and core-shell (colloidal and deposited) both remained stable under UV light. However, in future work the photostability measurements should be repeated for much longer time-periods to identify at which point photodegradation begins to occur (e.g. 30 days). The decay measurements of the QDs after shelling also showed a longer exciton lifetime approximately 10x longer than without the shell. This suggested that there were fewer recombination routes within the QD which would have allowed for a faster exciton recombination.

Long chain ligands were attached to the QDs following their synthesis in order to achieve the desired composition of the QDs, but they can be substituted for alternative ligands for different purposes. For example, a ligand with different functional groups could substitute the original ligands (DDT for this work) so that the QDs were dispersible in water. Alternatively, smaller ligands could be substituted in order to increase the QD packing density, since smaller ligands would permit for the QDs to be positioned closer

together. In this work, mercaptopropionic acid ligands were substituted which theoretically allowed for QD dispersion in water, as well as increasing QD loading (increased density of QDs after deposition onto a substrate). However, the PL showed a red-shift from the DDT-capped shell QDs, whereas the absorption profile was blue-shifted from the DDT-capped shell QDs. It was postulated that MPA passivated the QD with surface defects which lead to a red-shifted PL, but the increased QD-loading lead to an alternative crystalline arrangement which lead to a blue-shift in the absorption, since the spacing between QDs was decreased and thus it was less likely for photons to pass through the structure. Alternatively, it was postulated that zinc etched into the QD core during the ligand exchange, thus decreasing the size of the core and increasing the quantum confinement of the QD. In future work, the photostability and exciton lifetime of the MPA-capped QDs should also be measured and compared to the DDT-capped shell results. To corroborate with the expected reason behind the red-shift in the PL measurement, the PL decay would indicate that MPA passivation induced defect states if the lifetime was shorter than in the DDT-capped shell.

Other future work would include performing transmission electron microscopy (TEM) to observe individual QDs and thus estimate their morphology. The size of the QDs from TEM could then be used to estimate the band gap using Equation 10 and compared to the estimates gathered from PL and absorption measurements. Additionally, charge-transport measurements of QD solids fabricated from CIS QDs could be conducted before and after ligand exchange with the shorter, MPA ligands to reveal the magnitude of the effect on transport of increased QD loading. Since the QDs would be much closer together, it would be expected that the charge transport would be much quicker with MPA ligands compared to DDT-ligands. The charge transport could also be measured under different temperatures to establish the transport mechanism; a high dependence on temperature would indicate hopping, but small or zero dependence would indicate quantum tunnelling [87].

References

[1] "Green Growth Studies: Energy." Organisation for Economic Co-operation and Development and International Energy Agency. (accessed 14th July, 2019).

[2] J. Hammarstrom, "Overview: Capturing the Sun for Energy Production," *AMBIO,* vol. 41, no. 2, pp. 103 - 107, 2012.

[3] M. Gratzel, "Photochemical Cells," *Nature,* vol. 414, pp. 338 - 344, 2001.

[4] D. Hanson and E. Harvey, "Quantum States of Atoms and Molecules," *J. Chem. Educ.,* vol. 82, no. 12, 2005.

[5] S. Kei, "Band diagram - semiconductors," vol. 441 x 303, B. o. semiconductors, Ed., ed. Wikipedia Commons, 2006, p. https://commons.wikimedia.org/w/index.php?curid=728753.

[6] R. Largent and S. Wenham, R. Largent, Ed. *Solar cells: resources for the secondary science teacher*. Key centre for photovoltaic engineering, Univ. New South Wales, 2003, p. 70.

[7] T. R. Kuphaldt, "Solid State Device Theory," *vol. 3*.

[8] L. C. Andreani and A. Bozzola, "Silicon solar cells: toward the efficiency limits," *Adv. in Phys. X,* vol. 4, no. 1, 2018.

[9] S. S. Verma, "Next Generation Solar Cells: The Future of Renewable Energy," pp. 22-25, 2016.

[10] J. Rangel-Cárdenas and H. Sorbal, "Optical absorption enhancement in CdTe thin films by microstructuration of the silicon substrate," *Materials,* vol. 10, no. 607, 2017.

[11] T. D. Lee and A. U. Ebong, "A review of thin film solar cell technologies and challenges," pp. 1286-1297, 2017.

[12] A. Extance, "The reality behind solar power's next star material," vol. 570*,* pp. 429 - 432, 25th June,

[13] R. Peleg. "Perovskite Solar." (accessed 20th June, 2019).

[14] K. Sharma and V. Sharma, "Dye-sensitised solar cells: fundamentals and current status," *Nano. Res. Letters,* vol. 13, no. 381, 2018.

[15] K. Kakiage and Y. Aoyama, "Highly-efficient dye-sensitised solar cells with collaborative sensitisation by silly-anchor and carboxylate-anchor dyes," *Chem. Commun.,* vol. 51, pp. 15894 - 15897, 2015.

[16] H. P. Myers, *Introductory solid state physics*, 2 ed. CRC Press, 1990, p. 520.

[17] R. Nave. "Fermi Level." HyperPhysics. (accessed 10th July, 2019).

[18] "Fermi energy and fermi surface." Engineering LibreTexts. (accessed 15th July, 2019).

[19] S. Some and I. K. Sen, "Biosynthesis of silver nanoparticles and their versatile antimicrobial properties," *Mater. Res. Exp.,* vol. 6, no. 1, 2018.

[20] A. Valizadeh and H. Mikaeili, "Quantum dots: synthesis, bio applications and toxicity," *Nano. Res. Letters,* vol. 12, no. 7, 2012.

[21] J. van Embden and A. S. R. Chesman, "The heat-up synthesis of colloidal nanocrystals," *Chem. Meter.,* vol. 27, pp. 2246 - 2285, 2015.

[22] M. Booth, "Synthesis and characterisation of CuInS2 quantum dots," Doctorate, Sch. of Physics and Astronomy, University of Leeds, 2014.

[23] X. Michalet and F. F. Pinaud, "Quantum dots for live cells, in-vivo imaging and diagnostics," *ScienceMag,* vol. 307, pp. 538 - 544, 2005.

[24] Z. Ahmad and M. A. Najeeb, "Limits and possible solutions in quantum dot organic solar cells," *Ren. Sust. Energy.. Rev.,* vol. 82, pp. 1551 - 1564, 2018.

[25] A. R. AbouElhamd, "Review of core/shell quantum dots technology integrated into building's glazing," *Energies,* vol. 12, p. 1058, 2019.
[26] A. Sedlmeier and H. H. Gorris, "Surface modification and characterisation of photon-upconverting nanoparticles for bioanalytical applications," *Chem. Soc. Rev.,* vol. 44, no. 6, pp. 1526 - 1560, 2015.
[27] F. Xu and L. F. Gerlein, "Impact of different surface ligands on the optical properties of PbS quantum dot solids," *Mater.,* vol. 8, no. 4, pp. 1858 - 1870, 2015.
[28] H. J. Yun and J. Lim, "Charge-transport mechanisms in CuInS2xS2-x quantum dot films," *ACS Nano,* vol. 12, pp. 12587 - 12596, 2018.
[29] A. Smith and S. Nie, "Semiconductor nanocrystals: structure, properties and band gap engineering," *Acc. Chem. Res.,* vol. 43, no. 2, pp. 190 - 200, 2010.
[30] L. Sinatra and J. Pan, "Methods of synthesising mono disperse colloidal quantum dots," *Mater. Mat.,* vol. 12, no. 1, 2017.
[31] H. Goodwin and T. C. Jellicoe, "Multiple exciton generation in quantum dot-based solar cells," *Nanophotonics,* vol. 7, no. 1, pp. 111 - 126, 2018.
[32] A. Kurzmann and A. Ludwig, "Auger recombination in self-assembled quantum dots: quenching and broadening of the charged exciton transition," *Nano. Lett.,* vol. 16, pp. 3367 - 3372, 2016.
[33] T. Edvinsson, "Optical quantum confinement and photocatalytic properties in two-, one- and zero-dimensional nanostructures," *R. Soc. open Sci.,* vol. 5, 2018.
[34] J. Shi and F. Tian, "Nanoparticle based fluorescence resonance energy transfer (FRET) for biosensing applications," *J. Mater. Chem. B.,* vol. 3, no. 35, pp. 6989 - 7005, 2015.
[35] S. Kane, "Spectroscopy and quantum dots," ed. Haverford College, Physics Dept., 2011, pp. 1 - 2.
[36] C. Czekelius and M. Hilgendorff, "A simple colloidal route to nanocrystalline ZnO/CuInS2 bilayers," *Adv. Mater.,* vol. 11, no. 8, pp. 643 - 646, 1999.
[37] J. Krustok and J. Raudoja, "Photoluminescence and the tetragonal distortion in CuInS2," *Thin Solid Films,* vol. 387, pp. 195 - 197, 2001.
[38] A. I. Onyia and H. I. Ikeri, "Theoretical study of the quantum confinement effects of quantum dots using particle in a box model," *J. Ovonic. Res.,* vol. 14, no. 1, pp. 49 - 55, 2018.
[39] M. Booth, "Determining the concentration of CuInS2 quantum dots from the size-dependent molar extinction coefficient," *Chem. Mater.,* vol. 24, pp. 2064 - 2070, 2012.
[40] A. C. Berends and M. J. J. Mangnus, "Optoelectronic properties of ternary I-III-VI2 semiconductor nanocrystals: bright prospects with elusive origins," *J. Phys. Chem. Lett.,* vol. 10, pp. 1600 -1616, 2019.
[41] T. Omata and K. Nose, "Size dependant optical band gap of ternary I-III-IV2 semiconductor nanocrystals," *S. J. Appl. Phys.,* vol. 105, no. 7, 2009.
[42] Y. A. Alemu, "Synthesis, surface treatment, and characterisation of copper indium disulphide quantum dots," Master of Science, Sch. Chem. Bio. Environ. Eng., Oregon State Univ., 2016.
[43] J. Kolny-Olesiak and H. Weller, "Synthesis and application of colloidal CuInS2 semiconductor nanocrystals," *ACS Appl. Mater. Interfaces,* vol. 5, pp. 12221 - 12237, 2013.
[44] C. Robinson, "Influence of shelling temperature and time on the optical and structural properties of CuInS2/ZnS quantum dots," Master of Science in Chemistry, University of Arkansas, Fayetteville, 2015.
[45] L. Li and A. Pandey, "Efficient synthesis of highly luminescent copper indium

sulphide-based core/shell nanocrystals with surprisingly long-lived emission," *J. Am. Chem. Soc.,* vol. 133, pp. 1176 - 1179, 2011.

[46] A. Bechiri and F. Benmakhlouf, "Calculation of electronic and optical properties of Zn-based II-VI semiconductors," *Phys. Procedia,* vol. 2, pp. 803 - 812, 2009.

[47] Y. Chen and S. Li, "Green and facile synthesis of water-soluble Cu-In-S/ZnS core/shell quantum dots," *Inorg. Chem.,* vol. 52, pp. 7819 - 7821, 2013.

[48] A. Frank and J. Grunwalk, "Facile and robust solvothermal synthesis of nanocrystalline CuInS2 thin films," *Nano. Mater.,* vol. 8, no. 405, 2018.

[49] L. Sinatra and J. Pan, "Methods of synthesising monodisperse colloidal quantum dots," *Mater. Matters,* vol. 12, no. 1, 2017.

[50] N. P. Brawand and M. B. Goldey, "Defect states and charge transport in quantum dot solids," *Chem. Mat.,* vol. 29, no. 3, pp. 1255 - 1262, 2017.

[51] T. Onishi and K. Abe. "Defect states in CuInS2 crystals grown by traveling heater method." (accessed 1B, 44).

[52] Fuhr and H. J. Yun, "Light emission mechanisms in CuInS2 quantum dots evaluated by spectral electrochemistry," *ACS Photonics,* vol. 4, pp. 2425 - 2435, 2017.

[53] S. Brovelli and C. Galland, "Tuning radiative recombination in Cu-doped nanocrystals via electrochemical control of surface trapping," *Nano. Lett.,* vol. 12, pp. 4372 - 4379, 2012.

[54] D. Sharma and R. Jha, "Quantum dot sensitised solar cell: recent advances and future perspectives in photoanode," *Solar: Energy Mater. Solar Cells,* vol. 155, pp. 294 - 322, 2016.

[55] M. Ye and X. Gao, "Recent advances in quantum dot-sensitised solar cells: insights into photoanodes, sensitisers, electrolytes and counter electrodes," *Sust. Ener. Fuels,* vol. 1, pp. 1217 - 1231, 2017.

[56] B. Fu and C. Deng, "Efficiency enhancement of solid-state CuInS2 quantum dot-sensitised solar cells by improving charge recombination," *Nano. Res. Lett.,* vol. 14, no. 198, 2019.

[57] J. Lee and M. Kovalenko, "Band-like transport, high electron mobility and high photoconductivity in all-inorganic nanocrystal arrays," *Nat. Nanotech.,* vol. 6, pp. 348 - 352, 2011.

[58] E. Talgorn and Y. N. Gao, "Quantum yield of photo generated charges and band-like transport in quantum-dot solids," *Nat. Nanotech.,* vol. 6, pp. 733 - 739, 2011.

[59] J. Choi and A. R. Fafarman, "Bandlike transport in strongly coupled and doped quantum dot solids: a route to high-performance thin-film electronics," *Nano. Lett.,* vol. 12, pp. 2631 - 2638, 2012.

[60] P. Guyot-Sionnest, "Electrical transport in colloidal quantum dot thin films," *J. Phys. Chem. Lett.,* vol. 3, pp. 1169 - 1175, 2012.

[61] A. J. Nozik and M. C. Beard, "Semiconductor quantum dots and quantum dot arrays and applications of multiple exciton generation to third-generation photovoltaic solar cells," *110,* pp. 6873 - 6890, 2010.

[62] S. Jiao and J. Du, "Nitrogen-doped mesoporous carbons as counter electrodes in quantum dot sensitised solar cells with a conversion efficiency exceeding 12%," *J. Phys. Chem. Lett.,* vol. 8, pp. 559 - 564, 2017.

[63] Z. Pan and H. Rao, "Quantum dot-sensitised solar cells," *Chem. Soc. Rev.,* vol. 47, pp. 7659 - 7702, 2018.

[64] J. Zhang and W. Sun, "One-pot synthesis of hydrophilic CuInS2 and CuInS2-ZnS colloidal quantum dots," *J. Mater. Chem. C,* vol. 2, no. 24, pp. 4812 - 4817, 2014.

[65] T. P. Instruments. "Fluorescence, phosphorescence, and photoluminescence

spectroscopy." (accessed.
[66] O. Optics. "Absorbance." Ocean Optics. (accessed 2019).
[67] X. Gao and L. Yang, "In vivo molecular and cellular imaging with quantum dots," *Current Opinion in Biotechnology,* vol. 16, no. 1, pp. 63 - 72, 2005.
[68] O. Gidron. "What is NMR?" Hebrew University of Jerusalem. (accessed 16th Aug., 2019).
[69] A. Nanakoudis. "What is SEM? Scanning electron microscope technology explained." ThermoFisher Scientific. (accessed 28th Aug., 2019).
[70] M. Hudl, "Magnetic materials with unable thermal, electrical, and dynamic properties - an experimental study of magnetocaloric, multiferroic, and spin-glass materials," Science and Technology, Uppsala University, Sweden, 2012.
[71] L. Li and T. J. Daou, "Highly luminescent CuInS2/ZnS core/shell nanocrystals: cadmium-free quantum dots for in-vivo imaging," *Chem. Mater.,* vol. 21, no. 12, pp. 2422 - 2429, 2009.
[72] J. Li and B. Kempken, "Alloyed CuInS2-ZnS nanorods: synthesis, structure, and optical properties," *CrystEngComm,* vol. 17, pp. 5634 - 5643, 2015.
[73] K. N. Lawrence and P. Dutta, "Dual role of electron-accepting metal-carboxylate ligands: reversible expansion of exciton delocalisation and passivation of nonradiative trap-states in molecule-like CdSe nanocrystal," *J. Am. Chem. Soc.,* vol. 138, pp. 12813 - 12825, 2016.
[74] H. D. A. and P. V. Kamat, "Quantum dot surface chemistry: ligand effects and electron transfer reactions," *J. Phys. Chem. C,* vol. 117, pp. 14418 - 14426, 2013.
[75] A. A. Yagenetfere and H. A. Gustavo, "Enhanced photoluminescence from CuInS2/ZnS quantum dots: organic superacid passivation," *Mat. Lett.,* vol. 219, pp. 178 - 181, 2018.
[76] C. Xia and W. Wu, "Size-dependant band-gap and molar absorption coefficients of colloidal CuInS2 quantum dots," *ACS Nano,* vol. 12, pp. 8350 - 8361, 2018.
[77] Z. Wang, "Fabrication and optical properties of CuInS2 quantum dots," presented at the International Conference on Electronic Packing Technology, 2017.
[78] R. Yan, "Optical spectroscopy reveals transition of CuInS2/ZnS to CuxZn1-xInS2/ZnS:Cu alloyed quantum dots with resultant double-defect luminescence," *APL Mater.,* vol. 4, 2016.
[79] A. R. Clapp and I. L. Medintz, "Fluorescence resonance energy transfer between quantum dot donors and dye-labelled protein acceptors," *J. Am. Chem. Soc.,* vol. 126, pp. 301 - 310, 2004.
[80] B. D. Viezbicke and S. D. B. E. Patel, "Evaluation of the Tauc method for optical absorption edge determination: ZnO thin films as a model system," *Physica Status Solidi,* vol. 252, no. 8, pp. 1700 - 1710, 2015.
[81] D. F. Garcia-Gutierrez and L. P. Hernandez-Casillas, "Influence of the capping ligand on the band gap and electronic levels of PbS nanoparticles through surface atomistic arrangement determination," *ACS Omega,* vol. 3, pp. 393 - 405, 2018.
[82] C. A. Merlic. "Notes on NMR Solvents." (accessed 21st Jan, 2020).
[83] K. Jayanthi and S. Chawla, "Structural, optical and photoluminescence properties of ZnS:Cu nanoparticle thin films as a function of dopant concentration and quantum confinement effect," *Crystal Res. and Tech.,* vol. 42, no. 10, pp. 976 - 982, 2007.
[84] E. Dutkova and N. Daneu, "Mechanochemical synthesis and characterisation of CuInS2/ZnS nanocrystals," *Molecules,* vol. 24, no. 1031, 2019.
[85] A. D. P. Leach, "Optoelectronic properties of CuInS2 nanocrystals and their origin," *J. Phys. Chem. Lett.,* vol. 7, pp. 572 - 583, 2016.

[86] T. T. K. Chi and N. Q. Liem, "Time-resolved photoluminescence study of CuInS2/ZnS nanocrystals," *Adv. Nat. Sci. Nano. Nanotech.,* vol. 1, no. 2, 2010.
[87] R. H. Gilmore and S. W. Winslow, "Inverse temperature dependence of charge carrier hopping in quantum dot solids," *ACS Nano,* vol. 12, pp. 7741 - 7749, 2018.